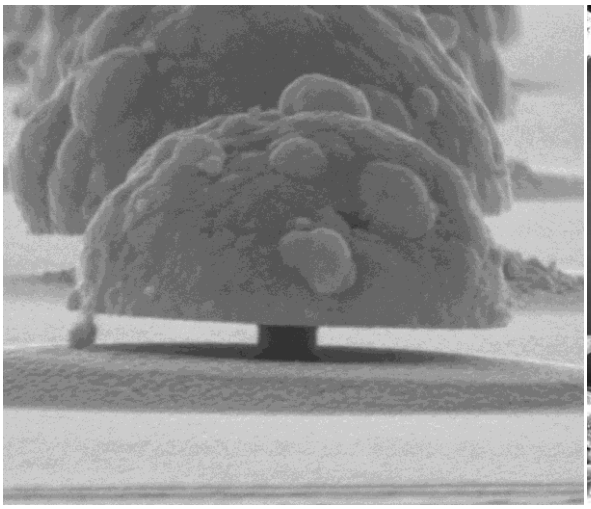
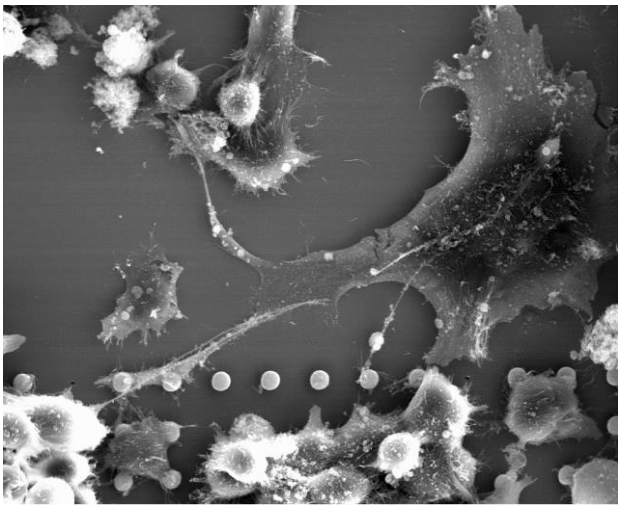

Fabrication of biocompatible gold mushrooms-shaped microelectrodes for the recording of neuronal signals

Mónica Catarina Costa Cerquido
Integrated Masters in Engineering Physics
Physics and Astronomy Department
2016

Supervisor
Dr. João Oliveira Ventura, Auxiliar Research, Faculty of Sciences of the University of Porto

Co-Supervisor
Dr. Paulo Aguiar, Auxiliar Research, Instituto de Investigação e Inovação em saúde da Universidade do Porto

U.PORTO

FACULDADE DE CIÊNCIAS
UNIVERSIDADE DO PORTO

Todas as correções determinadas pelo júri, e só essas, foram efetuadas.

O Presidente do Júri,

Porto, _____/_____/_____

Acknowledgements

As the author of this dissertation,I would like to recognize those who were most relevant in my personal and professional development and who are ultimately responsible for providing me with all the necessary tools to accomplish this dissertation.

First I would like to thank my supervisors Dr. João Ventura and Dr. Paulo Aguiar for all the help, support, advices and motivation. I have a special thank for Dr. João Ventura for made me believe in myself and my abilities, when I doubt myself. It was an enriching experience, which I will never forget. For both a thank you.

I want to mention Dr. Mariana Proença and Dr. Diana Leitão, for all the help, time spent, patience and assistance in all the process of microelectrodes fabrication. Dr. Mariana Proença and Dr. Diana Leitão play an important role throughout this project through its expertise in SEM analysis and Electrodeposition (Dr. Mariana Proença); in Lithography techniques (Dr. Diana Leitão). It was a pleasure working with you and a huge thank you for all the taught.

For all the help, counsel, support and company during the work, I thank my colleagues and friends, Catarina Dias, Joana Silva, Ana Pires, Pedro Rodriques, Bernardo Bordalo and Rui Costa.

I want to a special thank for Cátia Rodrigues and Ana Gomes for all the incredible moments, studying ,stressing, train trips and principally for the laughing. I am really thankful to have their friendship and support, and to share with them some of the best moments of my life. Thanks for all girls!

Finally, I have a huge thank you for my father, José Cerquido, because him always believe in me and support me in all the choices that I do. I wanted to thank my mother, Fernanda Cerquido, my grandmother Arminda Marcelo, my sister Márcia Cerquido and my boyfriend Braúlio Batista, for support and counsel me to be better each day. For my family thank you so much for being in my life, by my side and without them none of this would have been possible.

Resumo

A bioelectrónica é uma área de estudo que conecta a Fisica, a Biologia, a Química e a Electrónica, num objectivo comum de desenvolver sensores capazes de interagir com a matéria biológica (células, músculos, etc), de forma a conseguirem traduzir processos biológicos em respostas eléctricas, capazes de serem medidas e interpretadas. A Neuroelectrónica é uma área que estuda as células nervosas através de dispositivos criados com micro/nanotecnologia, tendo como objectivos compreender a interação e a forma do impulso nervoso das células nervosas, afim de desenvolver novas técnicas de análise e tratamento de doenças relaccionadas com o sistema nervoso, de forma a desenvolver dispositivos capazes de melhorar a qualidade de vida dos seres humanos.

Impulsos nervosos podem ser aquiridos através de técnicas electrofisiológicas, como *Patch-clamp* ou *Microelectrode arrays* (MEA). No capítulo 2, encontram-se descritas diversas técnicas, que permitem adquirir o sinal neuronal. A mais recente técnica electrofisiológica é chamada de *gold-mushroom microelectrodes arrays*. Esta técnica reúne vantagens de métodos intra e extra celulares. As interfaces criadas nesta dissertação têm como base esta técnica.

A criação destes microelectrodos envolde várias técnicas como deposição fisica e química, litografia e técnicas de caracterização. Depois de optimizado o processo litográfico para fabricar poros com 2 μm no fotoresiste S1818 (10 mW-17%) e S1805 (10 mW-9%), foram electrodepositadas estruturas em forma de cogumelo a diferentes temperaturas, tempos de deposição e potenciais aplicados. A solução usada para electrodepositar as estruturas foi analisada através de ciclos voltamétricos, onde foi possivel identificar o potencial de nucleação e o potencial em que a deposição ocorre controladamente. Verificou-se também que a massa depositada varia com o valor do potencial aplicado, ou seja, para potenciais mais baixos que -1.0 V, há uma transferência de carga maior, o que origina uma massa depositada também maior. Dos testes em temperatura para diferentes potenciais aplicados, verifica-se que, um aumento na temperatura da solução de Orosene, cria um aumento do material depositado e que, para potenciais abaixo de -1.3 V, a deposição nos poros litografados é bastante complicada, porque no fotoresiste surgem físsuras, que levam à formação de filmes finos contínuos. Depois de analizadas as amostras em SEM, verificou-se que as estruturas criadas com -0.8 V, não

apresentam o topo em forma de um semi-hemisfério, estando apenas com essa forma estruturas criadas com -1.0 V e -1.3 V. No entanto, deposições a -1.3 V criam perdas no padrão desenhado. Assim, só deposições a -1.0 V conseguem ser suficientemente controladas para permitir a formação correcta das estruturas em todo o padrão desenhado.

Para -1.0 V encontraram-se as taxas de deposição para a temperatura ambiente (46 nm/min), para 30 ºC (62 nm/min) e para 35 ºC (85 nm/min). Medidas de impedância nos arrays fabricados mostraram um comportamento capacitivo para baixas frequências (6 μF). Depois da caracterização foram realizadas culturas de neurónios que através da funcionalização dos microelectrodos, aderiram à superfície, fazendo o envolvimento do microeléctrodo, criando uma ligação neurónio-microeléctrodo. Uma estimativa dos parametros biofísicos indicam que os eléctrodos criados possuem uma capacidade de 19.6 pF e uma resistência de 2.8 GΩ.

Por último, um pequeno estudo numérico do coeficiente de acoplamento é apresentado. Neste estudo, simulado através do software NI Multissim 14.0, foi obtido o valor do coeficiente de acoplamento para diferentes valores de *Seal Resistance* (R_{seal}) e *Junctional Resistance* (R_j).

Esta dissertação termina com as conclusões do trabalho, apresentando algumas perspetivas a serem desenvolvidas no futuro.

Palavras chaves: Neuroelectrónica, Biofísica, Sinais eléctricos, Impedâncias, Raio- x analise, Técnicas de litografia, Deposições de filmes finos, Electrodeposição, Micro e nanoelectrodos, Interfaces neuronais, Simulações.

Abstract

Bioelectronics is a subject of study, that joins Physics, Electronics, Biology and Chemistry. Its main goal is to develop sensors that interact with biological matter (cells, organs, etc) and are capable to transduce biological process in electrical responses, that can be recorded and studied. Neuroelectronics is a subject that studies neuron cells through devices created with micro/nanoelectrodes. The main goal of this subject is to understand the communication between nervous cells, as well as study the propagation of the nervous impulse inside the cells, in order to develop new techniques and decease treatments, to improve the life quality of human beings.

Nervous impulses can be recorded using Electrophysiological Techniques. Patch-clamp, MEA devices are two of the main example that we will describe in this thesis. The most recent electrophysiological technique, named gold-mushroom microelectrodes arrays, joining advantages of intra and extracellular methods will be our main focus. The interface created in this dissertation, is based on this technique. To created and study these microelectrodes one used several techniques, such as physical and chemical deposition, lithography and characterization techniques.

After optimizing the lithography process to obtain 2 µm sized circular holes in S1818 (10 mW-17%) and S1805 (10 mW-9%) photoresists, we electroplated structures with mushroom shape with different potentials, deposition times and temperatures. The electrodeposition solution was analysed through Voltammetric Cycles, allowing us to identify the nucleation and reduction regions. The value of the deposited mass was found to be highly dependent on the applied potential. For potential below -1.0 V the transferred charge is higher, leading to a higher value of the deposited mass. Increasing the solution temperature also led to an increase in the amount of deposited material. However, below -1.3 V, it is difficult to deposit inside the holes because the photoresist cracks which originates the deposition of a thin film. After SEM characterization, we verified that structures created with -0.8 V do not present the cap with semi-hemispherical shape. However, for -1.0 and -1.3 V, the grown cap presents the desired shape but, for electrodepositions at -1.3 V, the deposited array is usually damaged. For -1.0 V, we found the deposition rate for different values of temperature 23.5ºC (46 nm/min), 30ºC (62 nm/min) and 35ºC (85 nm/min).

Impedance measurements of the fabricated gold-mushroom microelectrodes arrays showed that, for low frequencies, the PBS-gMμEs has a capacitive behaviour (6 μF). After this characterization, neuron cultures were performed at i3S. The neurons were found to adhere to the electrode surface, doing the engulfment, resulting in the connection between neurons and microelectrodes. An estimative of the biophysical parameters indicates that the fabricated gMμEs have a capacity of 19.6 pF and resistance of 2.8 GΩ.

Finally, a numerical study of the coupling coefficient is presented. For this study, simulated in NI Multissim 14.0, the value of the coupling coefficient was obtained for different values of Seal Resistance (R_{seal}) and Junctional Resistance (R_j). This dissertation finish with conclusions on the developed work and proposals for future works.

Key-words: Neuroelectronics, Biophysics, Electrical signals, Impedance, X-ray analysis, Lithography Techniques, Deposition of thin films, Electrodeposition, Micro/nanoelectrodes, Neuronal Interfaces, Simulation.

Contents

Acknowledgements iii

Resumo iv

Abstract vi

List of Figures xi

List of Tables xv

Abbreviations xvi

Physical Constants xvii

Symbols xviii

1 Introduction 1
- 1.1 Motivation . . . 1
- 1.2 This thesis . . . 2
  - 1.2.1 Aim and Objectives . . . 2
  - 1.2.2 Thesis Organization . . . 2

2 Neuroelectronics 4
- 2.1 The nervous system . . . 4
- 2.2 Nervous Impulse . . . 6
- 2.3 Recording individual neuron's activity . . . 10
  - 2.3.1 Electrophysiological Techniques . . . 11
- 2.4 Gold-mushroom microelectrodes arrays . . . 14
  - 2.4.1 Fabrication of gMμEs . . . 15
  - 2.4.2 Engulfment mechanism . . . 18
  - 2.4.3 Functionalization of the gMμEs . . . 19
  - 2.4.4 Recorded Signal . . . 19

2.4.5 Cell-microelectrode electrical interface . . . 20
2.4.6 Biophysical parameters . . . 22

3 Experimental Methods **25**
3.1 Deposition Techniques . . . 25
3.1.1 Magnetron sputtering . . . 25
3.1.2 Electrodeposition . . . 27
3.2 Characterization Techniques . . . 30
3.2.1 Scanning Electron Microscopy (SEM) . . . 30
3.2.1.1 Energy Dispersive X-ray Spectroscopy (EDS) . . . 31
3.2.2 Profilometry . . . 31
3.2.3 X-Ray Diffraction (XRD) . . . 32
3.2.4 Four-terminal sensing . . . 33
3.2.4.1 Electrical Resistivity . . . 33
3.2.4.2 Electrical Impedance . . . 34
3.3 Lithography . . . 35
3.3.1 Photoresist . . . 36
3.3.2 Lithographic Process . . . 37
3.3.2.1 Spin coating . . . 37
3.3.2.2 Pre-bake . . . 38
3.3.2.3 Exposure . . . 38
3.3.2.4 Post Exposure Bake . . . 38
3.3.2.5 Develop . . . 39

4 Fabrication of gold-mushroom microelectrodes **40**
4.1 Lithography optimization . . . 40
4.1.1 Spin coating . . . 40
4.1.2 Exposure energy dosage . . . 41
4.1.2.1 $S1818$ photoresist . . . 42
4.1.2.2 $S1805$ photoresist . . . 43
4.2 Gold electrodeposition . . . 44
4.2.1 Voltammetry . . . 44
4.2.2 Electrodeposition curves and efficiency . . . 44
4.3 Electrodeposition in micro-pores . . . 48
4.3.1 Influence of potential and temperature on the gMμEs morphology . . . 48
4.3.2 Electrodepositions at -1.0 V . . . 52
4.3.2.1 *Minimum exposure energy* . . . 52
4.3.2.2 *Structures grown with different deposition times* . . . 52
4.3.2.3 *Structures grown with different temperatures and deposition times* 54
4.4 e-beam lithographed arrays . . . 56

5 Interfacing electrodes and neurons **60**
5.1 Produced sample . . . 60
5.2 Characterization of the gold-mushroom microelectrodes arrays . . . 61
5.2.1 X-ray diffraction . . . 61

5.2.2 Electrical Resistivity and Impedance 62
5.3 Cell culture 65

6 Electrical Simulations **71**

7 Conclusion and Future work **75**

A Appendixes **81**

List of Figures

1.1 An artificial robotic hand (adapted from [1]). 1

2.1 The human nervous system (adapted from [2]). 4
2.2 The cerebral lobes (adapted from [3]). 5
2.3 Schematic of a neuron where the main constituents are indicated. 6
2.4 Constituents of the cell membrane. Two types of components play important electrical roles in a neuron's membrane. The lipid bilayer is an impermeable barrier to inorganic ions. The ion channel is a protein that forms a hole through the membrane, allowing ions to pass (adapted from [4]). 7
2.5 Two electrodes measurement of the difference of potential between the interior of the cell and the extracellular fluid. The graph shows the measurement of the membrane potential at rest (adapted from [5]). 8
2.6 Equivalent circuit for a cell membrane according to the Hodgkin-Huxley model [4]. 9
2.7 The propagation of a nervous impulse (adapted from [4][5]). 10
2.8 Recording of neural activity using intracellular and extracellular methods (adapted from [6]). 11
2.9 Recording neuronal activity by (a) sharp glass electrode and (b) patch-clamp (adapted from [6]). 12
2.10 Vertical Nanowire: Schematic of the technique: (a) vertical nanowire [6]; (b) SEM image of a nanostuctured array. (c) SEM image of the coupling between a neuron and a nanowire. (d) Signal recorded [7]. 13
2.11 Nanowire Transistor: (a) Recorded FET signal; (a1) left: before penetration of the cell; (a2) right: a single intracellular recorded potential. (b) SEM imaging of the FET device (adapted from [6]). 13
2.12 Microelectrode arrays (MEAs): (a) a SEM image of a nanopillar array; a1) a neuron engulfment of a nanopillar; a2) the signal recorded by the nanopillar. (b) Flat electrode array; b1) the signal recorded by the flat electrode. (c) SEM image of a carbon nanotube with an adhered neuron; c1) the recorded signal. (d) SEM image of gold mushrooms engulfment by a neuron; d1) schematic of the technique; d2) the action potential recorded by gold-mushrooms micro-electrodes (adapted from [6][8][9][10][11][12]). 14
2.13 The comparison between MEA devices and gold mushrooms-shaped microelectrode arrays (adapted from [13]). 15
2.14 The sequential steps to produce the gMμEs: (a) silicon substrate; (b) gold thin film deposition; (c) spin coating of the photoresist; (d) exposure and development; (e) electrodeposition and (f) strip of the photoresist. 16

2.15 Scanning electron microscope images of neurons grown on a matrix of gMμEs: (a) a low magnification image of a neuron's cell and an extending neurite on a matrix of large gMμEs; (b) the neurites growing on top of the gMμEs and (c) the neurites on top of a mushroom cap appear to tightly adhere to the surface [14]. . 17
2.16 Silicon substrate with patterns of nano gold-mushroom arrays for neuron guidance: (a) schematic of a guided neuron by a pattern composed by gold - mushroom microelectrodes; (b) zoom-in view of the pattern; (c) SEM image of the neuron guided through the microelectrodes; (d) Confocal microscope image [15]. 17
2.17 The engulfment of a gold microelectrode by a cell (adapted from [13]). 18
2.18 Recorded Signal by gMμEs in the "in-cell" configuration. (a) Schematic of the experimental set up; (b) calibration pulses applied to the cultured cells recorded by intracellular and gold-mushroom electrodes; (c) hyperpolarization pulses applied to the neuron and recorded by intracellular and the gold-mushroom electrodes; (d),(e) and (f) depolarization pulses and signal recorded by the two electrodes. The red line corresponds to records by the intracellular electrode; the blue line represents the results for the gMμEs, while the purple line corresponds to the injected current [16]. 20
2.19 Electrical model of the interface between the neuron cell and the gold mushroom-shaped microelectrode: (a) schematic of the interface, where the neuron cell realizes the total engulfment; (b) schematic of the interface, where the neuron fails the engulfment; (c) equivalent electrical circuit of the total engulfment; (d) equivalent electrical circuit of the partial engulfment (adapted from [14][17]). . . . 21
2.20 Simulation of the electrical properties of the interface between a neuron cell and a gMμE: (a) coupling coefficient as a function of the seal resistance for high and (b) low frequencies; (c) maximum membrane depolarization as a function of the stimulation voltage via gMμE for high (dot points) and low (square points) frequencies (adapted from [18]). 22

3.1 Schematics of a Magnetron Sputtering system (adapted from [19]). 26
3.2 The image of Magnetron Sputtering system used in this work: (a) INESC-MN and (b) INL. 26
3.3 The flux of ions in the electrodeposition process [20]. 27
3.4 Hydrogen electrode versus Ag/AgCl and SCE standard electrodes. 28
3.5 Three-electrode configuration used for potentiostatic electrodeposition. In (a) have the schematic of the technique and (b) the photo of the electrodeposition set-up (adapted from [21]). 29
3.6 Scanning Electron Microscopy (SEM) (adapted from [22]). 31
3.7 $DektakXT^{TM}$ profilometer: (a) set-up; (b) support of the sample and (c) cantilever and camera. 32
3.8 The XRD diffraction:(a) are the schematic of incident and diffracted beam and (b) are the diffraction pattern obtained. 33
3.9 Four-point measurement of the resistivity. 33
3.10 The impedance analyser. 34
3.11 Lithography process. 35
3.12 Pattern produced by Positive and Negative Photoresist after expose to the UV-light. 36

3.13 Sequential steps of a spin coating process: (a) silicon substrate with an Au thin film; (b) dropping photoresist on top of the sample; (c) spin coating and (d) final sample coated with photoresist. 37

4.1 The spin coating process implemented for our samples: (a) the sample fixed in the spinner and (b) the photoresist placed in the sample surface. 41
4.2 The exposure step: (a) Pattern designed in AutoCad and (b) optical lithography system. 42
4.3 Optical microscope images of the transferred patterns produced in $S1818$ with (a) 2 and (b) 1.5 µm. 43
4.4 Optical microscope images of the transferred patterns produced in $S1805$ with 2 µm. 43
4.5 The voltammogram of the Orosene solution. The cycles were performed with different scan ramp rates, and the potential changed from $+2.0$ up to -2.0 V in scan rates of (a) 10 mV/s; (b) 20 mV/s; (c) 30 mV/s and (d) 40 mV/s. 45
4.6 The electrodeposition set-up in a cell. 46
4.7 Electrodeposition curves obtained at different potentials. 46
4.8 The total charge transferred in the electrodeposition process at : (a) -0.8 V, (b) -1.0 V , (c) -1.3 V and (d) -1.6 V as a function of the electrodeposition time. The deposition area was 0.20 cm^2. 47
4.9 Cap diameter of the gold-mushrooms grown with different potential as a function of electrolyte temperature: (a) -0.8 V, (b) -1.0 V and (c) -1.3 V. 49
4.10 SEM micrographs of the gold-mushrooms microelectrodes plated at different temperatures and potentials. The structures were created with S1805. 50
4.11 Top view of the produced gold-mushroom microelectrode. 51
4.12 SEM images of the microelectrodes produced by two different pixel pulse durations: (a) 12% and (b) 15 %. 52
4.13 SEM image of the microelectrodes produced at 10 mW with 15%. (a) Array of microelectrodes;(b), (c) and (d) microelectrodes seen at different positions. . . . 53
4.14 Arrays obtained for different deposition times with the electrodeposition temperature (23.5ºC) and potential (-1.0 V) constant. 54
4.15 The cap diameter obtained for different times at -1.0 V. 55
4.16 SEM images of electrodeposited structures at -1.0 V during 15 min, at different temperatures: (a) 23.5, (b) 30 and (c) 35 °C. 56
4.17 Nano holes transferred to PMMA. 57
4.18 The gold-mushroom grown in nano holes: (a)-(b) top-view of the 300 nm and 500 nm arrays; (c) and (d) are the zoom-in images of the gold-mushrooms for structures with 300 nm and 500 nm, respectively. The inserts in (a) and (b) represent the distribution of the cap diameter. 58
4.19 A cross-section view of the gMμEs grown with (a) and (c) $300\ nm$; (b) and (d) $500\ nm$. 59
4.20 SEm images of nano-mushroom electroplated at -1.0 V, during 4.5 min. 59

5.1 SEM characterization of the produced gold-mushrooms microelectrodes arrays for (a)-(c) 70 min and for (d)-(f) 94 min. 61
5.2 X-ray spectrum of the sample used to culture neurons cells. 62

5.3 The set-up for measure the impedance. 63
5.4 Impedance of PBS and electrodes, for different temperatures as a function of frequency. 64
5.5 The values of resistance and capacitance for the PBS and electrodes system. . . 65
5.6 Thermal evolution of the PBS solution. 65
5.7 Microscope image of the neurons placed in the gold-mushroom microelectrodes arrays. 66
5.8 SEM micrographs of the neuron culture in the microelectrode electroplated for 70 min. 67
5.9 SEM micrographs of the neuron culture in the microelectrode electroplated for 94 min. 68
5.10 EDS analysis, for the sample electrodeposited during (a), (c)70 min and (b), (d) for 94 min. 69

6.1 Schematic of the engulfment of a gold-mushroom microelectrode by a neuron cell. The electrical circuit represented is an equivalent for the situation. 72
6.2 Electrical circuit implemented in NI Multisim 14.0. 73
6.3 Coupling coefficient for pulses of current of 1 nA at 100 Hz. 74
6.4 Maximum depolarization acquired by the gold-mushroom microelectrode arrays through changing the stimulus intensity. 74

List of Tables

2.1 Characteristics of the methods for recording and stimulation neurons (adapted from [6]). 14

4.1 The values of the final thicknesses for the two photoresists prepared with same operation values. 41
4.2 Deposited an Theoretical gold mass values for four different potentials. 47
4.3 Size measurements of the produced gold-mushrooms microelectrode arrays. . . 51

5.1 Estimated areas of the stalk, cap, rim and gold-mushroom microelectrode for 70 and 94 min of electrodeposition. 70

Abbreviations

gMμEs	gold-mushroom microelectrodes arrays
CNS	Central Nervous System
PNS	Peripheral Nervous System
EDS	Energy Dispersive X-ray Spectroscopy
SEM	Scanning Electron Microscopy
SE	Secondary Electrons
BSE	Backscatter Electrons
XRD	X-ray diffraction

Physical Constants

Faraday's Constant	F	$=$	$96845.33289(59)\ C.mol^{-1}$
Ideal gas constant	R	=	$8.3144598(48)\ J.K^{-1}.mol^{-1}$

Symbols

T	Temperature	°C
C_e	Ion concentration extracellular medium	mol/m^3
C_i	Ion concentration in intracellular medium	mol/m^3
ρ	Electrical Resistivity	$\Omega.m$
Z	Impedance	Ω
t	time	s
I	Electrical current	A
I_i	Ionic current	A
V	Potential difference	V
A	Area	μ^2
C	capacitance	F
R	Electrical Resistance	Ω

Para Arminda Marcelo, José Cerquido e Manuel Cerquido

Chapter 1

Introduction

1.1 Motivation

Bioelectronics is a subject of study that joins Physics, Biology, Chemistry and Electrical engineering [23]. The main goal of Bioelectronics is to develop biosensors that transduce biological process in the form of electrical signals [24]. Many studies have been developed in the last decades, including the creation of artificial systems like robotic hands capable of moving biomimetically (Fig. 1.1) [1].

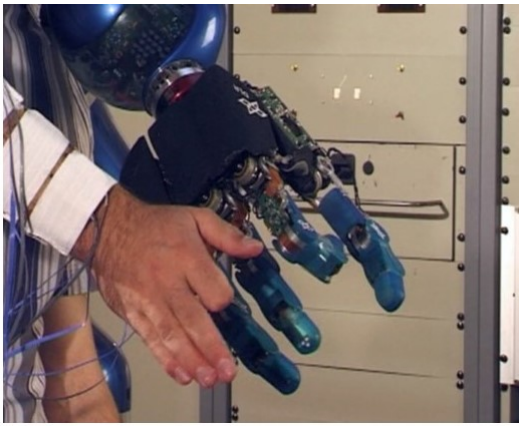

FIGURE 1.1: An artificial robotic hand (adapted from [1]).

A highly relevant branch of bioelectronics is neuroelectronics. Neuroelectronics is a subject that studies the interface between the human nervous system and electronic devices. Its main focus is to understand and describe how nervous cells interact and communicate in the nervous system. Although techniques like tomography can give a detail overview about the morphological aspects and structure of the brain, they do not provide relevant information about the

communication between different cells. In that respect, there are several techniques, named electrophysiological techniques, that allow access to the cell. These have allowed us to obtain important biophysical parameters of the cell membrane, like its capacitance and resistance, and record nervous signals. Furthermore, with the development of nano/micro technologies, it is now possible to create hybrid interfaces that allow access to the cell. Microelectrodes array (MEA) devices recently demonstrated a great potential for cell studies. These devices are composed by electrodes, with a well defined geometry, that allows recording and stimulating the neuron cell.

The study of this subject allowed me to, understand and acquire new knowledge in clean-room environment, materials science, electronics and critical aspects on neuron cells.

1.2 This thesis

1.2.1 Aim and Objectives

The aim of this dissertation covers a wide range of domains related to Physics Engineering, Biophysics and Materials Science, specifically on neuroelectronic interfaces. We will explore in depth the most recently electrophysiological technique, named gold-mushroom microelectrodes arrays (gMμEs). The study of this new technology comprises both the theoretical aspects and manufacturing processes.

To accomplish this, the following objectives were defined:

- To produce and optimize gold-mushroom microelectrodes arrays;
- To characterize the morphological, crystallographic and electrical properties of the fabricated gMμEs;
- To culture neuron cells and to create an interface between the neurons and the electrodes.

1.2.2 Thesis Organization

This document starts with a theoretical introduction to the intrinsic Physics behind the gMμEs technology (Chapter 2). Following this overview, in Chapter 3, we present the techniques used to produce the gold-mushroom microelectrodes arrays (including electrodeposition and lithography steps). The optimization of the exposure conditions to obtain the desired pattern and

to electrodeposit the structures is presented in Chapter 4. The characterization of the microelectrodes and the design of the interface between neurons and the gold-mushroom microelectrodes arrays can be found in Chapter 5. In Chapter 6, we will describe electrical simulations of the neuron-interface, to study how the coupling coefficient changes with the change in biophysical parameters and understand what is the input needed to record a neuronal signal with quality. Finally, in Chapter 7 we summarize the presented information and provide potential improvements.

Chapter 2

Neuroelectronics

2.1 The nervous system

The nervous system allows us to recognizes, understand, and respond to the world around us. The brain, spinal cord and nerves are constituents of the central nervous system (CNS) that, together with the peripheral nervous system (PNS) constituted by the sensory organs, ganglia (clusters of neurons) and the nerves that connect the two subsystems, are responsible for the control of the communication between different parts of the body, (Fig. 2.1). Fundamentally, the CNS receives information from all the organs and tissue within the body, analyzes this information and transmits appropriate responses back to the organ, while the PNS accounts for all the cells that bring information into and out of the CNS.

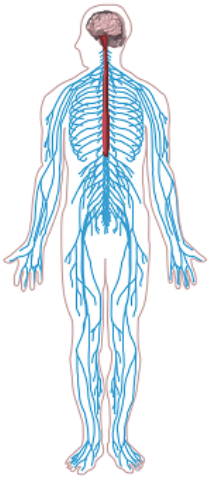

FIGURE 2.1: The human nervous system (adapted from [2]).

The brain is the central organ of the nervous system and is responsible for receiving and processing the information, initiating responses and controling all the emotions and motor reactions. But, how does it store and process the information? The brain is one of the greatest mysteries faced by mankind, with several large scale international projects being recently initiated to study the brain, including the *Human Brain Project* (European Union), the *BRAIN Initiative* (United States), *MINDS* (Japan), *BrainLinks-BrainTools* (Germany), or the *Blue Brain Project* (IBM; industry-driven). These have the main goals of mapping and understanding the human brain, improving the treatment of brain diseases or understanding the human body [25].

The human brain is composed by different regions, each responsible for different actions. The two largest regions are the left and the right hemispheres. The left hemisphere is responsible for logical thinking and verbal communication (speak) while in the right side we have emotions, feelings and creativity.

The hemisphere is then constituent by five lobes: the *Frontal Lobe*, the *Occipital Lobe*, the *Parietal Lobe*, the *Temporal Lobe* and the *Limbic Lobe*, Fig. 2.2. Each one of these lobes has a specific function. The *Frontal Lobe* is responsible for control attention, decision making, motor planning, initiation of voluntary movements and has an important role in language. The lobe responsible for the visual function and the processing of visual information is the *Occipital lobe*. For the capacity of sensing, spatial orientation, perception and language comprehension we have the *Parietal lobe*. The *Temporal lobe* processes aspects of learning and memory as well as assisting the occipital lobe in higher order processing of visual information. The last one, the *Limbic lobe* is connected with the Temporal, Parietal and Frontal lobes. This part of the brain is responsible for emotion responses, drive-related behavior and memory. These components of the brain are entirely connected, and those connection permit an efficient control of the human body [26].

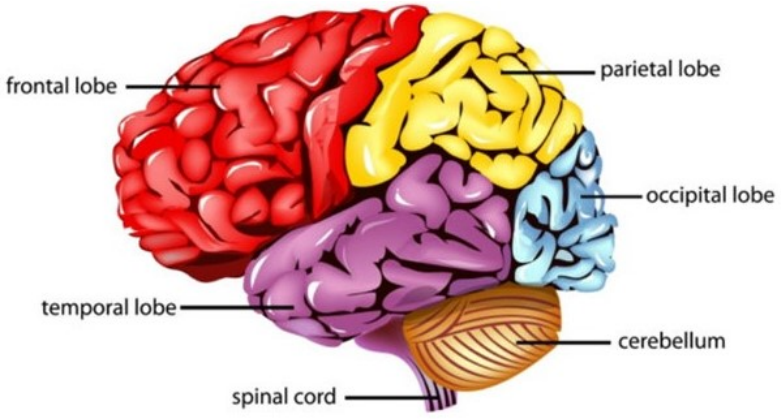

FIGURE 2.2: The cerebral lobes (adapted from [3]).

But, how then does the brain control the entire human body?

The brain is composed in its most fundamental part by neurons and it is estimated that the brain has over 100 billion of neurons. Connections in the nervous system are made through these neurons, that receive a chemical or electrical impulse, and transmit these impulses to other neurons.

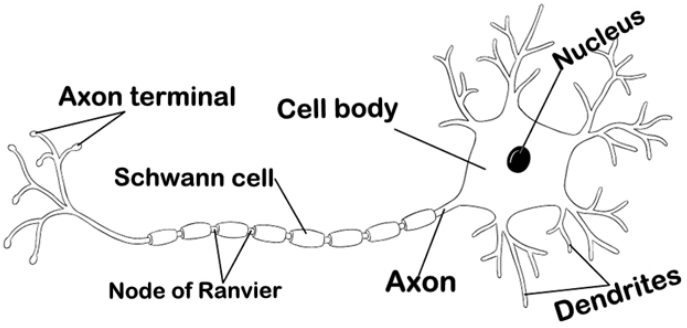

FIGURE 2.3: Schematic of a neuron where the main constituents are indicated (adapted from [27]).

Figure 2.3 shows a schematic of a neuron. Neurons are constituted by a cell body, a nucleus, dendrites, Schwann cell, nodes of Ranvier and an axon. The dendrites are responsible for receiving the information from adjacent neurons. The axon has a variable length and conducts the information along the neuron. However, there are neurons that do not have an axon and, in this case, the dendrites are responsible for transmitting the information to other neurons. A node of Ranvier is an interruption in the myelin sheath where actual conduction and voltage gated channels occur. The myelin sheath's main function is to allow the communication between neurons and ensures that the transmission between neurons is fast. The communication between neurons occurs at the *synapses*, that can be chemical or electrical. The flow of communication between neurons then depends on the membrane potential of adjacent cells [28].

2.2 Nervous Impulse

The ability of cells to receive, transmit and act on signals from beyond the membrane is essential for life. These signals represent information that is detected by specific receptors and converted into a response. This conversion always involves a chemical process and this signal transduction is a property of living cells [29]. There are three important factors to account for the extraordinary sensitivity of biological signal transducers. Those factors are the high affinity of receptors for signal molecules, the co-operation in the ligand-receptor interaction and signal amplification. The receptor captures the signal, amplifies and transmit it into the cell [29]. We

can classify the transduction systems into six basic signal mechanisms. These mechanisms are denominated by *Gate ion channel*, *Receptor enzymes*, *Serpentine receptors*, *Receptor with no intrinsic enzyme activity* and *Adhesion receptor*. The *Gate ion channel* consists in a channel in the plasma membrane that opens and closes as a response to the binding of chemical ligands or changes in the trans-membrane potential. This mechanism is the simplest signal transducer [29]. The *Receptor enzymes* is an enzymatic process, that occurs when a ligand binding to the extracellular domain stimulates enzymatic activity in the intracellular domain. When we have an external ligand binding to the receptor and this indirectly active enzymes that generates intracellular second messenger, we talk about the *Serpentine receptors* mechanism. *Receptor with no intrinsic enzyme activity* contacts with cytosolic protein kinase, which activates a gene-regulating protein that changes gene expression. The *Adhesion receptor* binds molecules in extracellular matrix, changes conformation, thus altering its interaction with cytoskeleton [29].

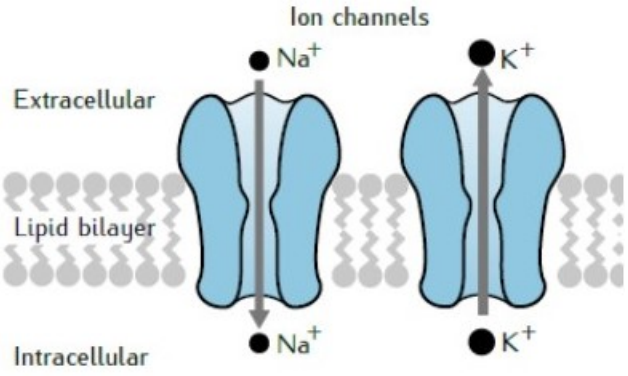

FIGURE 2.4: Constituents of the cell membrane. Two types of components play important electrical roles in a neuron's membrane. The lipid bilayer is an impermeable barrier to inorganic ions. The ion channel is a protein that forms a hole through the membrane, allowing ions to pass (adapted from [4]).

At the cells, there is a barrier between intracellular and extracellular mediums that is dominated by cell membrane (Fig. 2.4). The cell membrane has a thickness of 40 Å and is constituted by channels (*ions channels*) that permit the exchange of ions between the intracellular and extracellular mediums. When these *ions channels* are open, ions can flow from the intracellular medium to the extracellular medium, or vice-versa. When the channels are in the closed state, the membrane becomes impermeable and ions cannot pass through it. The entry of ions is selective and creates an asymmetric distribution of ions between the two mediums, giving rise to an electrical potential, denominated by membrane potential [4][5].

When the system is in equilibrium, the number of ions flowing to the intracellular medium is equal to the number of ions flowing in the opposite direction. At equilibrium, the value of the

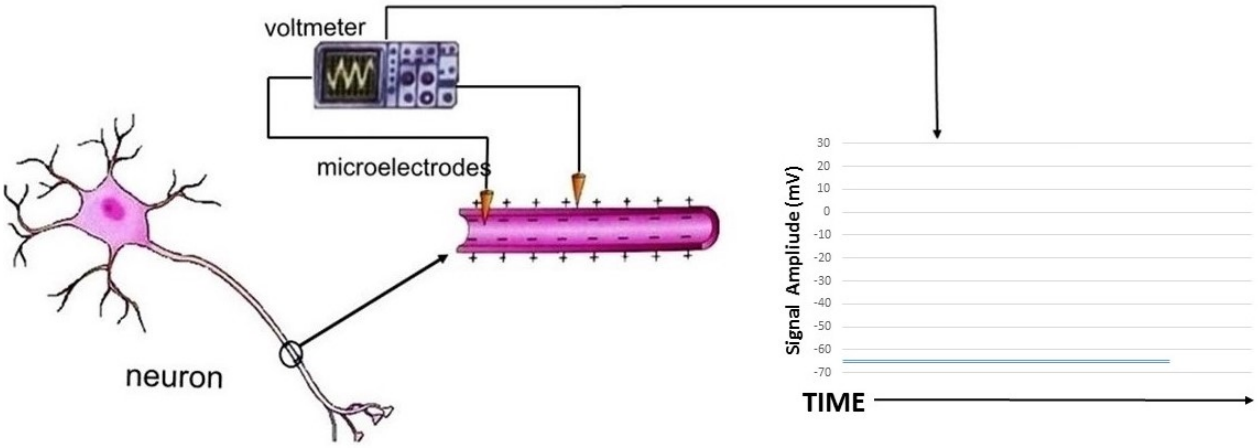

FIGURE 2.5: Two electrodes measurement of the difference of potential between the interior of the cell and the extracellular fluid. The graph shows the measurement of the membrane potential at rest (adapted from [5]).

equilibrium potential for each ion species present in the medium can be obtained according to the Nernst's equation [4]:

$$V = \frac{RT}{zF} \ln \frac{c_e}{c_i}, \tag{2.1}$$

where *R* is the gas constant, *F* the Faraday constant, *T* the absolute temperature, *z* the charge of each ion and c_e and c_i are the concentration at the extracellular medium and intracellular medium, respectively.

Ion pumps maintain different ionic concentrations between the inside and the outside of the cell. For example, at rest the concentration of sodium is larger outside, while the concentration of potassium is larger inside. This generates a concentration gradient for different ion types, and leads to a polarization of the membrane. The resulting rest potential has a value of $V_m = -65$ mV, i.e. inside the cell the potential is more negative than outside [29][4].

Through time, biologists tried to understand how nervous information or nervous impulses are processed. Nervous impulses are transmited by an electrical signal and biophysicists have developed an equivalent electrical circuit that has the behaviour of *ions channels* [4][30]. Figure 2.6 is the equivalent circuit of the cell membrane according to the Hodgkin-Huxley model. In this model there are three types of ionic currents: a potassium current, a sodium current and the leak current that is associated mainly to the chloride ions.

From this equivalent circuit, the membrane current is given by [4]:

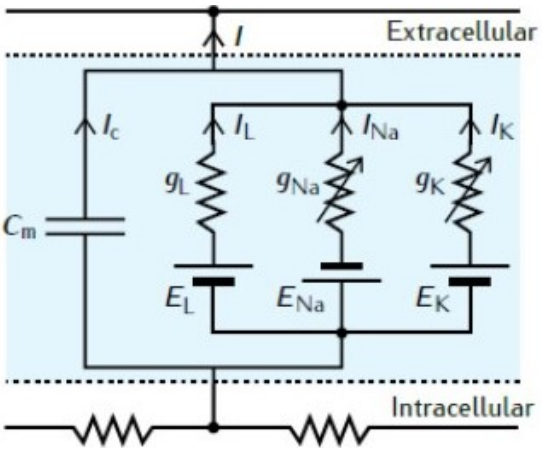

FIGURE 2.6: Equivalent circuit for a cell membrane according to the Hodgkin-Huxley model [4].

$$I = I_c + I_i = C_m \frac{dV}{dt} + I_i, \tag{2.2}$$

where *I* is the membrane current, I_c is the capacitive current and the total ionic current is represent by I_i. The total ionic current is the sum of potassium, sodium and leak currents. The expression for the total ionic current is then given by [4]:

$$I_i = I_{N_a} + I_K + I_L = g_{N_a}(V - V_{N_a}) + g_K(V - V_K) + \bar{g_L}(V - V_L). \tag{2.3}$$

In Eq. (2.3), V_{N_a}, V_K and V_L are the sodium, potassium and leak equilibrium voltages, respectively, that can be obtained using Eq. (2.1). The g_{N_a}, g_K and $\bar{g_L}$ are the conductance of sodium, potassium and leak, respectively. The bar in the leak conductance indicates that this conductance is constant, while the values of g_{N_a} and g_K depend of the previous event of the membrane potential [4]. Through these equations we can calculate the membrane potential and the total current in the membrane.

In the nervous system we have an electrical impulse that is transmitted from the end of an adjacent cell to the cell body of the neuron that in turn propagates this signal to another neuron [29]. This propagation is schematically shown in Fig. 2.7. Two types of voltage-gated ion channels are necessary for this mechanism to work: *voltage-gated Na*, *K channels*. The *voltage-gated Na channels* are channels that close when the membrane is at rest, but open when the membrane is depolarized locally. When the *Na channels* open, that induces the opening of the *K channels*, which create an exit of K ions and the local repolarization of the membrane. When the electrical impulse reaches the axon, the *Ca channels* are opened and Ca ions enter the intracellular medium. Through the entrance of Ca ions, neurotransmitters are

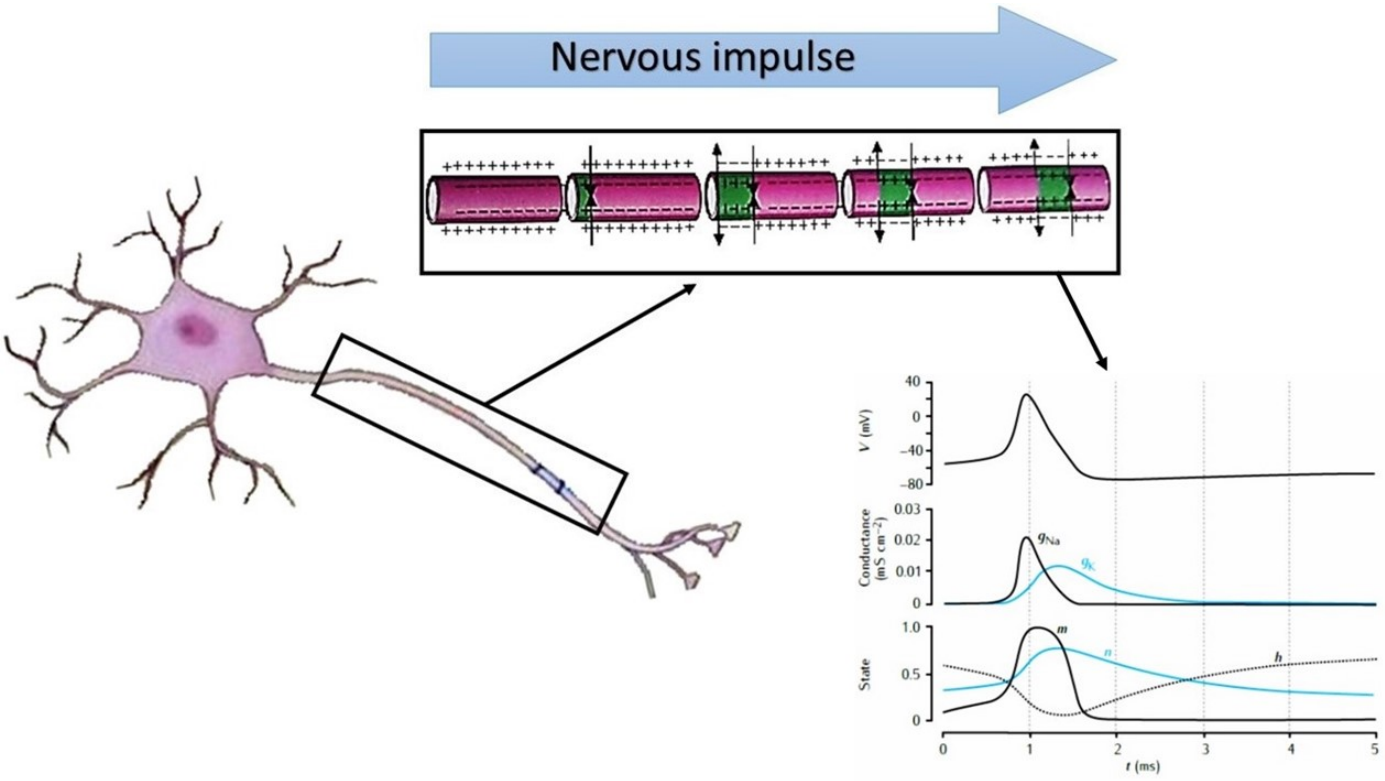

FIGURE 2.7: The propagation of a nervous impulse (adapted from [4][5]).

released in the synaptic zone. These neurotransmitters are received by another neuron and information passed to the next cell [29].

The information that passes between neurons, as mentioned above, is an electrical signal that creates changes in the polarization of the cell membrane. It is thus highly desirable and interesting to measure and acquire these propagating electrical signals. Several techniques, denominated electrophysiological techniques, were developed for this end. In the following section the most important techniques, as well as their advantages and disadvantages, will be presented.

2.3 Recording individual neuron's activity

Technological developments have allowed the acquisition of new knowledge by human beings. Due to these improvements, we are at the tipping point of connecting electronic and biological elements [25][31]. For this, several methods are presently available, including intracellular and

extracellular techniques, optical imaging, magnetic resonance imaging, electroencephalography, electrocorticography and magnetoencephalography that allow recording neuronal activity [6].

Electroencephalography, optical imaging, magnetic resonance imaging, electrocorticography and magnetoencephalography are techniques that record the activity of a set of neurons, and thus do not have the resolution to record single neuron activity [6]. These techniques are often used in medicine to detect mental diseases. For higher resolution studies, i.e. the recording of single neuronal activity, we have intracellular and extracellular methods (Fig. 2.8), each having its own advantages and disadvantages. Intracellular methods are techniques that have a good coupling with the cell, a high signal-to-noise ratio and provide the measurement of voltages in the cell without distortion through time. However, this type of technique requires bulky manipulators and the recording time is restricted due to cell instability. This method is complex and invasive because it is necessary to penetrate the cell [6][32].

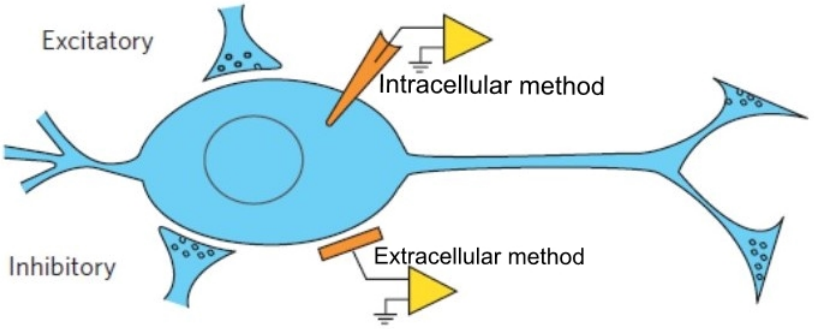

FIGURE 2.8: Recording of neural activity using intracellular and extracellular methods (adapted from [6]).

On the other hand, extracellular methods are non-invasive, allow recording neural activity for long periods of time without damaging the plasma membrane and can stimulate and record simultaneously. However, these methods do not allow to detect neuronal activity bellow the threshold, have low signal-to-noise ratio and record action potentials only. The former limitation severally restricts the analysis of neuronal networks in culture or *in vivo* [6][32][16][33].

2.3.1 Electrophysiological Techniques

Sharp-glass electrode. This technique can be applied in various cell types, has a good coupling coefficient and the electrode is inserted in a mechanical form in the cell [6]. The application of this technique is made through the penetration of the cell membrane with a tip. The tip is a

micro needle that has an electrode that measures the cell activity [34]. In Fig. 2.9 we can see the schematic of the sharp-glass electrode. The orange cone is our tip and we see that the electrode is inside the cell.

This technique has a limited recording time due to the instability caused to the cell. Another limitation is the appearance of bubbles near the tip that make the electrodes unusable. Another problem resides in the exchange of one electrode for another due to the improper resistance or tip clogged [34][35].

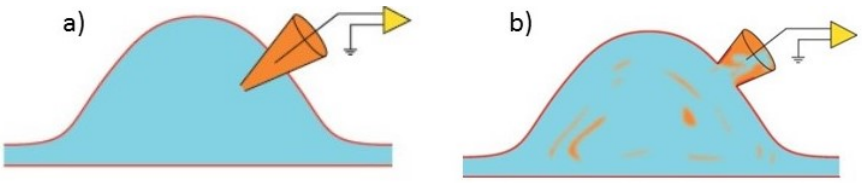

FIGURE 2.9: Recording neuronal activity by (a) sharp glass electrode and (b) patch-clamp (adapted from [6]).

Patch-clamp electrodes (whole cell). Patch clamping involves contact between a glass pipette tip and the cell membrane. When in contact with the membrane, suction is applied to the glass pipette and the cell membrane is aspirated, leading to the rupture of the membrane, that permits access to the interior of the cell. This allows the measurement of the ionic current in the whole cell membrane [36][37]. In Fig. 2.9(b), we have a schematic of this technique.

Through the pipette it is possible to measure and record the ionic current because the patch clamp is connected to an amplifier. The recording is made in a single-channel activity or by isolating the patch from the environment and removing the pipette from the cell [26]. This technique can be applied in various cells types, has a good coupling coefficient and the electrode is mechanically inserted in the cell [6]. This technique requires precision on the micro-manipulation, vibrational reduction and some experience by the experimentalist [38].

Vertical Nanowire electrode array. Vertical nanowires are very thin structures that penetrate the cell without causing much damage and permit measuring the cell activity and composition directly through its electrical properties, with molecular sensors or through probing a cellular component. These nanostructures may arise as single elements or as an array, as shown in Fig. 2.10 [12][7].

The fabrication of this type of structures can be made by semiconductor manufacturing techniques. Depending on the fabrication of the structure that is used, we can have a Nanowire Field Effect Transistor (FET; Fig. 2.11), that consists in a tube that penetrates the cell membrane and

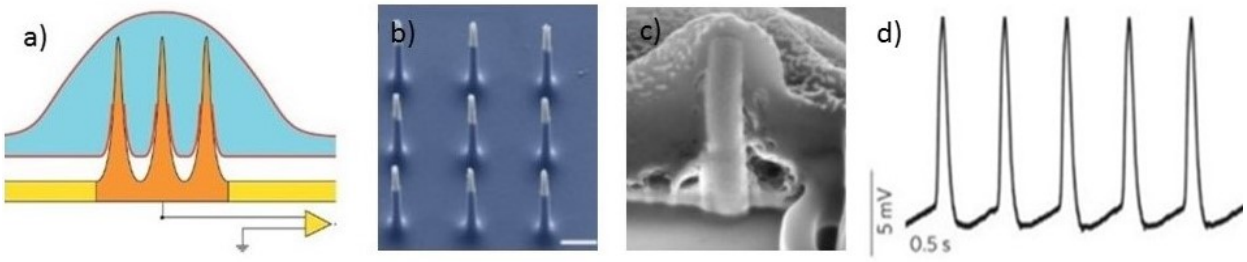

FIGURE 2.10: Vertical Nanowire: Schematic of the technique: (a) vertical nanowire [6]; (b) SEM image of a nanostuctured array. (C) SEM image of the coupling between a neuron and a nanowire. (d) Signal recorded [7].

records the membrane potential; Silicon Nanowires, which use the same mechanism as the Nanowire FET to access the cell, but require the use of an amplifier to amplify the recording signal [7][10].

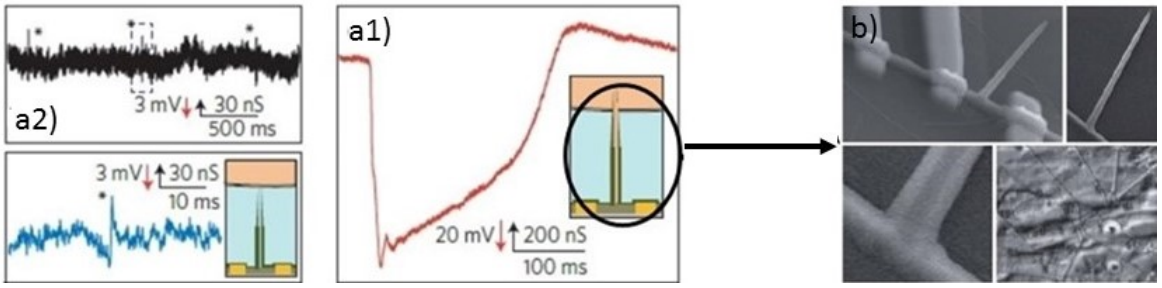

FIGURE 2.11: Nanowire Transistor: (a) Recorded FET signal; (a1) left: before penetration of the cell; (a2) right: a single intracellular recorded potential. (b) SEM imaging of the FET device (adapted from [6]).

MEAs. Microelectrode arrays (MEAs) are devices that allow the measurement and recording of neural signals through the connection between neural cells and electric circuits. In microelectrode arrays (Fig. 2.12) the success of extracellular recording depends on the distance and the stability between the electrode and the cell membrane. This type of device is non-invasive, with the exception of the nanowire and carbon nanotube arrays [39]. The precautions that must be taken with this technique are: that the electrode size has to be small for the connection with an individual neuron to occur; one must ensure a low signal-to-noise ratio caused by the position of the electrodes relative to the cell; and sometimes there are glial cells that prevent the measurement of the cell activity by the electrodes [7].

Table 2.1 shows the generic characteristics of several techniques. Analysing the table, we conclude that planar MEAs devices allow stable recording for a long period of time, in comparison with the others techniques. On the other hand, gold mushroom-shaped microelectrode arrays

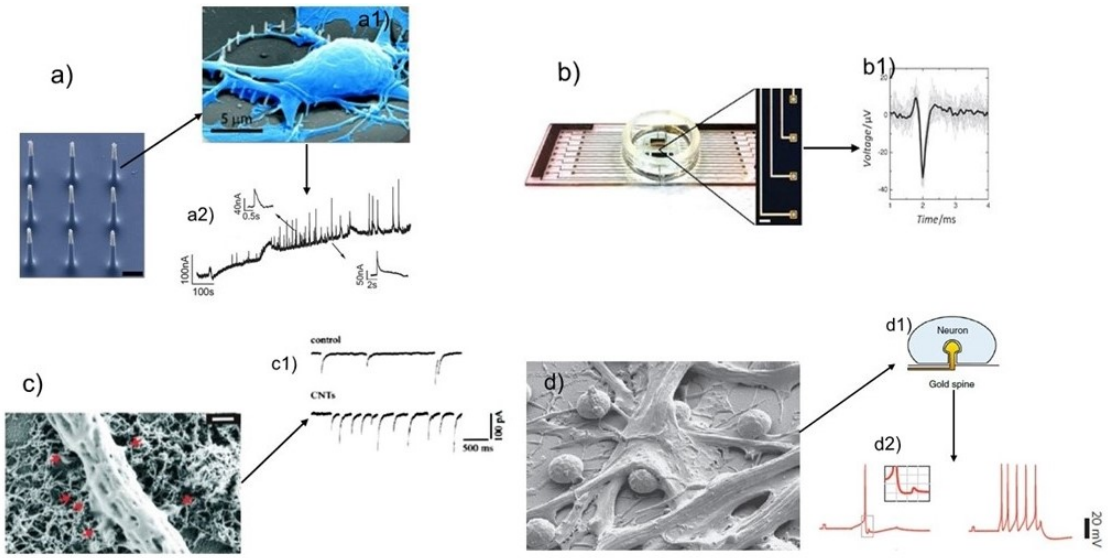

FIGURE 2.12: Microelectrode arrays (MEAs): (a) a SEM image of a nanopillar array; a1) a neuron engulfment of a nanopillar; a2) the signal recorded by the nanopillar. (b) Flat electrode array; b1) the signal recorded by the flat electrode. (c) SEM image of a carbon nanotube with an adhered neuron; c1) the recorded signal. (d) SEM image of gold mushrooms engulfment by a neuron; d1) schematic of the technique; d2) the action potential recorded by gold-mushrooms micro-electrodes (adapted from [6][8][9][10][11][12]).

TABLE 2.1: Characteristics of the methods for recording and stimulation neurons (adapted from [6]).

Technique	Cell type Studied	Coupling coefficient	Stable record
Sharp-glass electrode	Multiple	1	Hours
Patch-clamp electrode (whole cell)	Multiple	1	Hours
Planar MEA	Multiple	0.001-0.01	$>$ months
Gold mushroom-shaped MEA	Neurons	0.5	2 days
Vertical Nanowire electrode arrays	Neurons	0.3	10 min

[Fig. 2.12(d)] is the technique that has the best trade off between coupling coefficient and stable recording time. Gold mushroom-shaped MEAs allow stable measurement of neuronal signals up to two days. It was therefore the technique chosen to use in this thesis and, in the next section, we will present a detailed overview about this technique and the way to implement it.

2.4 Gold-mushroom microelectrodes arrays

Gold mushroom-shaped microelectrodes arrays is a technique that, by its characteristics, is awakening an intensive study and implementation. This technique is an extracellular method that has the characteristics of intracellular techniques and is applied only to neurons. Through

gold mushrooms-shaped microelectrodes arrays it is possible to apply high voltages without damaging the cell and record and stimulate cells during days [6]. Thus, this new neuroelectronics interface is able to perform "in-cell" recording, allowing multisite, long-term recordings of action potentials and subthreshold potentials, from individual neurons, with excellent signal-to-noise ratio. This electrophysiological technique allows effective stimulation, gathering advantages of the intra and extracellular electrophysiological techniques [6][16].

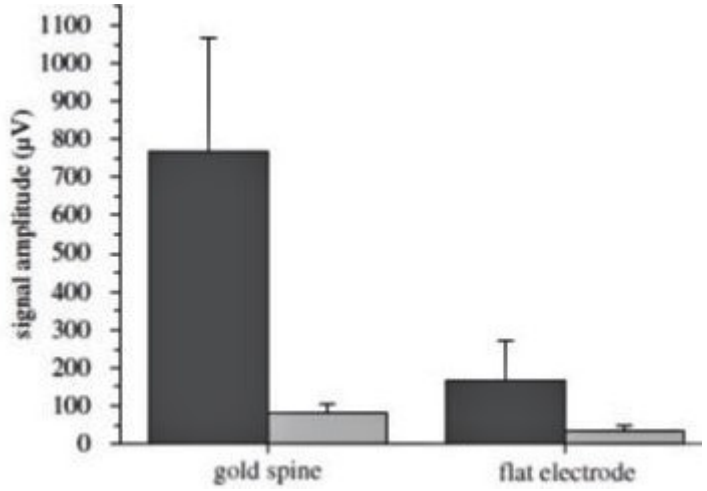

FIGURE 2.13: The comparison between MEA devices and gold mushrooms-shaped microelectrodes arrays (adapted from [13]).

In Fig. 2.13, the dark grey bars represent the amplitude of the recorded signal and the light grey bars represent the noise amplitude. Clearly, the amplitude signal is much larger when using gold mushroom-shaped microelectrodes than on flat electrodes, although the noise is also larger in the gold mushrooms-shaped microelectrodes [13]. This is a most recent and advantage technique, but how can we produce gold mushrooms-shaped microelectrodes arrays? For this, it is necessary to create an experimental procedure, where lithography and deposition techniques are present.

2.4.1 Fabrication of gMμEs

To fabricated gold mushroom-shaped microelectrodes it is necessary to use deposition and lithography techniques. Deposition, spin coating, exposure and development, electroplating and photoresist strip are the sequential steps needed to created these type of structures (Fig. 2.14).

Figure 2.14(b), corresponds to a deposition step, where a thin film is deposited. For the gMμEs produced in this thesis, gold (Au) was the material deposit on the substrate. Afterwards, the

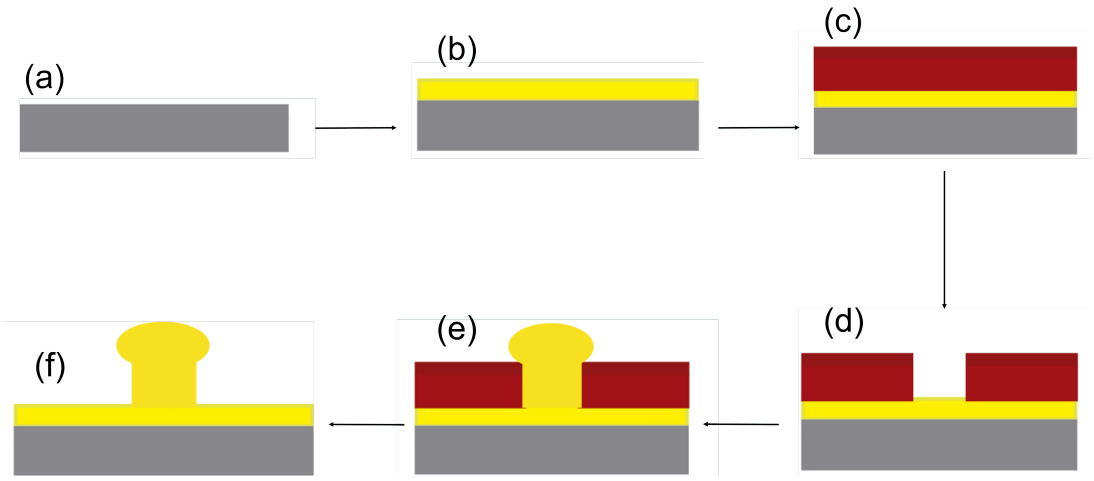

FIGURE 2.14: The sequential steps to produce the gMμEs: (a) silicon substrate; (b) gold thin film deposition; (c) spin coating of the photoresist; (d) exposure and development; (e) electrodeposition and (f) strip of the photoresist.

spin coating [Fig. 2.14(c)], exposure and development of the photoresist [Fig. 2.14(d)], are steps of the lithography process. The spin coating consist in depositing, through a spinner, a thin layer of a photosensitive polymer, named photoresist. Exposure is the step where the pattern is transferred to the photoresist. Electrodeposition [Fig. 2.14(e)] is a chemical method to deposit conductive materials on the substrate and can be used to fill structures. Finally, the last step is the strip of the photoresist [Fig. 2.14(f)] that consists in removing the photoresist thin layer with acetone. A more detail information about the experimental methods and the fabrication process can be found in the Chapter 3 and 4.

Figure 2.12(d) corresponds to a gold mushroom-shaped microelectrodes arrays. In this figure, we have a scanning electron microscope (SEM) image of a neuron engulfing the microelectrode and the signal recorded by the microelectrode. In the available literature, different values for the mushroom height and the stalk diameter have been reported. These values ranged between the micron and nano dimensions. Thus, for the stalk diameter, the sizes reported are comprised between 1 µm to 500 nm, but for the mushroom height the values reported comprise 1 to 2 µm [14][16][40].

Some studies have also been reported on the influence of the size and the distance between microelectrodes on neuron engulfing. In relation to the size, the cap diameter must be smaller than 2.5 μm because, beyond this diameter, although the neurons adhere to the surface of the mushroom caps, they fail to engulf them, decreasing the value of the coupling coefficient [14].

Other studies reported the possibility to direction cells growth. Cultured neurons usually grow in an unordered way. This growth causes a non-uniform distribution of cells in the substrate.

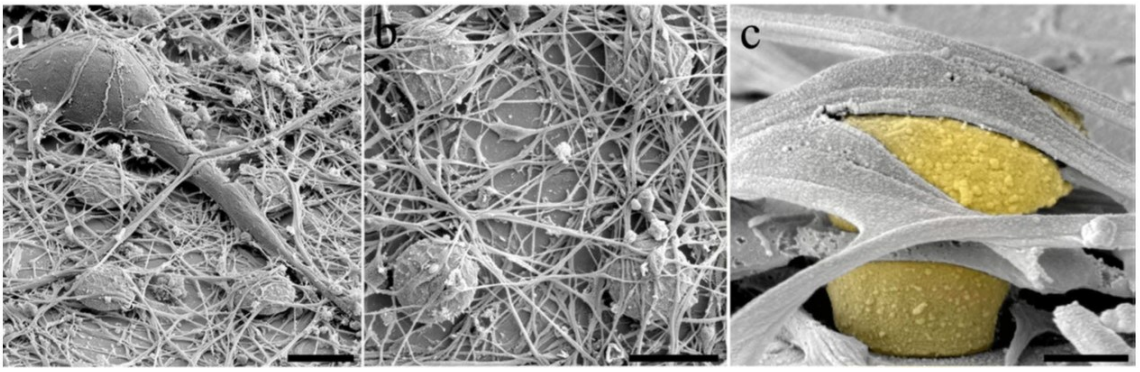

FIGURE 2.15: Scanning electron microscope images of neurons grown on a matrix of gMμEs: (a) a low magnification image of a neuron's cell and an extending neurite on a matrix of large gMμEs; (b) the neurites growing on top of the gMμEs and (c) the neurites on top of a mushroom cap appear to tightly adhere to the surface [14].

To create a well-defined network of cells on MEAs, it is necessary to guide the cells growth by the patterning. Guidance can be realized through different techniques (like protein patterning, grooves, etc) that have been develop in the last years [15]. In the case of protein patterning for neuron guidance, one uses a well-defined pattern and geometry where the protein is recognized by the cells and form a cell-matrix boundary. Figure 2.16(b) shows an example of a matrix designed to guide the growth of the neuron cells. When the cells are cultured in this type of sample, neurons grow ordered over the design pattern, as shown in Fig. 2.16.

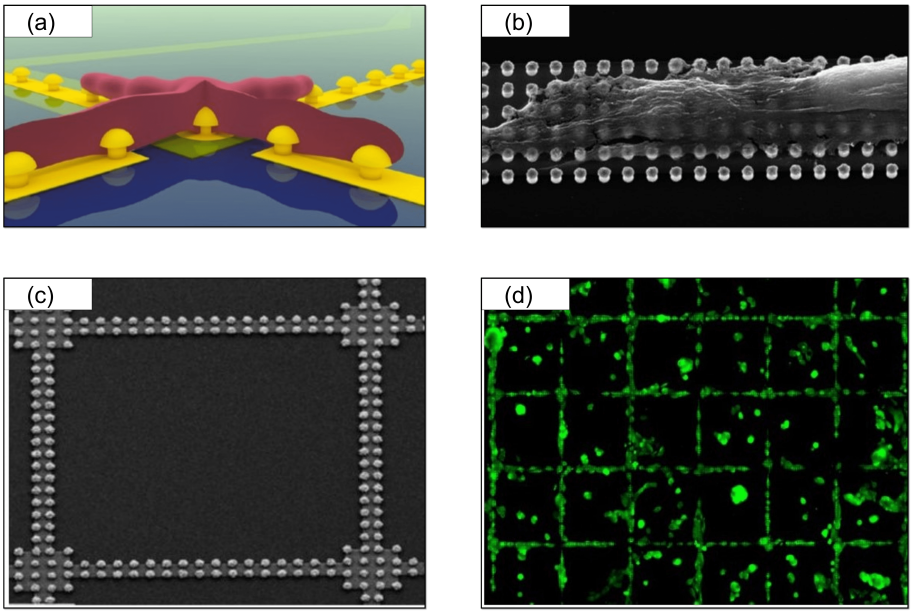

FIGURE 2.16: Silicon substrate with patterns of nano gold-mushroom arrays for neuron guidance: (a) schematic of a guided neuron by a pattern composed by gold-mushroom microelectrodes; (b) zoom-in view of the pattern; (c) SEM image of the neuron guided through the microelectrodes; (d) Confocal microscope image [15].

2.4.2 Engulfment mechanism

The formation of neuron hybrid interfaces has been highly studied in the last years. One of the major problems in creating neuron hybrid interfaces, is the low value of the coupling coefficient. In order to obtain high values of the coupling coefficient, it is necessary to have a good engulfment of the microelectrode. This leads to a high seal resistance value and to a reduced cleft between the neuron and the microelectrode, that allows increasing the value of the coupling coefficient [41]. The cleft appears when the neuron tries to adapt the cellular membrane to the shape of the microelectrode, allowing the communication between them. Figure 2.17 shows the engulfment mechanism, where it is possible to see the engulfment of the gold-mushroom microelectrode by a neuron cell.

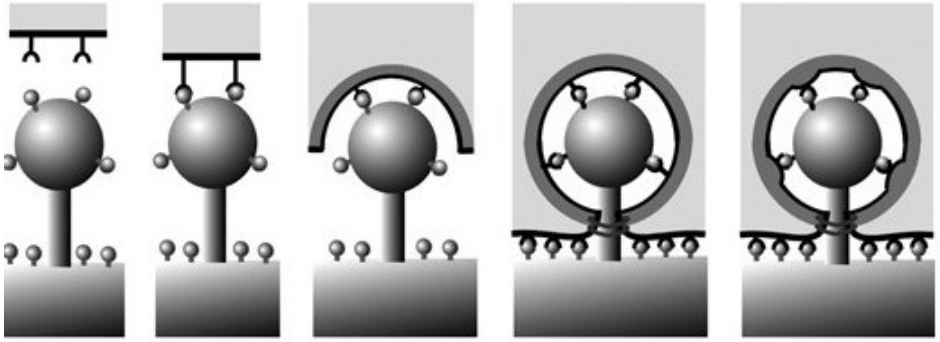

FIGURE 2.17: The engulfment of a gold microelectrode by a cell (adapted from [13]).

The engulfment of the gMμEs is based on the natural phenomenon of particle phagocytosis by living cells. This process creates extensions of the plasma membrane around a particle, in which the particle 'sinks' into the cell, leading to its internalization. The phagocytosis allows the internalization of large particles of the order of 0.5 µm [41][13]. Then, similar to the phagocytosed particle, the gold-mushroom microelectrode will be engulfed by the plasma membrane. The first step of the phagocytosis is the interaction between the receptor molecules present in the cell and molecules present on the surface of the microelectrode. Afterwards, the cellular membrane engaged receptors recruit a number of proteins that allow the plasma membrane to internalize the particle. Finally, the plasma membrane surrounds and tightens the particle. Nevertheless, the gold-mushroom microelectrode will be bloated by the cell, but the process of internalization will end when the plasma membrane tightly surrounds the head and the stalk of the microelectrode. Hai *et al.* found that cells cultured on gMμE arrays engulf the mushrooms and the field potentials generated by action potentials of cultured neurons are larger when neurons are cultured on gold-mushroom microelectrodes in comparison with records on

flat electrodes [13]. Conceptually, the mushroom shape represents a favorable shape for biological interfaces, considering that in neuronal cultures the dendritic spines are responsible for biomechanics stability and signal propagation between cell and the dendritic spines have a mushroom-shape. Then, neuronal cells can recognize the microelectrodes as a physiological structure and build a connection to it. The cells then grow around the gMμEs and promote the engulfment process.

2.4.3 Functionalization of the gMμEs

After the gold-mushroom microelectrodes arrays are made, it is usually necessary to functionalized them. Functionalization is a surface treatment to convert the surface from hydrophobic into hydrophilic. This surface treatment is necessary because hydrophobic surfaces prevent cell growth [42]. The surface treatment can be made in three different ways, denominated Plasma Cleaning, Protein Coating and Pre-culturing. Plasma Cleaning consists in placing the sample inside a plasma chamber under low vacuum for about two minutes. In this chamber, the surfaces are expose to a gas plasma discharge, that transforms the surface in a polar and therefore hydrophilic surface. The problem of this technique is that the treatment of the surface disappears after a few days. Protein Coating is a treatment where the surface is sterilized and then the region of the culture is placed in a concentrated protein solution for a given time (usually 30 minutes). After this, the sample is washed with water. This technique is the most simple and quick form to obtain a hydrophilic surface. Finally, we can coat the surface with one culture of cells and leave the cells grow for a long period (several days), until the cells transform the surface into hydrophilic. This method is denominated by Pre-culturing and is the method with the most objections because the pre-culture has small growth and viability, and it is necessary to remove this culture before placing the culture of the experiments [43][44]. After the sample is functionalized, it is placed in a neuron culture that adheres to the surface of the gold-mushrooms, doing their engulfment. The neuron cell can grow in the form of a network with preferential direction created by the fabricated microelectrodes. After the engulfment, we can measure the action potentials and record them using an electronic circuit.

2.4.4 Recorded Signal

The MEA device constituted by the gMμEs has been proved a good interface to record the neuronal signal, because the recorded signals are comparable in amplitude to signals recorded by intracellular techniques (in the range of μV). Figure 2.18 shows the experimental set-up used to measure and compare the signal recorded by gMμEs and an intracellular technique.

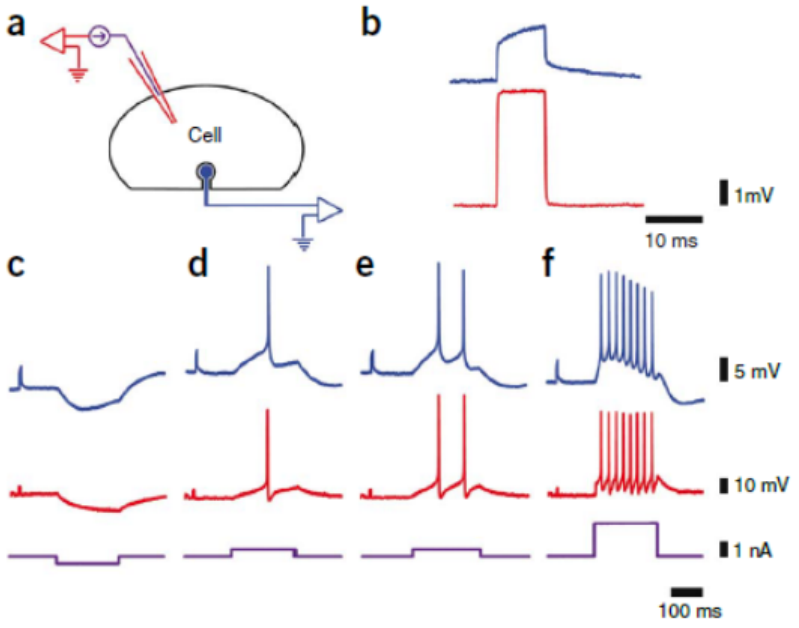

FIGURE 2.18: Recorded Signal by gMμEs in the "in-cell" configuration. (a) Schematic of the experimental set up; (b) calibration pulses applied to the cultured cells recorded by intracellular and gold-mushroom electrodes; (c) hyperpolarization pulses applied to the neuron and recorded by intracellular and the gold-mushroom electrodes; (d),(e) and (f) depolarization pulses and signal recorded by the two electrodes. The red line corresponds to records by the intracellular electrode; the blue line represents the results for the gMμEs, while the purple line corresponds to the injected current [16].

The intracellular method represented in Fig. 2.18 is the patch clamp technique. The patch clamp penetrates the neuron allowing to inject a current and measure the intracellular voltage. The injected current is plotted as the purple line in Fig. 2.18, while the red line is the patch pipette signal. The gold-mushroom microelectrode was placed at the extracellular side for voltage measurements and is represented by the blue line. From Fig. 2.18 one can see that, increasing the injected current [Figs. 2.18 (d) - (f)] leads to the depolarization of the cell, while the signal was again measured intracellularly and extracellularly by the electrodes. The shape and amplitude of both records are very similar. gMμEs are thus a suitable method to record neuronal signals in an extracellular manner [16].

2.4.5 Cell-microelectrode electrical interface

When the neurons are grown on the substrate it is possible to represent the interface between a neuron and gMμEs (3D microelectrode) as an analog electrical equivalent circuit. Figure 2.19 shows two situation of the engulfment and the respective equivalent circuit.

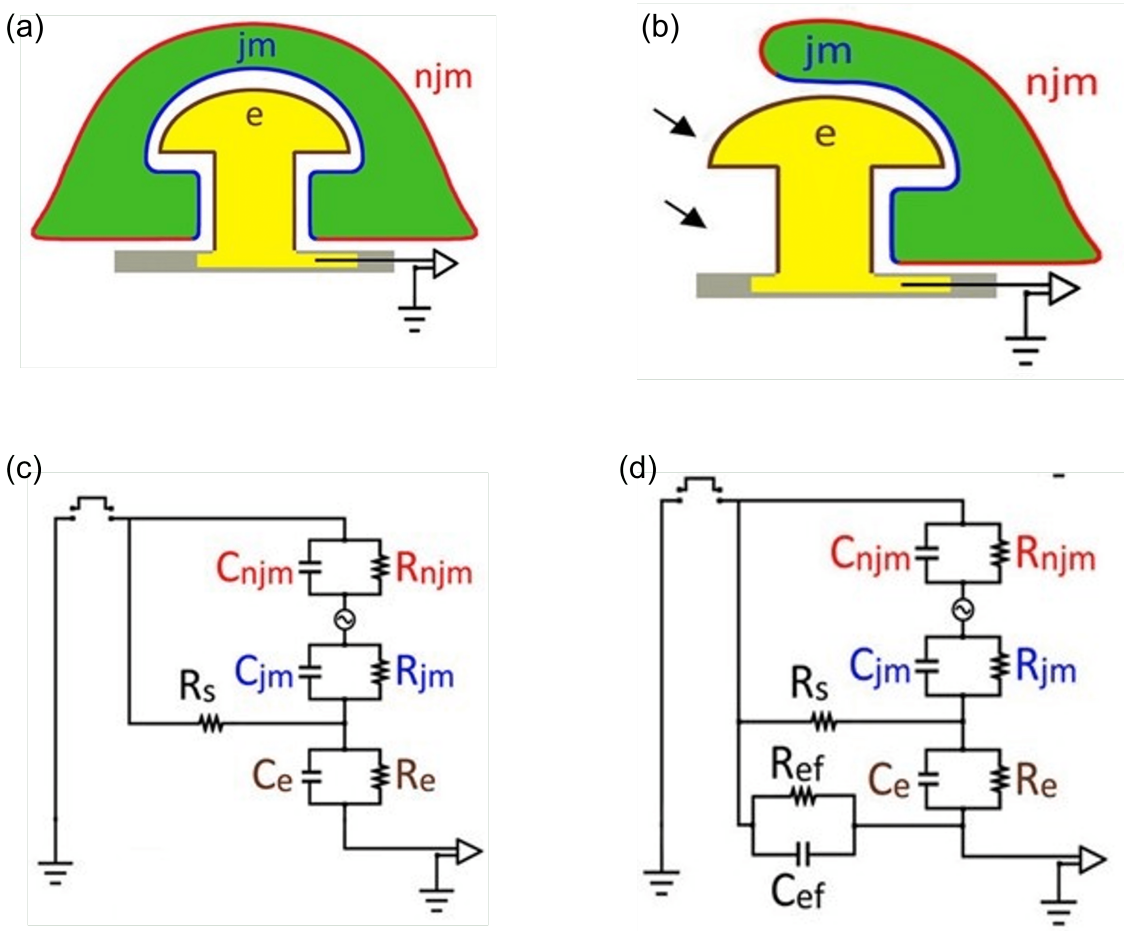

FIGURE 2.19: Electrical model of the interface between the neuron cell and the gold mushroom-shaped microelectrode: (a) schematic of the interface, where the neuron cell realizes the total engulfment; (b) schematic of the interface, where the neuron fails the engulfment; (c) equivalent electrical circuit of the total engulfment; (d) equivalent electrical circuit of the partial engulfment (adapted from [14][17]).

The coupling coefficient value varies as a function of the engulfment and the biophysical parameters. Through simulations we can estimated the value of the coupling coefficient depending on the value of the junctional domain facing the microelectrode, defined by a resistance R_j and a capacitance C_j. The domain of the cell membrane which faces the bath is the non-junctional membrane. This domain is characterized by a resistance R_{nj} and a capacitance C_{nj}. The gold-mushroom microelectrode has an impedance that is represented by a resistor R_e and a capacitor C_e. The cleft formed in the engulfment process is characterized by the spreading resistance $R_{spreading}$. Hai *et al.*, performed simulations to obtain the coupling coefficient as a function of the seal resistance at different values of the junctional membrane resistance and different frequencies [18].

The coupling coefficients were calculated for stimulus in a frequency range from 100 Hz up

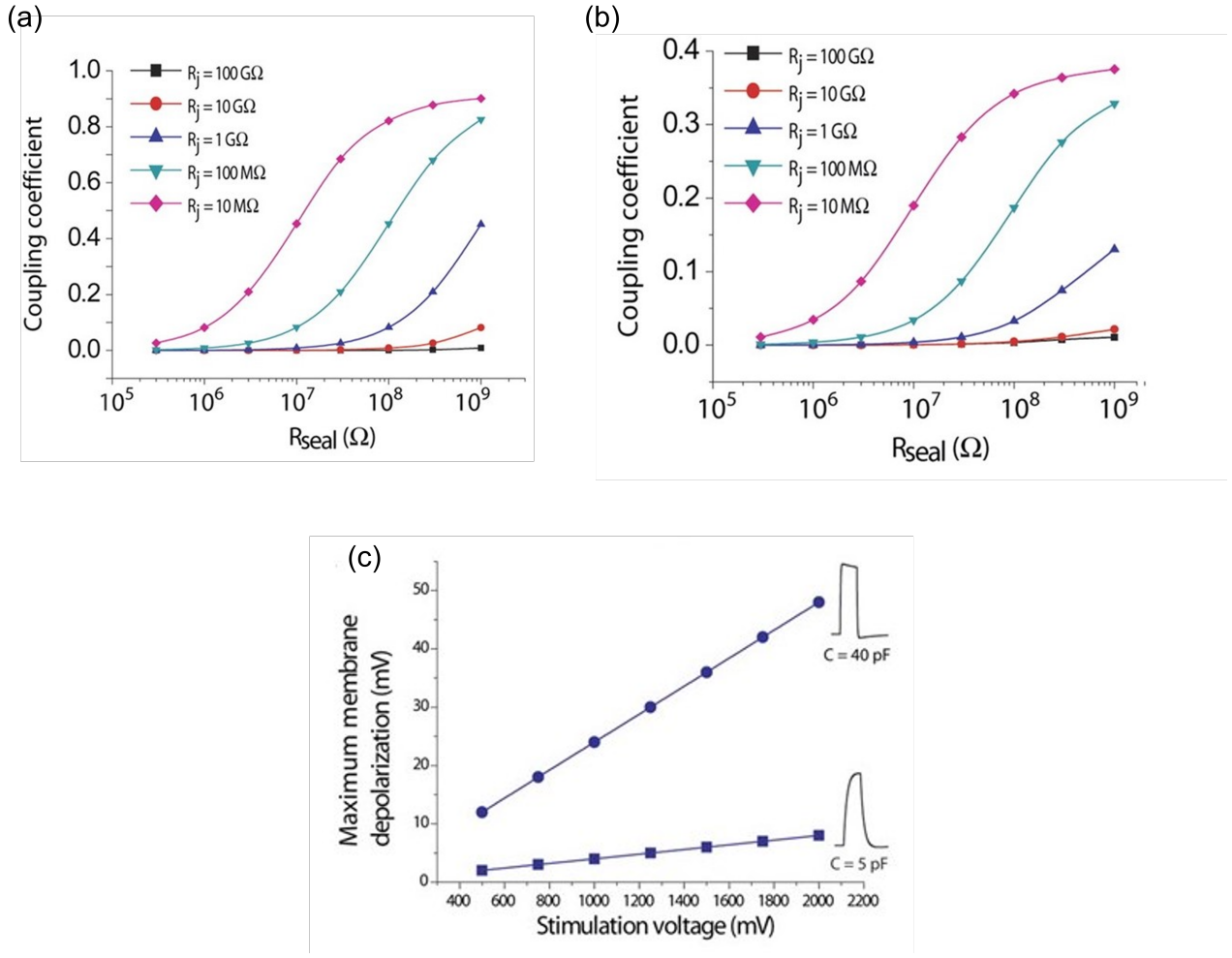

FIGURE 2.20: Simulation of the electrical properties of the interface between a neuron cell and a gMμE: (a) coupling coefficient as a function of the seal resistance for high and (b) low frequencies; (c) maximum membrane depolarization as a function of the stimulation voltage via gMμE for high (dot points) and low (square points) frequencies (adapted from [18]).

to 1 kHz. Assuming that the seal resistance is approximately 100 MΩ and that the junctional membrane ranges from 10 MΩ to 100 MΩ, the coupling coefficient was calculated and plotted (Fig. 2.20). It was shown that the coupling coefficient value varies from 0.05 up to 0.4 for low frequencies ($\sim$ Hz) and from 0.05 up to 0.8 for high frequencies ($\sim$ kHz). Moreover, the maximum membrane depolarization was calculated as a function of the stimulation voltage [Fig. 2.20 (c)] for high frequencies (dot points) and low frequencies (square points) [18].

2.4.6 Biophysical parameters

The junctional membrane resistance (R_j) can be estimated, but first it is necessary to estimate the engulfed surface area of the gold-mushroom microelectrodes. For this, it is necessary to

model the gold-mushroom microelectrodes. We assume that the microelectrode has a cylinder shaped stalk and the mushroom cap's is a semi-hemisphere [45]. The engulfed area of the gMμE is given by [45]:

$$A_{goldmushroom} = A_{stalk} + A_{cap} + A_{rim}, \tag{2.4}$$

where A_{rim} is the surface area under the mushroom and the others areas are given by [45]:

$$A_{stalk} = 2 \times \pi \times r_{stalk} \times h_{stalk}, \tag{2.5}$$

$$A_{cap} = 2 \times \pi \times (r_{cap})^2, \tag{2.6}$$

$$A_{rim} = \pi[(r_{cap})^2 - (r_{stalk})^2], \tag{2.7}$$

where A_{stalk} is the stalk area and A_{cap} is the cap area. The value of r_{stalk} and r_{cap} corresponds to the radius of the stalk and cap, respectively, and h_{stalk} is the height of the salk.

After estimating the engulfed area, it is necessary to calculate the neuron surface area. This value is calculated using the area membrane capacitance. To estimate the value of the junctional membrane resistance, one multipies the value of the input resistance by the ratio between the surface area of the neuron (A_{neuron}) and the surface area of the engulfment ($A_{goldmushroom}$). The junctional membrane resistance is then estimated according to [45]:

$$R_j = R_{in} \frac{A_{neuron}}{A_{goldmushroom}}. \tag{2.8}$$

The junctional capacitance, C_j, can also be estimated by the engulfed area ($A_{goldmushroom}$) and the specific membrane capacitance (C_{jm}). Thus, the junctional membrane capacitance, is given by [45]:

$$C_j = \frac{C_{jm}}{A_{goldmushroom}}. \tag{2.9}$$

The resistance of the gold-mushroom microelectrode arrays can be estimated, in a solution, using the results reported in Hai *et al* [16], that measured for, a mushroom surface with 14 µm^2 of area, a resistance of 1 GΩ. To calculate the capacitance of the gold-mushroom microelectrodes

arrays we use the specific capacitance of the gold electrical double layer ($_{EDL}$). This value is approximated 50 µF/cm^2. Thus, the gold-mushroom microelectrodes arrays capacitance is given by [45]:

$$C_{goldmushroom} = C_{EDL} \times A_{goldmushroom}. \tag{2.10}$$

Another important parameter is the spreading resistance. The spreading resistance is generated by the gap between the surface of the gold-mushroom microelectrode arrays and the engulfing cell membrane. This resistance is composed by three resistors in series: (a) the resistor between the cap surface and the cell membrane (R_1); (b) the resistor of the cap bottom (R_{rim}) and (c) the resistor of the stalk (R_{stalk}).

The resistor between the cap surface and the cell membrane, can be calculated by [45]:

$$R_1 = \frac{\rho}{2\pi t}\{ln[tg(\frac{\pi}{4})] - ln[tg(\frac{\alpha}{2})]\}, \tag{2.11}$$

where ρ is the solution resistivity, *t* is the cleft thickness and α the cap capacitance. To obtain the value of α, it is necessary to equal the Eqs. (2.12) and (2.13). These areas follow the relations [45]:

$$A_1 = 2\pi(r_{head})^2(1 - cos(\alpha)), \tag{2.12}$$

$$A_2 = 2\pi(r_{head})^2 cos(\alpha) + 2\pi[(r_{head})^2 - (r_{stalk})^2] + 2\pi r_{stalk} h_{stalk}. \tag{2.13}$$

After obtaining α, we insert it in Eq. 2.11, and obtain the value of R_1. The second contribution to the spreading resistance is the resistor of the cap bottom, that can be estimated according to [45]:

$$R_{Rim} = (\frac{\rho}{2\pi t})ln(\frac{r_{head}}{r_{stalk}}). \tag{2.14}$$

The last contribution is the resistor of the stalk, that is given by [45]:

$$R_{stalk} = \frac{\rho h_{stalk}}{2\pi t r_{stalk}}. \tag{2.15}$$

The spreading resistance is then the sum of these three contribution [45]:

$$R_{spreading} = R_1 + R_{Rim} + R_{stalk}. \tag{2.16}$$

Chapter 3

Experimental Methods

In this chapter we will give a brief description of the fabrication and characterization methods used in this thesis. To deposit materials we used both physical and chemical techniques, comprising Magnetron Sputtering and Electrochemical Deposition (electrodeposition). For the analysis of the stoichiometry of the produced materials, Energy Dispersive X-ray Spectroscopy (EDS) was employed. The morphology was studied with Scanning Electron Microscopy (SEM). Finally, for the fabrication of the micro gold-mushrooms, lithographic techniques were employed.

3.1 Deposition Techniques

Physical Vapor Deposition (PVD) is an atomistic process in which a material is vaporized from a target (solid or liquid) in atomic or molecule form, and is deposited on a substrate. These processes need low vacuum and are usually used to deposit thin films with a few nanometers to thousands of nanometers of thickness [46].

3.1.1 Magnetron sputtering

Sputtering deposition is a PVD process [46] in which the material to be deposited is physically evaporated through the bombardment of ions, from an inert gas, like Argon, that is ionized and accelerated in the direction of the target. After evaporated, the material is transported to the substrate where it condenses. There are several configurations for a sputtering system. In this work, we used Magnetron Sputtering [47], that is currently applied in several areas, like wear-resistant coatings, low friction coatings, corrosion-resistant coatings, decorative coatings

and coatings with specific optical properties. Beside that, this type of sputtering is a versatile technique for the deposition of high-quality and well-adhered thin films [47]. In this case, the target material serves as the cathode, that is bombarded by ions generated in a discharge plasma in front the target. This bombardment causes the removal of material from the target that condensates in the substrate. Secondary electrons emerge from the ionic bombardment and these electrons are important to maintain the plasma. The presence of a magnetic field causes the confinement of the secondary electrons near the target, that allows increasing the intensity of the bombardment [19][46][47]. Figure 3.1 is a schematic of a Magnetron sputtering system.

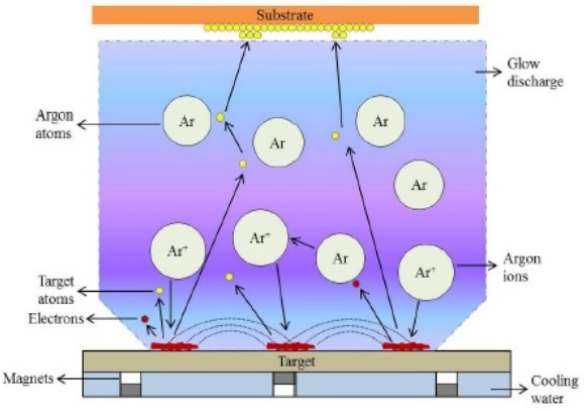

FIGURE 3.1: Schematics of a Magnetron Sputtering system (adapted from [19]).

This configuration is simple and adequate to deposit conductive materials. Here, this deposition process was used to deposit thin Cr and Au layers. These depositions were performed at the Iberian Nanotechnology Laboratory (INL) in a Kenosystek system [Fig.3.2(b)] and at INESC-MN in an Alcatell tool [Fig.3.2(a)].

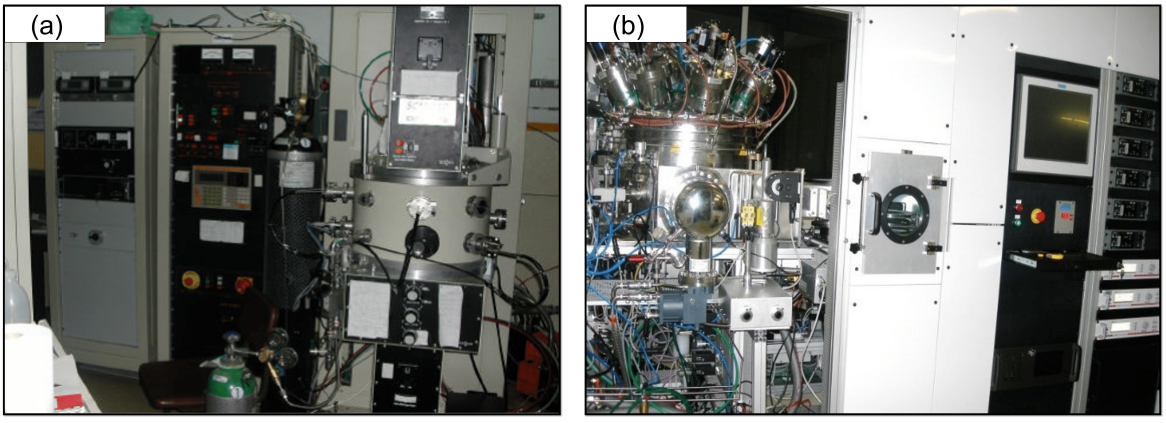

FIGURE 3.2: The image of Magnetron Sputtering system used in this work: (a) INESC-MN and (b) INL.

3.1.2 Electrodeposition

Electrochemical deposition or Electrodeposition is a chemical process able to produce thin films or grow structures in conductive substrates. Electrodeposition can be operated in continuous or pulsed methods. The Pulsed method, denominated by pulsed electroplating or pulsed electrodeposition, involves the cyclical variation of the potential or current between two values that leads to a series of pulses. By changing the electrodeposition parameters, it is possible to modify the composition and the thickness of the deposited film [48]. The continuous method, called DC electrodeposition, uses a continuous electrical current (galvanostatic electrodeposition) or a continuous potential difference (potentiostatic electrodeposition) to reduce the metallic ions present in the electrolyte solution. The electrolyte is a solution where the metal of interest to deposit is dissolved into a solvent.

Electrodeposition set-ups are composed by three electrodes (a reference electrode, a counter electrode and a working electrode), by a power supply and a cell (Fig. 3.3). To reduce the material, an electrical current is applied by the power supply between the counter and working electrodes, while the cations of the desired material are reduced at the cathode.

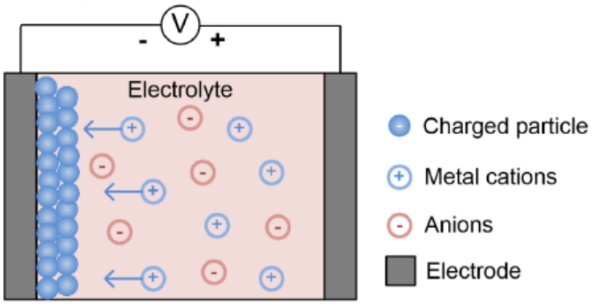

FIGURE 3.3: The flux of ions in the electrodeposition process [20].

For the reduction to occur, it is necessary that the applied potential (in the case of potentiostatic electrodepositon) between the counter and working electrodes, to be equal or near to the standard value of the reaction. In fact, each reaction has a standard value, that is tabled in relation to the reference electrode. In the majoring of cases, the tabled values are calculated in relation to the standard hydrogen electrode (reference electrode; Fig. 3.4). It is then necessary to adjust these values to the standard electrode used in the experimental set up [49][50].

When the reduction occurs, the electrons cross the interface between the electrode and the solution. The number of electrons that cross the interface is linked stoichiometrically to the extent of the chemical reaction. The number of electrons that passes in the circuit gives the

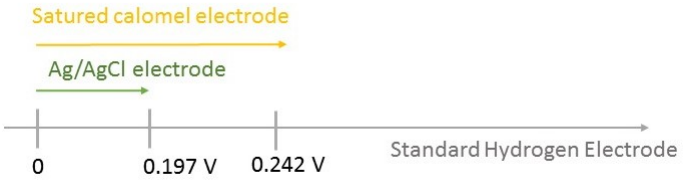

FIGURE 3.4: Hydrogen electrode versus Ag/AgCl and SCE standard electrodes.

total charge (*Q*). Assuming an electrodeposition efficiency of 100%, this allows us to calculate the deposited mass of the metal:

$$m = \frac{Q}{F}\frac{M}{z}, \tag{3.1}$$

where *Q* is the total electrical charge that flowed though the circuit, *F* is the Faraday constant, *M* is the molar mass of the substance and *z* is the valency number of ions (electrons transferred per ion) [48]. Other quantities, like the deposited thickness or the time needed to deposit a desired thickness can be evaluated. The deposit thickness is given by:

$$d = \frac{m}{ad}, \tag{3.2}$$

where *m* is the deposited mass of the metal, *a* is the plated surface area and *d* is the density of the deposited material. When the height of the structure, or the thickness of a thin film is known, the time (t) needed to deposit at a given current density is related to:

$$t = \frac{hadzF}{mi}, \tag{3.3}$$

where *h* is the desired height. From this equation we conclude that, if the current intensity increases, the time need to deposit decrease. Using the deposited material and the time of the deposition, we can calculated the deposition rate of the process. This value is characteristic of each solution used to deposit the desire material. The overpotentital (η) is given by the difference between the potential electrode when current flows through it and the potential electrode in the absence of current. This value is related to the efficiency of the cell. Current density is related with the overpotential by the Tafel equation:

$$i = -FkCexp(\frac{\alpha F\eta}{RT}), \tag{3.4}$$

where *k* is a constant, *C* is the concentration of metal ions in the solution, α is the coefficient of symmetry, *R* is the ideal gas constant and *T* is the absolute temperature in Kelvin [20]. Equation (3.4) shows that small variations in η produce large changes in the current density. Thus, to have good electrodeposition,the cell potential need be controlled [48][49].

A three electrode cell configuration was used in this work. Gold depositions were performed in a beaker, using an Ag/AgCl reference electrode, a platinum mesh as the counter-electrode and a conductive substrate as working electrode (Fig. 3.5). The used electrolyte solution, Orosene E +4gr/lt, consisted in a conductive gold bath and its properties can be founded in the data sheet distributed by the manufacturers [51].

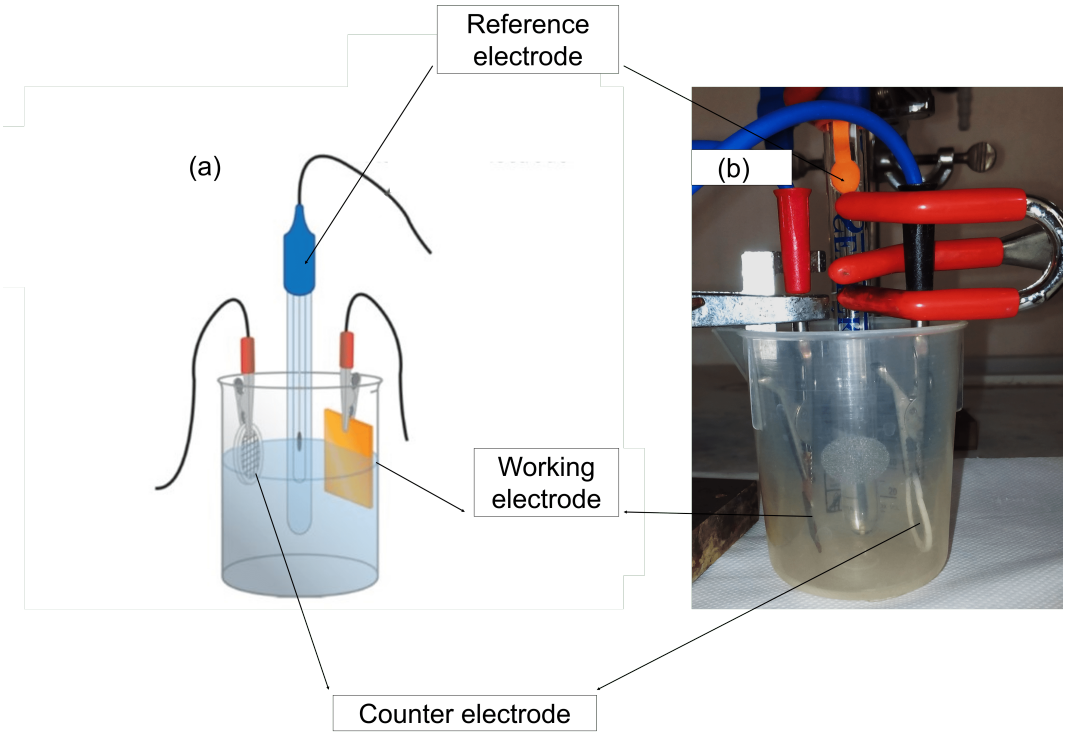

FIGURE 3.5: Three-electrode configuration used for potentiostatic electrodeposition. In (a) have the schematic of the technique and (b) the photo of the electrodeposition set-up (adapted from [21]).

All gold electrodepositions were performed using the potentiostatic method. When the constant voltage difference is applied, the substrate surface is polarised and the complex ions present in the electrolyte solution are attracted. Thus, when the $[Au(CN)_2]^-$ (present in the gold cyanide bath) approach the reduction interface, this anion receives one electron and the metallic ion is reduced, feeding the Cyanide anion. The chemical reduction reaction responsible for the production of metallic gold, using the Orosene solution, is:

$$[Au(CN)_2]^{-1} + e^- \longrightarrow Au + 2CN^{-1}. \tag{3.5}$$

The gold reduction potential is -0.61 V, with respect to the hydrogen standard electrode [52][53]. With respect to the Ag/AgCl standard electrode, the reduction potential is approximated -0.8 V. When the electrodeposition starts, several reactions occur simultaneously. This creates a difference between the tabled and experimental reduction potential values. Normally, the experimental reduction potential values are larger (in magnitude) than the tabled ones.

3.2 Characterization Techniques

3.2.1 Scanning Electron Microscopy (SEM)

Scanning Electron Microscopy is an electron microscope technique that allows inspecting the morphology of samples due to the elastic and inelastic collisions between an electron beam and the sample. A SEM system consists of an electron gun, an electromagnetic optical system and a set of different detectors. In this type of microscopy, the surface of the sample is irradiated with a beam of high energy electrons focused by a set of magnetic lenses. The magnetic lenses are responsible for moving the focused beam back and forth in the sample. The interaction between the electron beam and the surface of the sample leads to the emission of Secondary Electrons (SE), Backscattered Electrons (BE) and X-rays that are used to form the image. Secondary electrons give topographic information and are the result of inelastic collisions caused by the incident beam. These electrons are the first to be scattered and have energies smaller than 50 eV. Backscattered Electrons are the electrons from the primary beam that experience an elastic collision with the sample's electrons. The number of BE collected is related with the chemical composition of the sample and these electrons are the second to be scattered by the sample. Thus, these electrons produce an image with the distribution of chemical elements. The secondary and the backscattered electrons can be distinguished through their kinetic energy. The SEM resolution is related with the beam spot size and the interaction volume, and can go down to nm. The main limitation of this technique is charge accumulation in non-conductive samples. In this case, an electrically conductive coating must be applied to the samples under study, unless the instrument is capable of operation in a low vacuum mode.

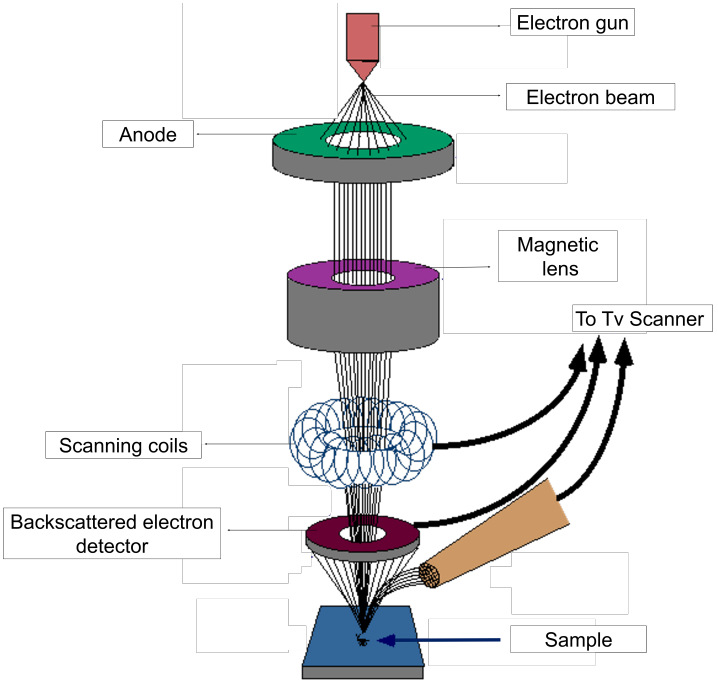

FIGURE 3.6: Scanning Electron Microscopy (SEM) (adapted from [22]).

3.2.1.1 Energy Dispersive X-ray Spectroscopy (EDS)

Energy Dispersive X-ray Spectroscopy (EDS) is a technique that is often incorporated in SEM systems. As in SEM, the sample area is scanned to analyse the chemical elements present. The interaction between the electron beam and the sample results in the emission of X-rays. The emitted X-ray spectrum provides information on the chemical elements that are present in the sample. This technique allows the qualitative and quantitative analysis of the scanned area.

Both SEM and EDS experiments in this thesis were performed at CEMUP (Portugal) and Escuela Técnica Superior de Ingenieros de Telecomunicación (Polytechnic University of Madrid; Spain).

3.2.2 Profilometry

A profilometer is an instrument that allows measuring the roughness and the film thickness of a sample, indicating the profile of its surface. All profilometer measurements were performed with a Bruker $DektakXT^{TM}$ (Fg.3.7), in the CEMUP - MNTEC clean-room. The $DektakXT^{TM}$, is a powerful instrument that allows measurements down to 10 nm of thickness. This tool is a contact profilometer, where a diamond cantilever scans the sample surface, measuring its profile. Technical details on the $DektakXT^{TM}$ can be found in the respective user's manual.

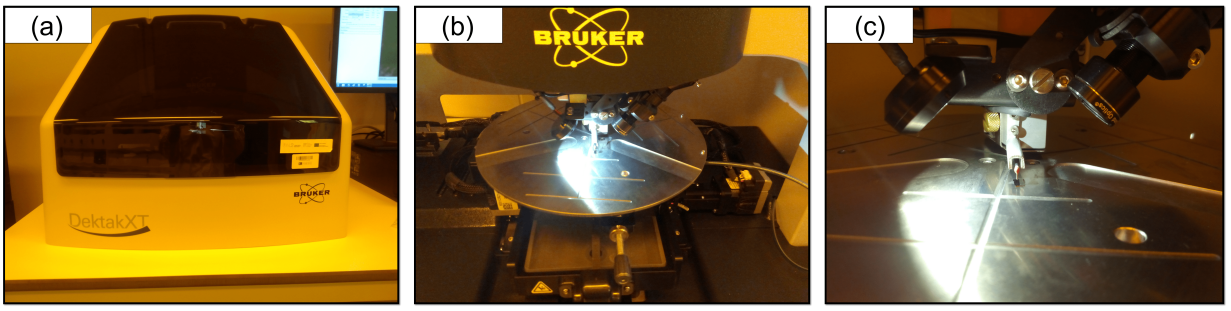

FIGURE 3.7: $DektakXT^{TM}$ profilometer: (a) set-up; (b) support of the sample and (c) cantilever and camera.

3.2.3 X-Ray Diffraction (XRD)

X-Ray Diffraction is a technique used to study the crystalline structures and atomic spacing of materials. One needs to use radiation with X-ray wavelength because the atomic spacings are of the order of Angstrom. The incident beam is directed towards the sample surface, interacting with the electrons of the sample that produces the scattering of the incident beam. When the inter-atomic spacing is of the same order as the wavelength of the incident radiation, diffraction occurs, Fig. 3.8(a). Thus, the interaction between the incident beam with the sample produces an interference pattern. Constructive interference occurs when the Bragg's law is satisfied:

$$n\lambda = 2d_{hkl}\sin(\theta), \tag{3.6}$$

where *n* is an integer, λ the wavelength of the incident wave, d_{hkl} the distance between planes with the Miller indexes (hkl) and θ the angle between the atomic plane and the incident beam. The diffracted X-rays are then detected and counted [Fig. 3.8(b)]. Through a θ - 2θ scan, it is possible to obtain all diffraction directions of the lattice and identify the material because each material has an unique d-space. For the identification of the experimental pattern one should then compared it with a reference pattern [54].

XRD also allows estimating the grain size, over the broadening of the diffraction peak, according to:

$$\tau = \frac{K\lambda}{\triangle 2\theta\cos\theta}, \tag{3.7}$$

where τ is the size of crystalline domains, $\triangle 2\theta$ is the broadening of the peak at half maximum intensity and K is a shape factor.

X-Ray Diffraction experiments in this work were performed at IFIMUP-IN.

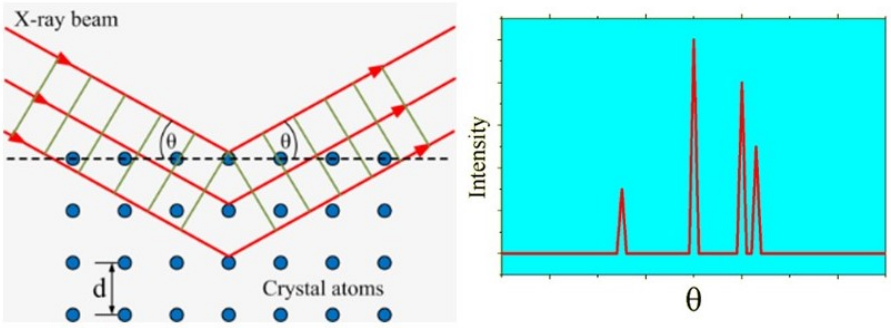

FIGURE 3.8: The XRD diffraction:(a) are the schematic of incident and diffracted beam and (b) are the diffraction pattern obtained.

3.2.4 Four-terminal sensing

Four-terminal sensing is a technique used to measure the electrical impedance and resistivity of a material.

3.2.4.1 Electrical Resistivity

Electrical resistivity (ρ; in $\Omega\,\mathrm{m}$) is an intrinsic physical property of a material independent of shape and size, that evaluates how much a material opposes the flow of an electric current through it. A low resistivity value demonstrates that the electric current flows easily through the material. Resistivity and conductivity are related according to:

$$\rho = \frac{1}{\sigma}, \tag{3.8}$$

where σ is the conductivity of the material [55].

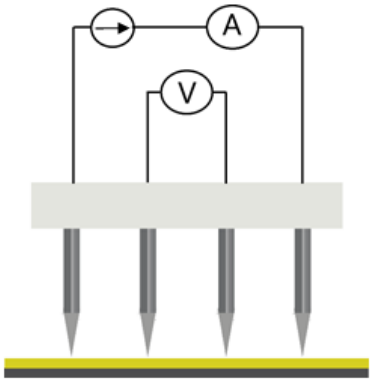

FIGURE 3.9: Four-point measurement of the resistivity.

Figure 3.9 demonstrates the four contact technique that takes advantage of current and voltage pairs to obtain accurate results. Through this method it is possible to eliminate the error caused by the contact resistance. The four contact method is constituted by four metallic probes that enter in electrical contact with the sample. The two external probes apply the current (I) to the sample and the two internal probes are used to acquire the voltage (V) drop across the sample. The resistivity measured through the four contact method is calculated according to:

$$\rho = \frac{A}{l}\frac{V}{I}, \tag{3.9}$$

where *A* is a area of the sample and *l* is the distance between voltage probes [55][56]. This method was employed to measure the resistivity of the gold thin film deposited into a silicon substrate at IFIMUP-IN.

3.2.4.2 Electrical Impedance

Impedance (Z; $\Omega\,\mathrm{m}$) is the total opposition to an alternating current by an electronic circuit. Impedance is a complex quantity where the real part correspond to a resistance (R) and the imaginary parte correspond to a reactance (X) that includes the capacitive or inductive parts.

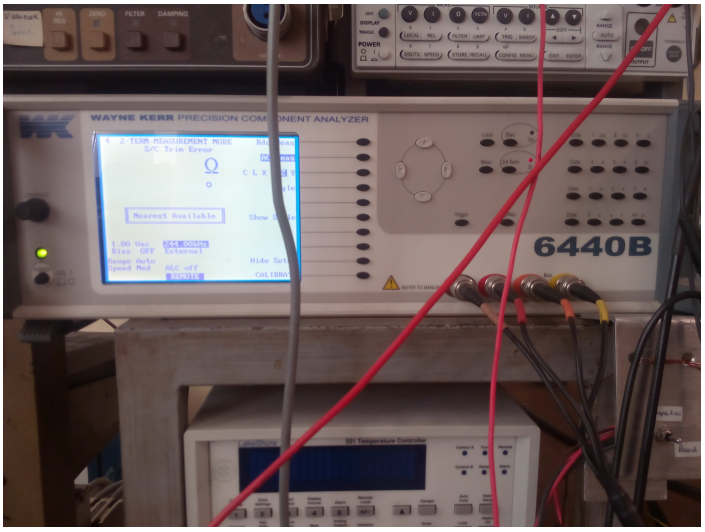

FIGURE 3.10: The impedance analyser.

In this work, we used a Precision Component Analyzer 6440B (Fig. 3.10), from Wayne Kerr Electronics, to measure the impedance of gold-mushroom microelectrodes arrays at IFIMUP-IN. This equipment uses four-terminal connections to measure with more accuracy the impedance and reduce the effect of contact resistance at the sample. Through a LabView routine, an alternating current at a given frequency is applied to the sample over the two external contacts and

the voltage is acquired through the two internal contacts. The LabView routine returns the data file.

3.3 Lithography

To print a 2-dimensional pattern in a substrate one must use a lithographic process. Direct Laser Write, electron beam, X-ray or optical lithographies are examples of Lithography tools. Lithography has a large range of applications, including advanced electronic technologies, biological interfaces, nano/micro devices. Advanced lithographic processes, like electron beam, have demonstrated resolution below 10 nm [57].

This process consists in transferring the pattern on a mask to the polymer placed in the substrate named Photoresist. After the pattern is transferred, it is possible to perform a large number of process such as lift-off, chemical etching, deposition or other techniques. Lithography is an easy but long process as it includes several steps (Fig. 3.11). The connection between Lithography and Deposition is called Patterning [57].

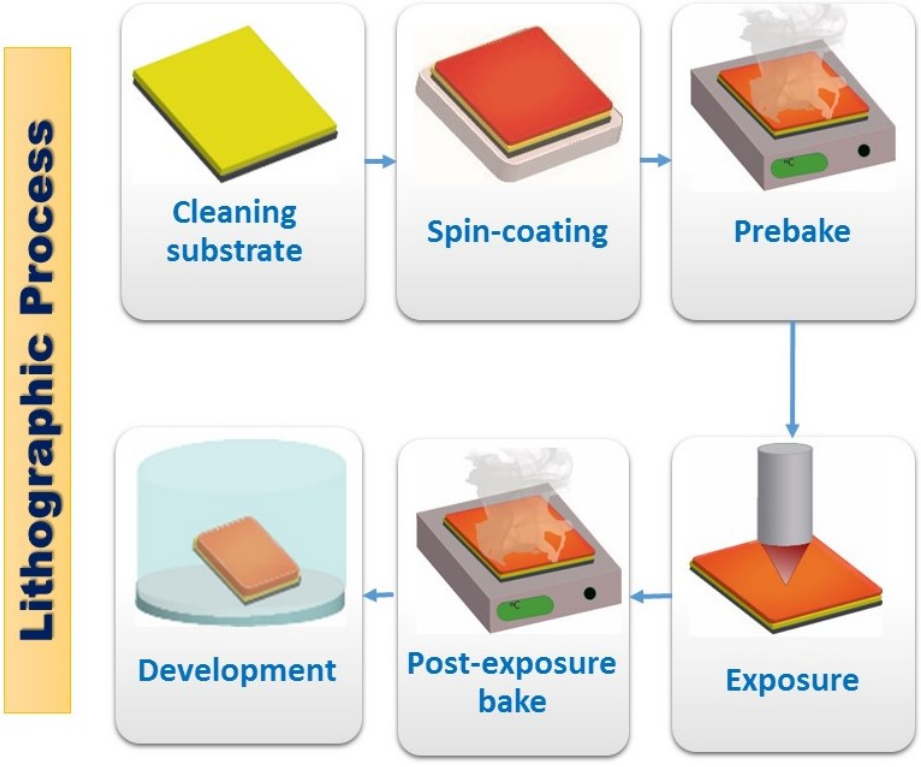

FIGURE 3.11: Lithography process.

Substrates, lithographic exposures parameters and the photosensitive coating of the substrates have to be carefully chosen according to the final application. The lithographic processes here presented were performed in the clean room of CEMUP-MNTEC (Porto) and INESC-MN (Lisbon).

3.3.1 Photoresist

Photoresist is a polymer that changes its properties when illuminated with light. A photoresist is composed by three essential elements: a solvent, a resin and a photoactive compound (PAC) or "sensitizer". The photoactive compound is the responsible for the permanent chemical changes in the solubility of the photoresist when lighted [58].

Photoresists can be classified as positive or negative. Positive photoresists are polymers that, when illuminated with ultra-violet (UV) light, become soluble. Thus, when the sample is developed, the illuminated regions are remove. One the other hand, when negative photoresists are illuminated, they become insoluble, so that in the development step the exposed region are not remove. Figure 3.12 shows pattern transferred using positive and negative photoresists.

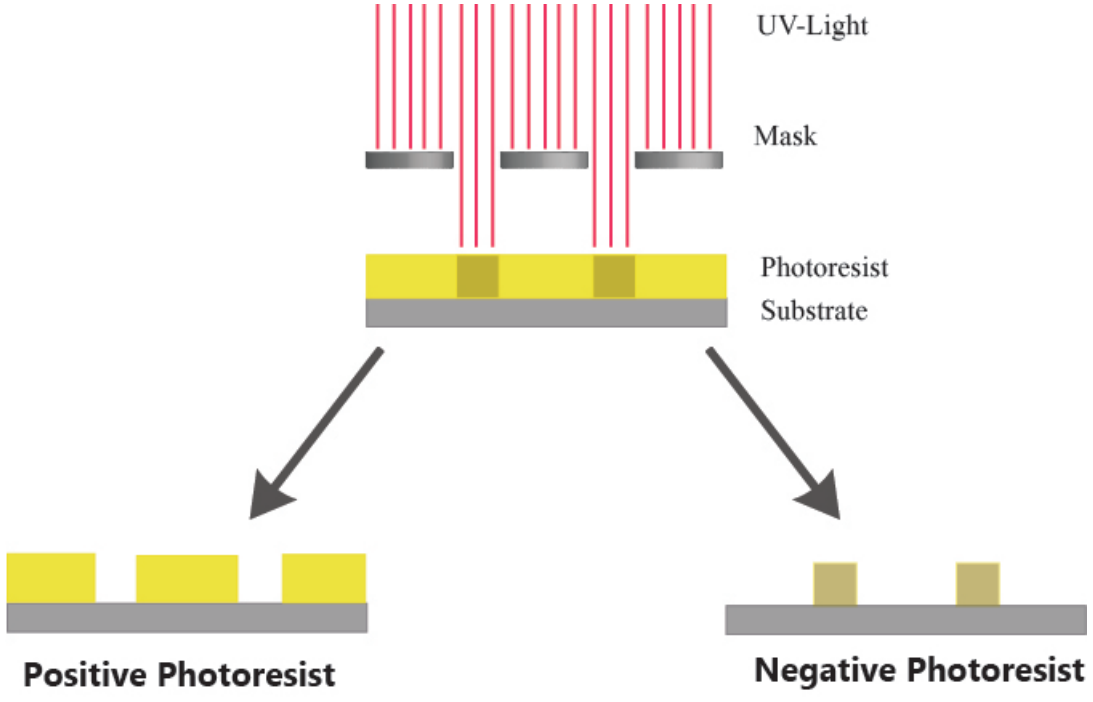

FIGURE 3.12: Pattern produced by Positive and Negative Photoresist after expose to the UV-light.

The chemical and mechanical properties of the photoresist are very important in the lithographic process, as they define the thickness and the necessary energy dosage to expose the pattern.

In this work, positive photoresists of the $S1800$ and $PFR7790G27cP$ series were used. Their properties can be founded in the data sheet distributed by the manufacturers [59].

3.3.2 Lithographic Process

A lithographic process starts with the preparation of the substrate, during which the substrate is cleaned and its surface modified to promote the adhesion of the photoresist to the substrate. Afterwards, the substrate moves to the spin coating process.

3.3.2.1 Spin coating

Spin coating, is a technique that uses a spinner to spread the photoresist in the surface of our samples. Figure 3.13 shows all the steps needed to coat a sample. After choosing the photoresist, the substrate is placed in a spinner and fixed by vacuum. Then, the photoresist is dropped in the center of the substrate and the sample is spined using the introduced values of spinning time, speed and acceleration, after which a thin film is coated in the substrate.

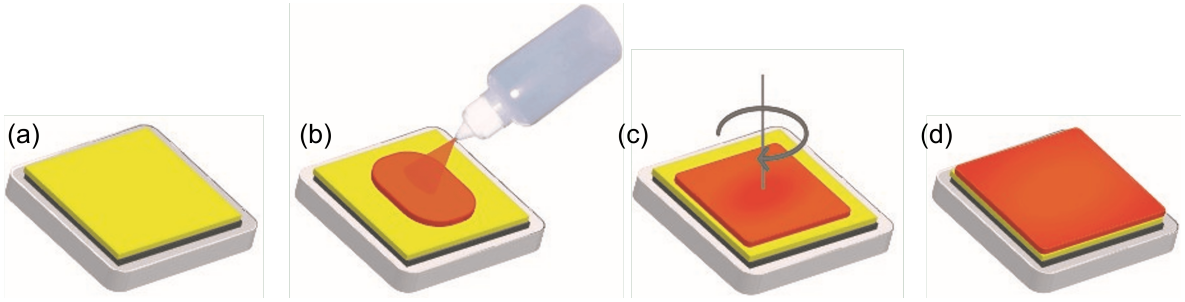

FIGURE 3.13: Sequential steps of a spin coating process: (a) silicon substrate with an Au thin film; (b) dropping photoresist on top of the sample; (c) spin coating and (d) final sample coated with photoresist.

The combination of the spin speed and time defines the thickness of the photoresist. Usually this information is reported in the data sheet of each photoresist. Commonly, high spin speed combined with long spin time create thinner films.

One problem associated to this technique is the coating of non-circular substrates. In these cases, the edges of the substrate will have different thicknesses than the central region. Thus, when exposing the pattern, we need to choose the most uniform part of the substrate because lithographic resolution is related with the photoresist thickness and the exposure energy [60]

3.3.2.2 Pre-bake

After spin coating, the photoresist suffers a thermal treatment called pre-bake or soft bake. This step is performed in a hotplate and is necessary to evaporate the excess of solvent present in the photoresist thin film. The soft baking temperature and time are important to consolidate the photoresist and to promote the adhesion. For shorter baking times and temperatures, the solvent is not completely evaporated and creates dark erosion in the wafer and poor adhesion to the substrate. On the other hand, when the baking temperature and time are larger, the low solvent concentration creates cracks and the photoactive compound is damaged [61]. In the case of under baked positive photoresists, the exposed and unexposed areas are equally attacked by the developer. Thus, the baking time and temperature should be well optimized. At the end of the soft bake process, the thickness of the photoresist is reduce and it becomes more resistant to chemical and physical attacks.

3.3.2.3 Exposure

When the photoresist is submitted to UV-light or a laser beam, its properties change and we can write a pattern on it. During exposure a photoreaction occurs and the photoactive compound becomes carboxylic acid, which is soluble in the alkaline solution. Thus, when the photoresist is illuminated with a pattern, the exposed area will change its solubility, creating a solubility change in the photoresist layer [62].

Direct laser write is a type of lithography that uses a laser beam as the light source. The wavelength of the laser is about 400 nm, that corresponds to a visible violet light. In this case, the patterning is transferred because the optical absorption curve of the photoresist is broad and smoothly drops to zero for high wavelengths. Therefore, using an adjusted exposure energy dosage, we can expose with wavelengths outside the maximum sensitivity of the photoresist. However, the lower sensitivity requires more exposure energy to write the pattern [62].

3.3.2.4 Post Exposure Bake

Before development and after exposure, the sample is submitted to another thermal treatment named Post Exposure Bake (PEB). This treatment modifies chemically and mechanically the photoresist. During PEB, mechanical stresses (created during the soft bake and exposure steps) are reduced and the adhesion of the photoresist to the substrate is improved. Moreover, PEB completes the photoreaction initiated during exposure and improves the diffusion of

the carboxylic acid from the photoactive compound [63]. Post Exposure Bake is an optional treatment but, for the photoresist used in this thesis, this process was employed.

3.3.2.5 Develop

The development process consists in placing the sample in a solution constituted by an alkaline solution and deionized water. The development rate is related with the concentration of the developer. Therefore, high (low) developer concentration in the solution produces high (slow) development rates. Another important factor for the development rate is the exposure energy. When the exposure energy is optimum, the photoactive compound is converted into carboxylic acid, allowing constant and high development rates. Thus, the combination of high developer concentrations and optimum exposure energies leads to shorter development time [64].

Chapter 4

Fabrication of gold-mushroom microelectrodes

The fabrication and optimization of gold-mushroom microelectrodes arrays aiming the recording of neural activity are the main topics of this chapter. The chapter begins by describing the optimization of the lithographic process to understand and optimize the structures size. The study and optimization of gold electrodeposition on unpattern and pattern (including e-beam lithography) substrates is then presented. Finally, a brief conclusion and a comparison between the results for the used parameters is presented.

4.1 Lithography optimization

In this section we describe the optimization of the lithographic processes necessary to obtain well defined and homogeneous holes with 1.5 and 2 µm of diameter. To obtain such size, it was necessary to optimize the spin coating parameters and the adequate exposure dosage of the photoresist, to transfer the desire pattern into the substrate.

4.1.1 Spin coating

Before coating the sample surface with photoresist, it is necessary to clean it. To clean the gold coated substrate, first the substrate was placed in acetone in an ultra-sonic bath for five minutes. After that, the sample was placed for five more minutes in an ultra sonic bath with isopropanol. Finally, the substrate was washed with deionized water and was dried with N_2.

After the cleaning step, the sample was placed in a spinner and fixed by vacuum. When the operational values are chosen (spin speed, acceleration and time), the photoresit was dropped in the center of the substrate and the spinning process initiated (Fig. 4.1).

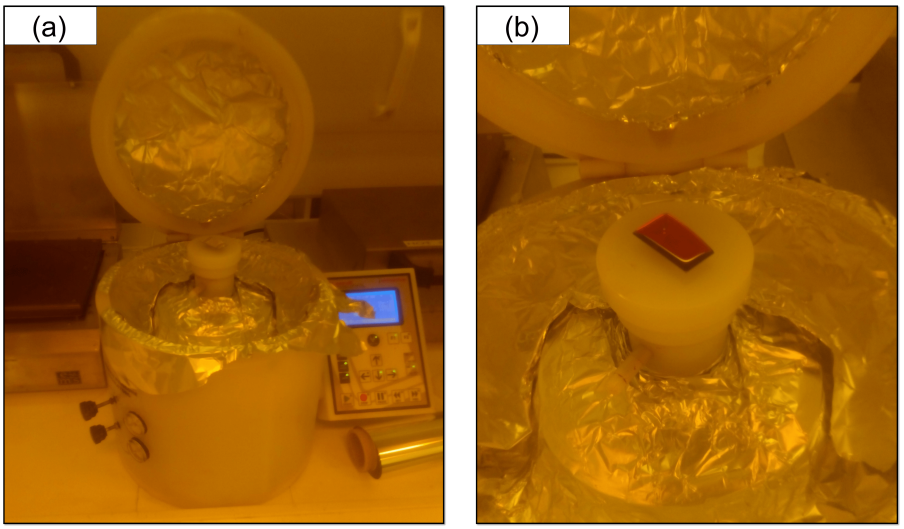

FIGURE 4.1: The spin coating process implemented for our samples: (a) the sample fixed in the spinner and (b) the photoresist placed in the sample surface.

The substrate is then placed in a hotplate to perform the soft bake (during 1 min at 110 °C). The two photoresist used ($S1818$ and $S1805$) have the same chemical properties, but different viscosities, with the $S1818$ being more viscose than the $S1805$. This implies that, for the same operational values (spin time and spin speed), $S1818$ will be thicker than $S1805$ (table 4.1).

TABLE 4.1: The values of the final thicknesses for the two photoresists prepared with same operation values.

Photoresist	**Time** s	**Spin speed** rpm	**Thickness** µm
S1805	30	2000	0.73
S1818	30	2000	2.5

4.1.2 Exposure energy dosage

After analysing the data from the spin coating process, we optimized the exposure energy dosage by performing an energy series in the µPG 101 tool from Heidelberg Instruments. In the Direct Write system, the user can choose the laser power, in mW (from 1 to 70 mW), and the pixel pulse duration, in percentage (from 1 to 100 %). To find the most adequate exposure energy, the pattern shown in Fig. 4.2(a), was written. The pattern is constituted by an array of circles with 2 µm and 1.5 µm of diameter and a pitch of 10 µm, filling a total area of 4 mm^2.

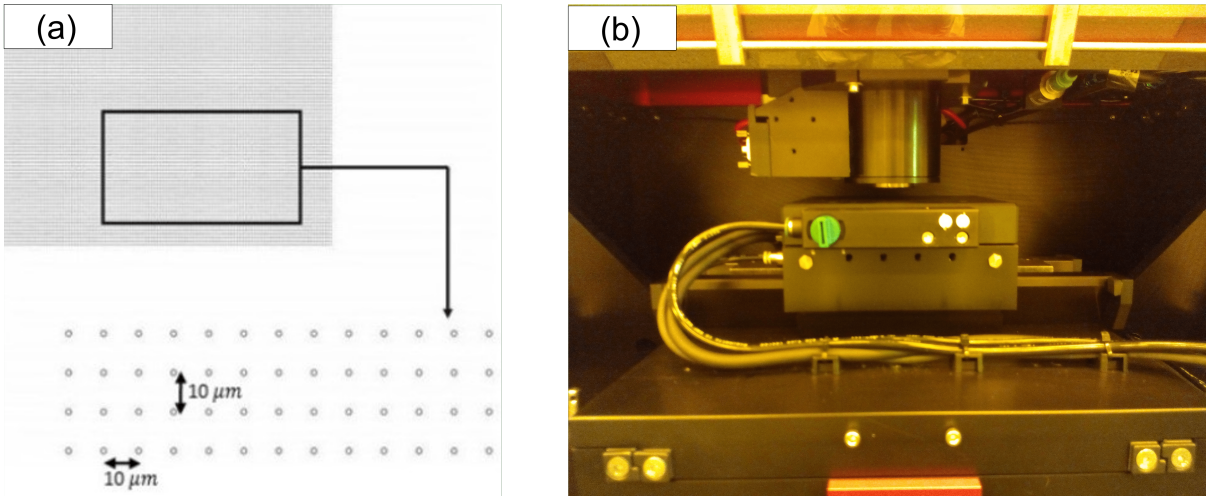

FIGURE 4.2: The exposure step: (a) Pattern designed in AutoCad and (b) optical lithography system.

4.1.2.1 $S1818$ photoresist

For the $S1818$ photoresist coated at 7 krpm for 30 s (leading to a thickness of 1.5 µm) we started by applying an exposure energy series from 10 mW with 100% of pixel pulse duration to 70 mW with 100%.

At the end of the process, optical inspection of the developed samples allowed us to conclude that the most favourable conditions for pattern imprint were at an exposure of 10 mW, although the size was not the desired. To achieve the most favourable pixel pulse duration, in order to obtain the 2 µm size of diameter, we performed a new, more detailed series of pixel pulse duration values between 5% and 30% at 10 mW. This showed us that the most favourable pixel pulse duration was at 17%, as shown in Fig. 4.3(a). Furthermore, when performing the electrodeposition step, we found 10 mW and 12% is the minimum energy required to expose the total thickness of the photoresist (see below).

In order to achieve the 1.5 µm size of diameter, the same procedure was performed. An exposure energy series was implemented and, through optical inspection, we determine that to transfer the pattern it is necessary to apply 20 mW with 50%. Such size optimization was performed only for the $S1818$ photoresist. Figure 4.3 (b) shows the pattern transferred to the sample.

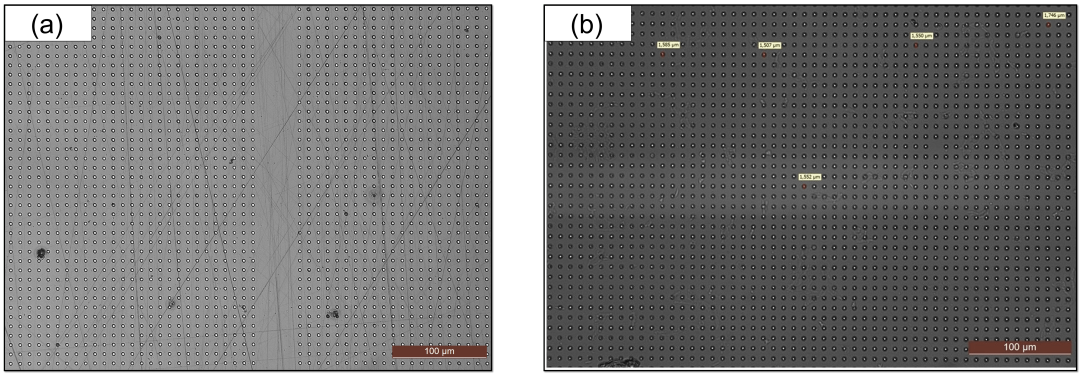

FIGURE 4.3: Optical microscope images of the transferred patterns produced in $S1818$ with (a) 2 and (b) 1.5 µm.

4.1.2.2 $S1805$ photoresist

A similar study was performed for the $S1805$ photoresist. For the $S1805$ photoresist, coated at 2 krpm for 30 s (leading to a thickness of 0.73 µm), we started by applying an exposure energy series, from 10 mW with pixel pulse duration variable fdrom 5% to 18%. The most favourable values obtained was 10 mW with 9% of pixel pulse duration. Figure 4.4 shows the pattern correctly transferred to the sample and the circle structures well designed.

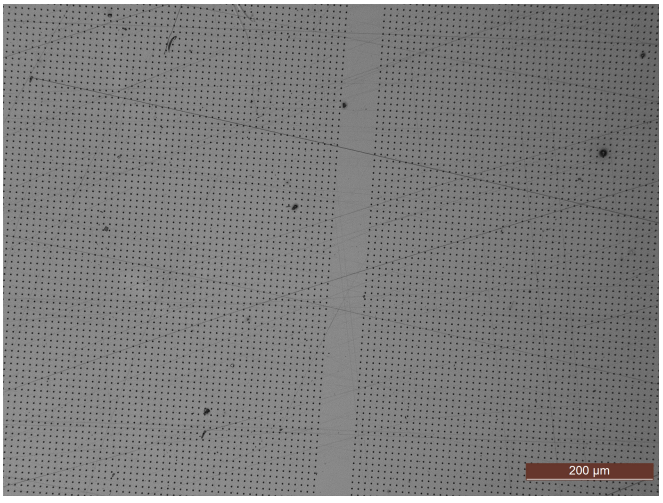

FIGURE 4.4: Optical microscope images of the transferred patterns produced in $S1805$ with 2 µm.

4.2 Gold electrodeposition

4.2.1 Voltammetry

The Voltammetric Cycle is an electro-analytical technique and is usually one of the first experiments performed in electrochemical studies. These cycles study the electrochemical properties of the solution, like the oxidation and the reduction region, the reversibility of the reaction, the reduction potential, etc. To deposit a material, the most important part is the reduction region [65][66]. In this work, these cycles were performed to identify the chemical properties of the gold reduction reaction of the Orosene solution. These cycles were realized trough scans of the potential between $+2.0$ V and -2.0 V, where the current between working electrode (sample) and the counter electrode (Pt electrode) was recorded. The cycles were performed with different scan ramp rates $(\mathrm{V/s})$, as shown in Fig. 4.5.

Figure 4.5 shows the Orosene voltammetric cycles, where the negative potential region corresponds to the reduction region and the positive potentials corresponds to the oxidation region. All the cycles reveals the same overall behaviour. From -0.6 to -0.8 V there is an increase in the current intensity value, corresponding to the gold nucleation. The gold reduction potential is then identified at -0.92 V. Potentials between -0.8 and -1.6 V allow the reduction of the gold ions from the chemical solution. However, using different electrodeposition potentials results in different deposition rates since, with deceasing potential, the current intensity increases. This leads to an increase of the number of transferred charge and thus the number of ions reduce per minute, also increase. On the other hand, Hydrogen formation appears for potentials below -1.6 V. Also for potentials below -1.6 V, the capacitive current increases, leading to an increase of electrons in the sample surface [67][68][69].

4.2.2 Electrodeposition curves and efficiency

To determine a reference value of the electrochemical efficiency for each potential of the previous voltammograms (Fig. 4.5), we performed several electrodepositions in a cell configuration (Fig. 4.6) for four different potentials. In the cell configuration used for this work, cooper tape was chosen as the conductive substrate and the deposited area was of approximately $0.20\ \mathrm{cm}^2$.

We performed DC electrodepositions, using -0.8, -1.0, -1.3 and -1.6 V for 10 min. Through the analysis of the electrodeposition curves (deposition current versus time; Fig. 4.7), we observe that, for potentials above -1.3 V, the current stabilizes 25 s after the beginning of the gold deposition, but for $V \leq -1.3$ V the current only stabilizes after 75 s. Furthermore, the current

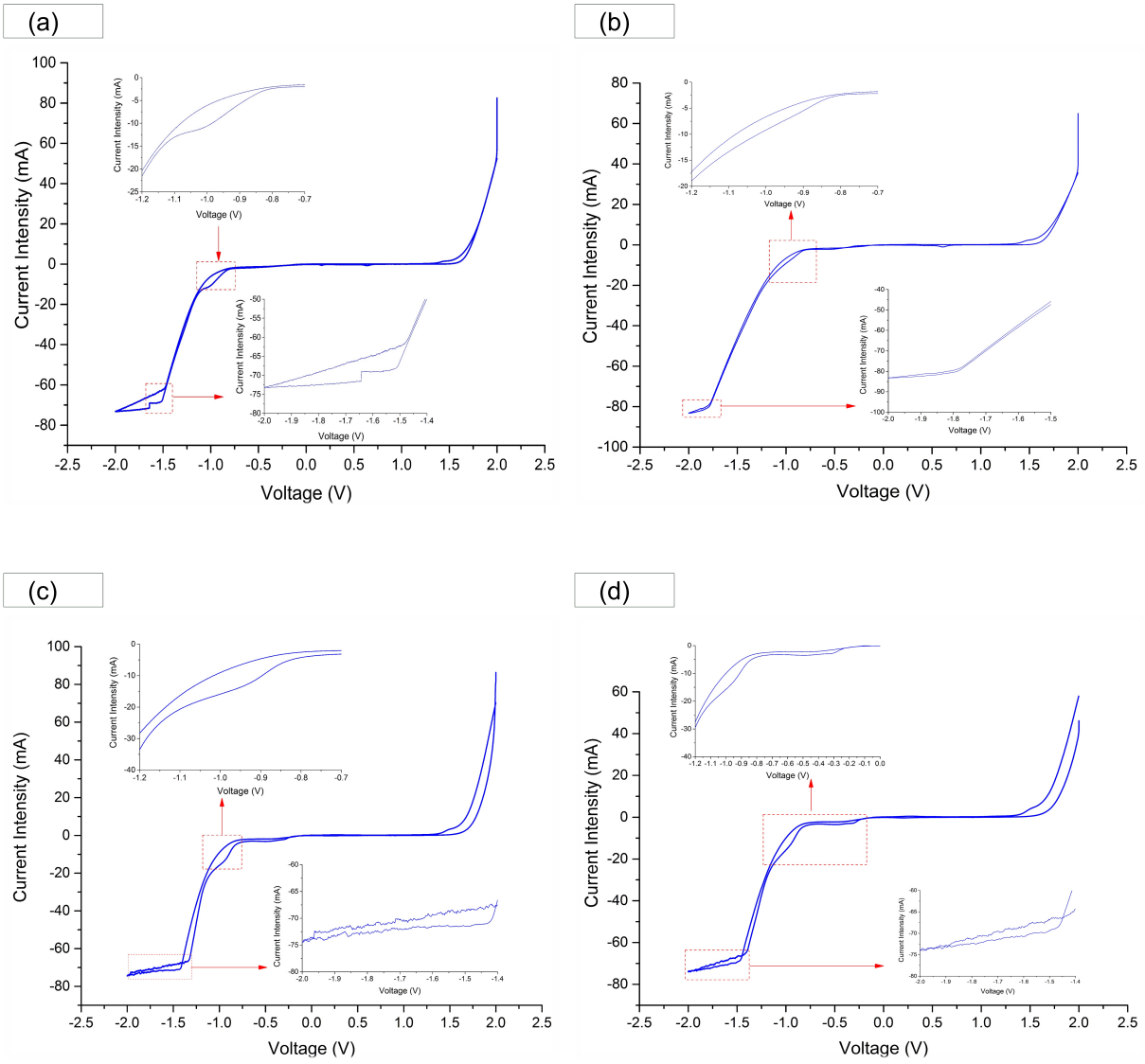

FIGURE 4.5: The voltammogram of the Orosene solution. The cycles were performed with different scan ramp rates, and the potential changed from $+2.0$ up to -2.0 V in scan rates of (a) 10 mV/s; (b) 20 mV/s; (c) 30 mV/s and (d) 40 mV/s.

values for potentials above -1.3 V, are lower in comparison with the potentials below -1.3 V. After the 10 minutes, the samples were removed from the cell and washed with deionized water.

Figure 4.7, shows the current density for the four different potentials. The measurements indicate that, as the potential increases, the current density also increases. So, for the same period of time and deposition area, the thin film grown with -1.6 V is thicker than the thin film deposited with -0.8 V. This occurs because, increasing the magnitude of the electrodeposition potential leads to an increase of the current density and of the number of free electrons, allowing more gold ions to be reduced in the surface of the conductive substrate.

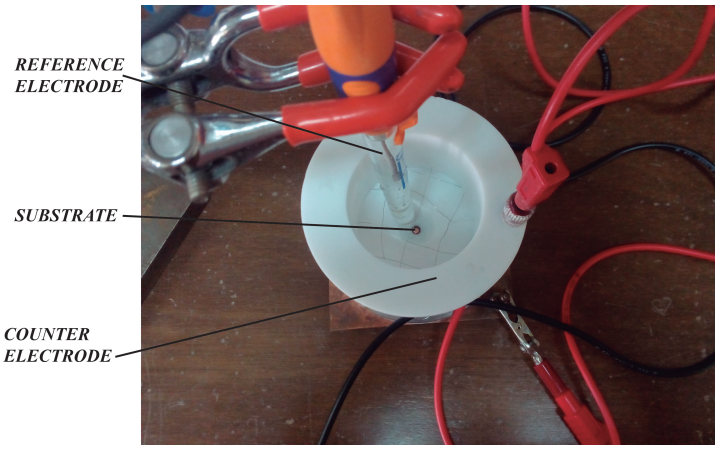

FIGURE 4.6: The electrodeposition set-up in a cell.

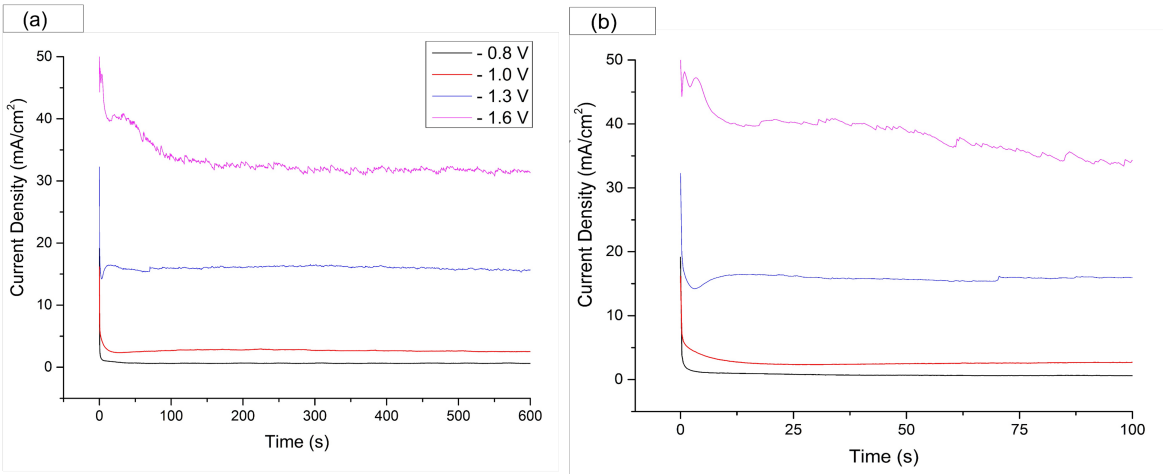

FIGURE 4.7: Electrodeposition curves obtained at different potentials.

To calculate the efficiency of the electrochemical reaction, it is necessary to evaluate the ratio between the deposited mass and the theoretical mass. This ratio is known by Faraday efficiency, and is given by:

$$\rho = \frac{mdep}{mthe} \times 100\%, \tag{4.1}$$

where mdep is the deposited mass and mthe is the theoretical mass. The theoretical mass is obtained using Eq. (3.1). The charge value it is obtained by the time integral of the current intensity. From Fig. 4.8, we find the value of the total charge transferred in the electrochemical reduction equation, for the studied potentials. The total charge values are 0.09 C, 0.15 C, 0.64 C and 0.24 C for the -0.8 V, -1.0 V, -1.3 V and -1.6 V, respectively. Replacing the obtained values and using an Au atomic mass of 197 u in Eq. (3.1), we calculated the theoretical mass. On the other hand, the deposited mass was measured in a precision scale. In Table 4.2 we

summarize the values obtained for the theoretical and deposited masses and of the calculated efficiencies.

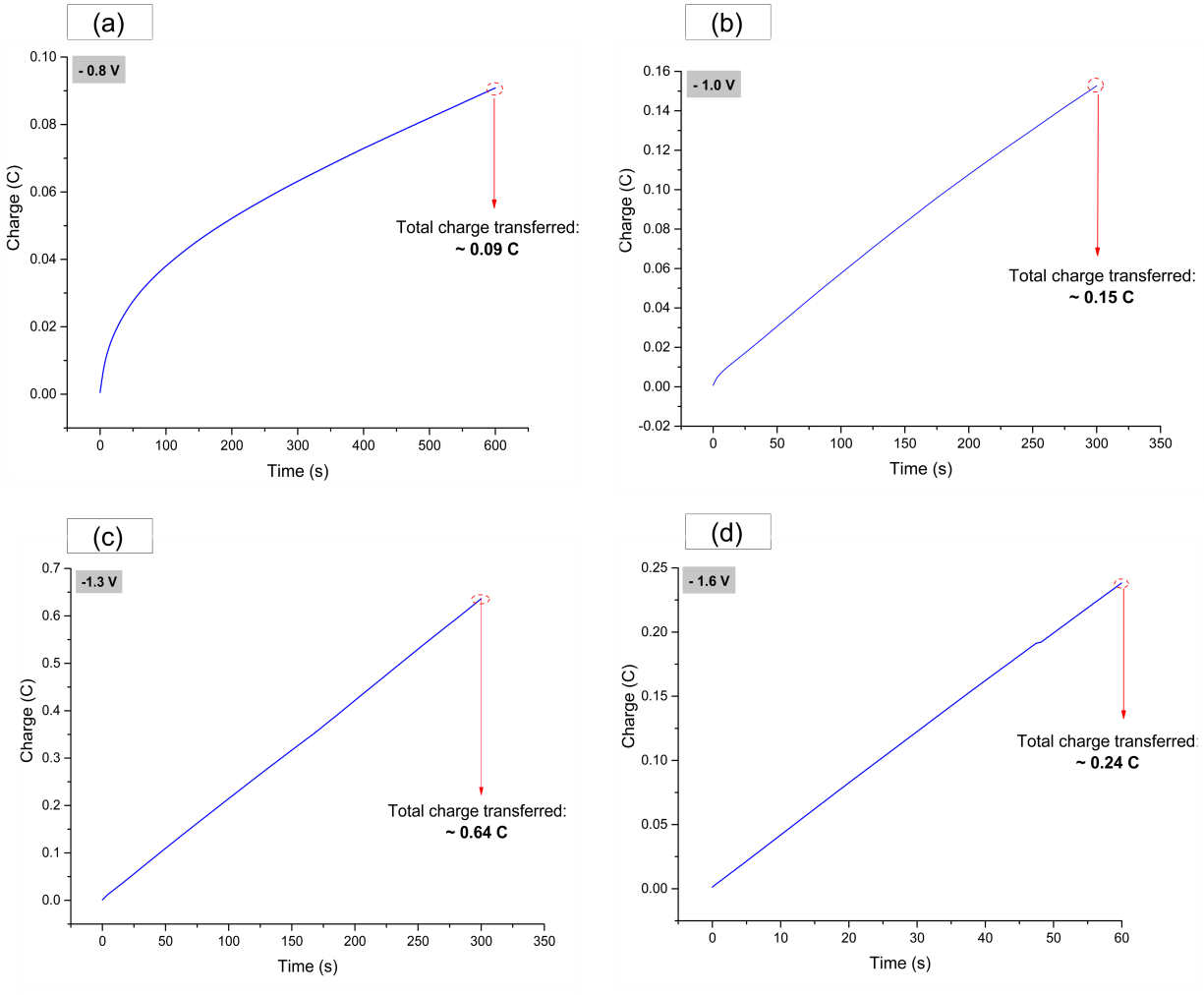

FIGURE 4.8: The total charge transferred in the electrodeposition process at : (a) -0.8 V, (b) -1.0 V , (c) -1.3 V and (d) -1.6 V as a function of the electrodeposition time. The deposition area was 0.20 cm^2.

TABLE 4.2: Deposited an Theoretical gold mass values for four different potentials.

Potential (V)	-0.8	-1.0	-1.3	-1.6
Deposited Mass (g)	0.00005	0.00022	0.00093	0.00045
Theoretical mass (g)	0.00018	0.00031	0.001	0.00048
Efficiency(%)	27.7	70.9	93	93.7

For applied potential of -0.8 V, -1.0 V, -1.3 V and -1.6 V, the efficiency values for the reduction equation are 27.7 %, 70.9 %, 93 % and 93.7 %, respectively. These results demonstrate that the electrochemical reduction equation can have high efficiencies, although the formation

of the $[Au(CN)_4]^-$ complex and hydrogen evolution leads to an overall electrodeposition efficiency below 100%. Nevertheless, those results are in good agreement with values published in the literature [67][68][70]. In our case, the potassium gold cyanide bath, when submitted to a potential, the reduction of gold ion occurs. However, the formation of the $[Au(CN)_4]^-$ complex and hydrogen evolution leads to a decrease in the overall electrodeposition efficiency.

4.3 Electrodeposition in micro-pores

4.3.1 Influence of potential and temperature on the gMμEs morphology

In this section, we present a study of the deposited material as a function of the Orosene solution temperature (23 °C - 35 °C) for different potentials (-0.8, -1.0 and -1.3 V). Note that, for -1.6 V, the photoresist creates cracks and it becomes impossible to deposit the lithographed pattern, because hydrogen is formed in the electrochemical reaction, originating an increase of the pH value that damages the photoresist. Figure 4.9 shows the cap diameter versus temperature for the different applied voltages for 25 min of deposition (-0.8 V and -1.0 V) and 3 min of deposition (-1.3 V). For these experiments, the Orosene solution was heated in a water bath and, during the electrodeposition, the temperature was kept constant by a hotplate.

These graphs clearly reveal that the variation of the temperature of the Orosene solution produces different structures, which implies that, for the same potential, the deposition rate varies with temperature. Figure 4.9 demonstrates that the relation between temperature and cap diameter is linear. Furthermore, the results indicate that, when the temperature increases, the cap diameter also increases. This conclusion implies that the deposition rate and deposited mass increase with the increase of temperature.

Figure 4.10 shows the shape of the produced gold-mushrooms with the $S1805$ photoresist. These micrographs evidence that different structures are obtained for the different potentials and temperatures. The fabricated microstructures acquire distinct shapes when grown with different potentials. For instance, the sample electroplated under -0.8 V at 25 °C did not form the cap of the mushroom. Another anomaly shown by the pictures occurs for -1.3 V at 25 °C. For these conditions, the mushroom shape is also not present because, when the electrodeposition occurs at this potential, the photoresist does not support it leadings to cracks. These cracks destroy the structures and results in a continuous gold thin film. Electrodeposition was difficult for all the samples grown at -1.3 V. Nevertheless, for the temperature of 30 and 35 °C the deposition occurred, although some parts of the array were damage. Figure 4.10 shows that the

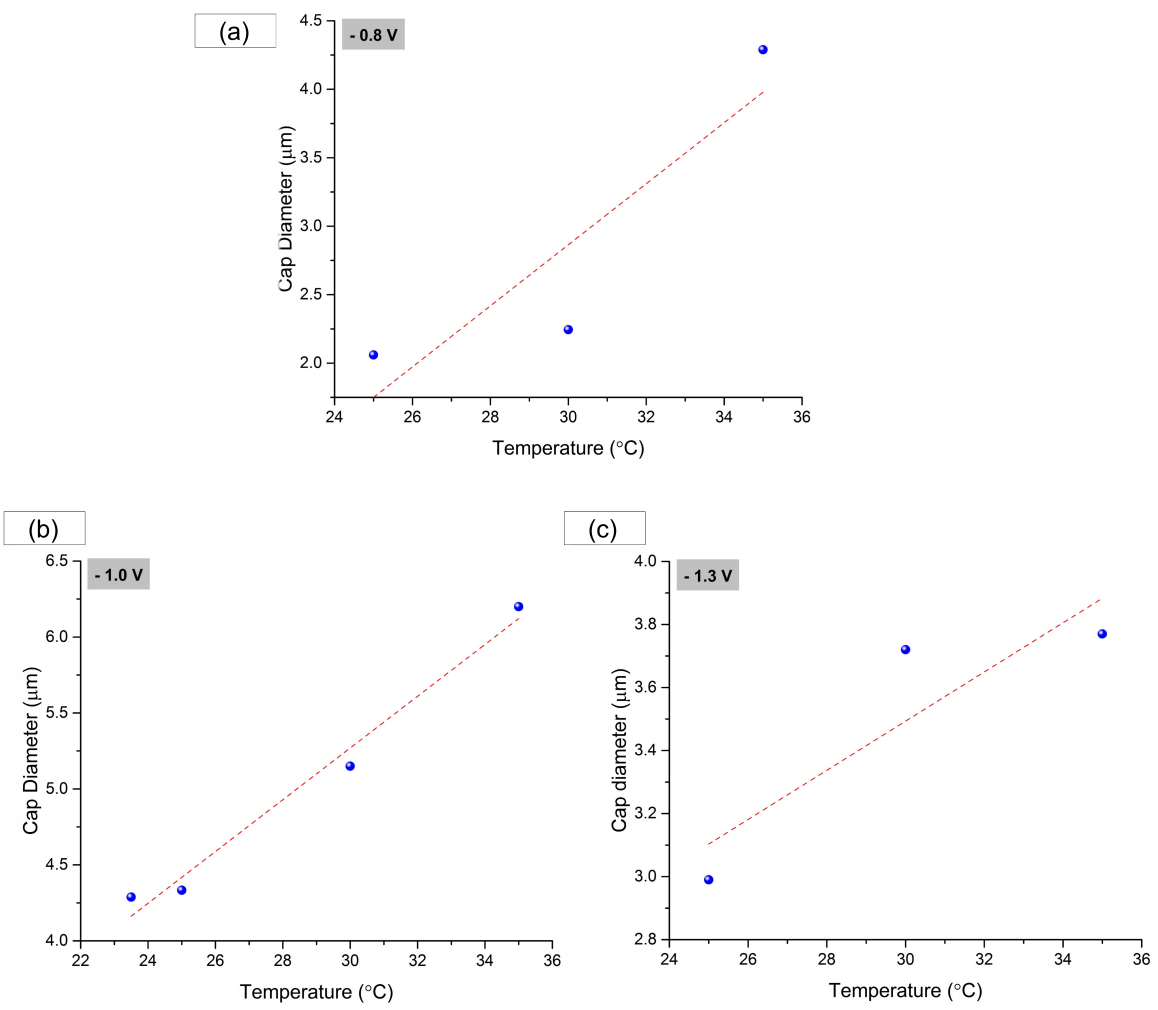

FIGURE 4.9: Cap diameter of the gold-mushrooms grown with different potential as a function of electrolyte temperature: (a) -0.8 V, (b) -1.0 V and (c) -1.3 V.

stalk diameter varies from the base to the top. This difference can be explained by the profile induced on the photoresist during exposure. The laser has a gaussian profile, so that, when the light focuses in the photoresist, the photoresist mimics the beam shape.

Using the ImageJ software, we measured the cap diameter, the mushroom height and the base diameter of the gold-mushrooms. The results are summarize in Table 4.3.

From these results, we can conclude that, for samples electroplated with -0.8 V at 25 °C, the electrodeposition time is not enough to grow a significant cap, because the cap height is of only about 0.17 µm. The other two samples obtained for the same potential (-0.8 V), have an approximate mushroom shape. However, for the case of 35 °C, the cap is still in formation, because this sample had to be exposed with more energy that the others, which created a larger hole. For the sample electroplated with -1.3 V at 25 °C we present no values because

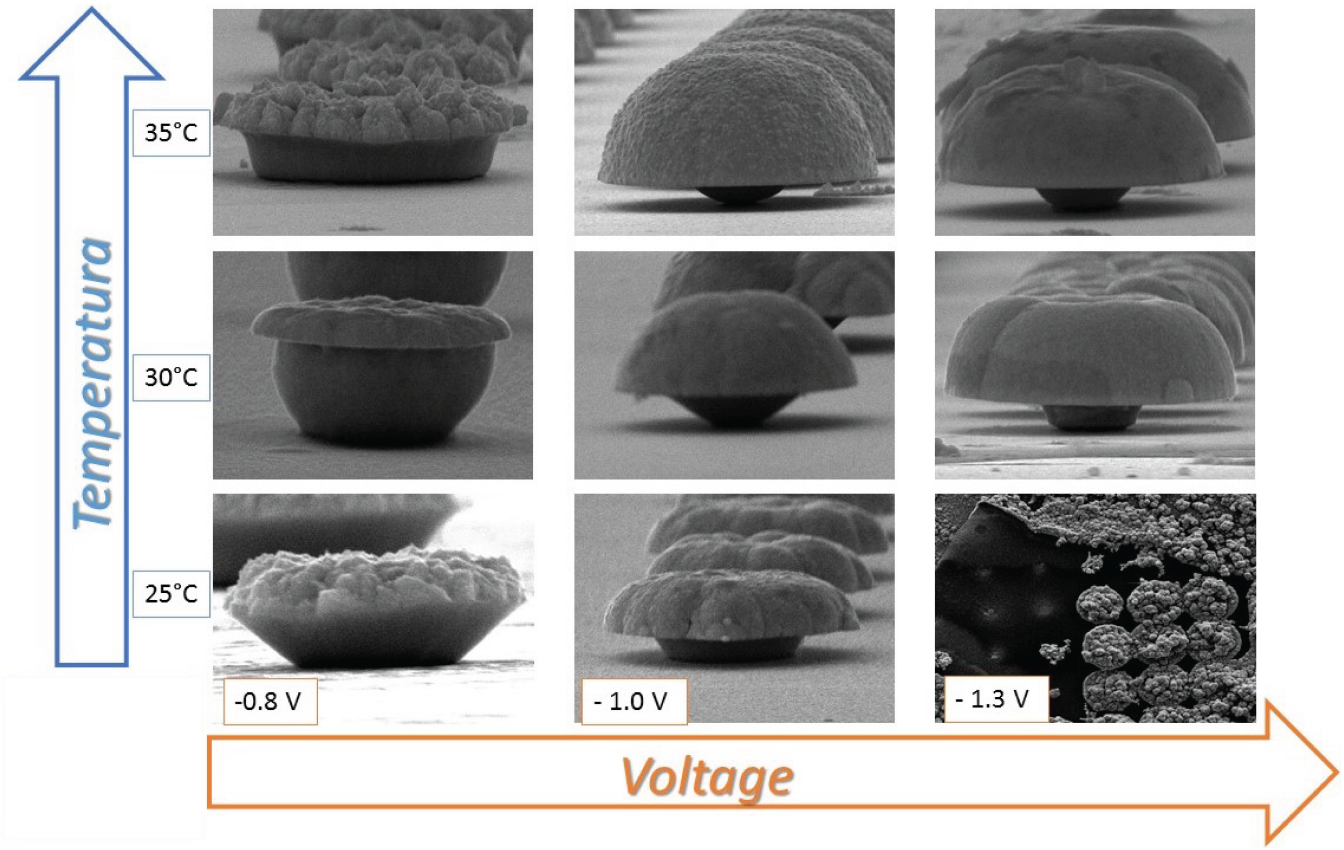

FIGURE 4.10: SEM micrographs of the gold-mushrooms microelectrodes plated at different temperatures and potentials. The structures were created with S1805.

the structures were damaged and the deposition occurred in all the substrate. For the same potential of -1.3 V, the other two samples deposited at 30 °C and 35 °C do present a cap. The cap diameter for 30 °C and 35 °C is 2.67 µm and 3.72 µm, respectively. These cap diameters are smaller than those obtained at -0.8 V and -1.0 V because these samples were electroplated for 3 min only. For the -1.0 V all the samples produced the mushroom shape.

Through the top-view of the SEM images (Fig. 4.11) it was possible to verify that the electrodeposit temperature and potential affect the morphology of the cap. For -0.8 and -1.3 V, the caps present an anomalous shape. For -0.80 V, the cap does not have the semi-hemispherical shape and the cap that is formed looks like a 2D circle. For -1.3 V, the grown cap presents the semi-hemisphere shape but, in the center of the cap, a hole is present. These holes results in a deformation that increases the size with increasing temperature. For the structures growth with -1.0 V, the cap presents the desired semi-hemisphere shape.

From the previous results the potential chosen to perform the electrodeposition was -1.0 V.

TABLE 4.3: Size measurements of the produced gold-mushrooms microelectrode arrays.

$Potential$ (V)	T (°C)	S_D (µm)	C_D (µm)	M_h (µm)
-0.8	25	1.36	2.72	0.92
-1.0	25	2.93	5.95	1.07
-1.3	25	$N.A$	$N.A$	$N.A$
-0.8	30	1.19	2.28	1.177
-1.0	30	0.883	5.25	2.41
-1.3	30	1.96	2.67	3.287
-0.8	35	3.66	4.93	1.01
-1.0	35	1.71	6.20	3.69
-1.3	35	1.34	3.72	2.29

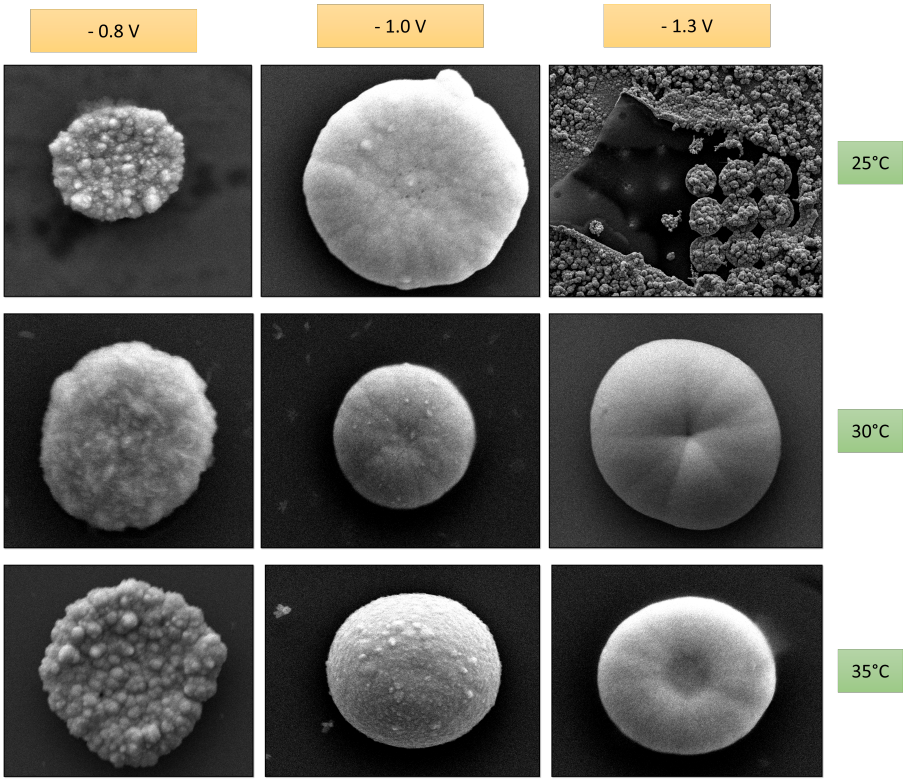

FIGURE 4.11: Top view of the produced gold-mushroom microelectrode.

This value provided the most stable current, the best relation with temperature and the photoresist is preserved at the end of the electrodeposition. In order to determine the deposition rate in the structures, we performed a study with different deposition times for constant temperature and potential. These results are present in the following section.

4.3.2 Electrodepositions at -1.0 V

After analysing the structures grown with different potentials, we performed a study of the deposition rate at -1.0 V. For this study, the gold-mushroom microelectrodes arrays were grown for different times in structures created in $S1805$ photoresist. Another series of samples with $S1818$ was also fabricated, where the temperature and the deposition time was varied.

4.3.2.1 *Minimum exposure energy*

In Section 4.1.2.1, the hole diameter versus pixel pulse duration was studied. The produced sample contained several arrays with different pixel pulse duration, from 5% to 15% with 10 mW. This set of arrays designed in the same substrate was electroplated at -1.0 V during 70 min. At the end, it was possible to see that, from the arrays, only four were actually electroplated, corresponding to pixel pulse durations value between 12% and 15%. Figure 4.12 shows the produced gMμEs at 12% and 15% pixel pulse duration, for a power of 10 mW. SEM images of this sample reveal that some gMμEs jumped from the surface of the gold thin film (Fig. 4.13).

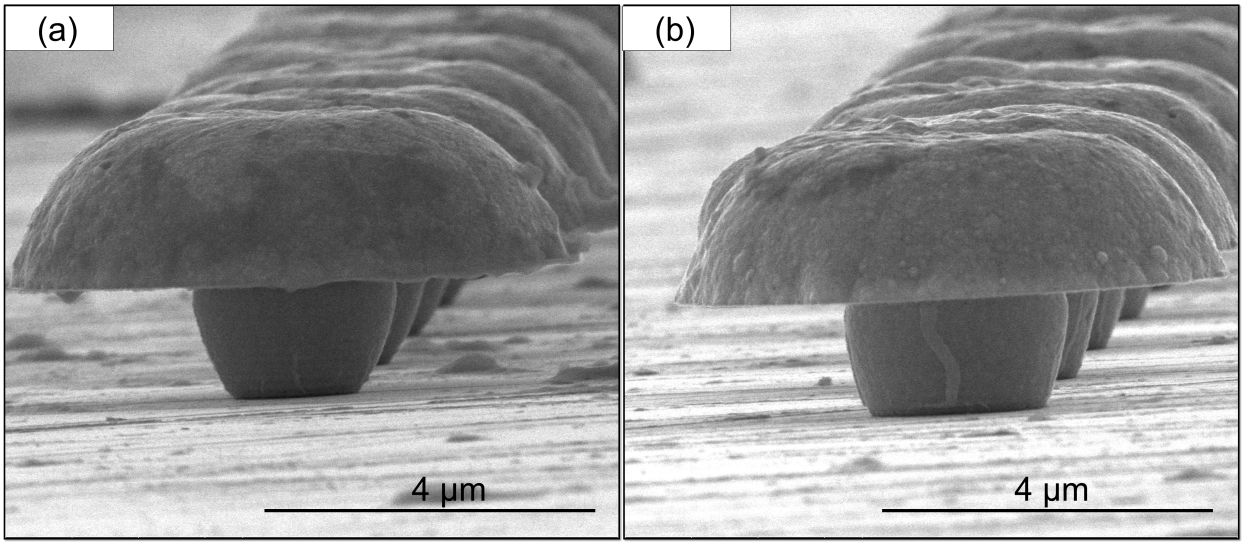

FIGURE 4.12: SEM images of the microelectrodes produced by two different pixel pulse durations: (a) 12% and (b) 15 %.

4.3.2.2 *Structures grown with different deposition times*

The first study was to grow structures with different deposition times. Figure 4.14 shows the top-view of the deposited array and the distribution of the cap diameter in each of the produced samples. All the graphs represented in Fig. 4.14 show a normal distribution (red line).

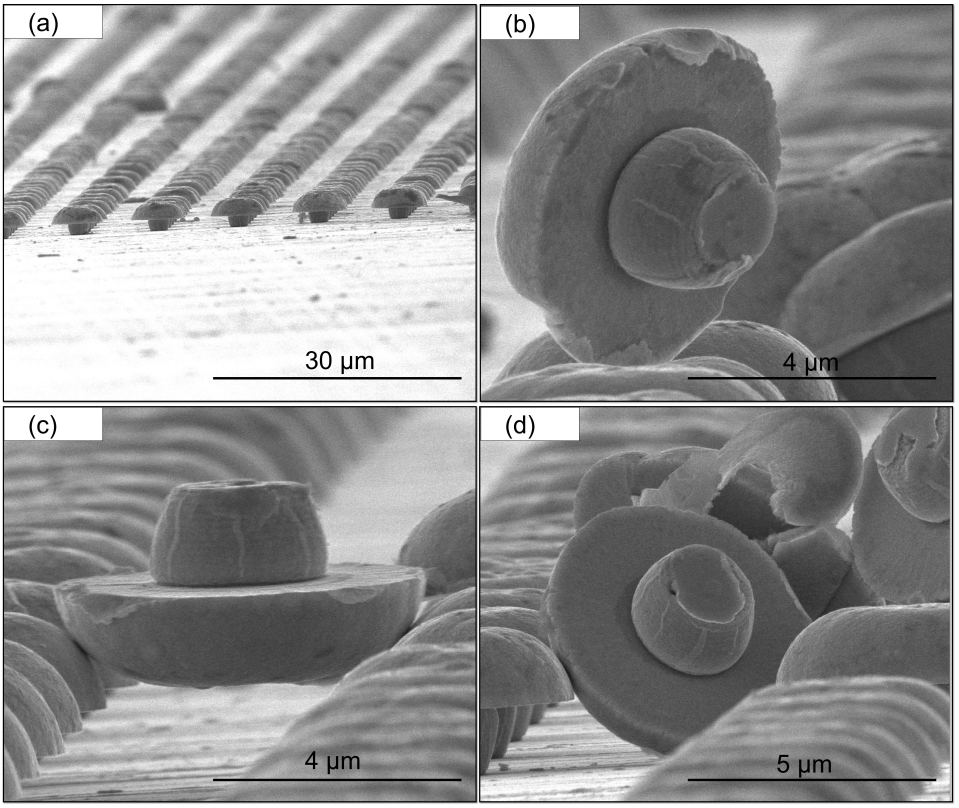

FIGURE 4.13: SEM image of the microelectrodes produced at 10 mW with 15%. (a) Array of microelectrodes;(b), (c) and (d) microelectrodes seen at different positions.

Figure 4.14(a) shows the cap diameter of the gold-mushroom produced for 5 min of electrodeposition. The major part of the produced microelectrodes have the cap diameter between 1.92 and the 1.94 µm, with an average value of 1.93 ± 0.03 µm. Figure 4.14(b) shows the results for 10 min of deposition. For this sample, the microelectrodes produced have caps between 2.69 and 2.78 µm, but the majority of the microelectrodes has cap diameters between 2.74 and 2.75 µm. The average value of the cap diameter for this distribution is 2.74 ± 0.02 µm. In the case of 15 min of electrodeposition, the average value of the cap diameter is 2.60 ± 0.08 µm while for 20 min, it is 3.18 ± 0.24 µm.

Figure 4.15 shows the cap diameter as a function of the deposition time. This graph demonstrates that the increase of the deposition time leads to an increase of the deposited material. However, for the sample produced during 15 min this is not verified. In this case, the cap diameter is smaller because the current is lower in comparative with the others samples and a decrease in the current value implies a larger deposition time to produce the same results. In fact, the current in the sample electrodeposited for 10 min was about three times higher than that of the sample electrodeposited during 15 min. This difference leads to a lower amount of transferred ions and lower deposition of material.

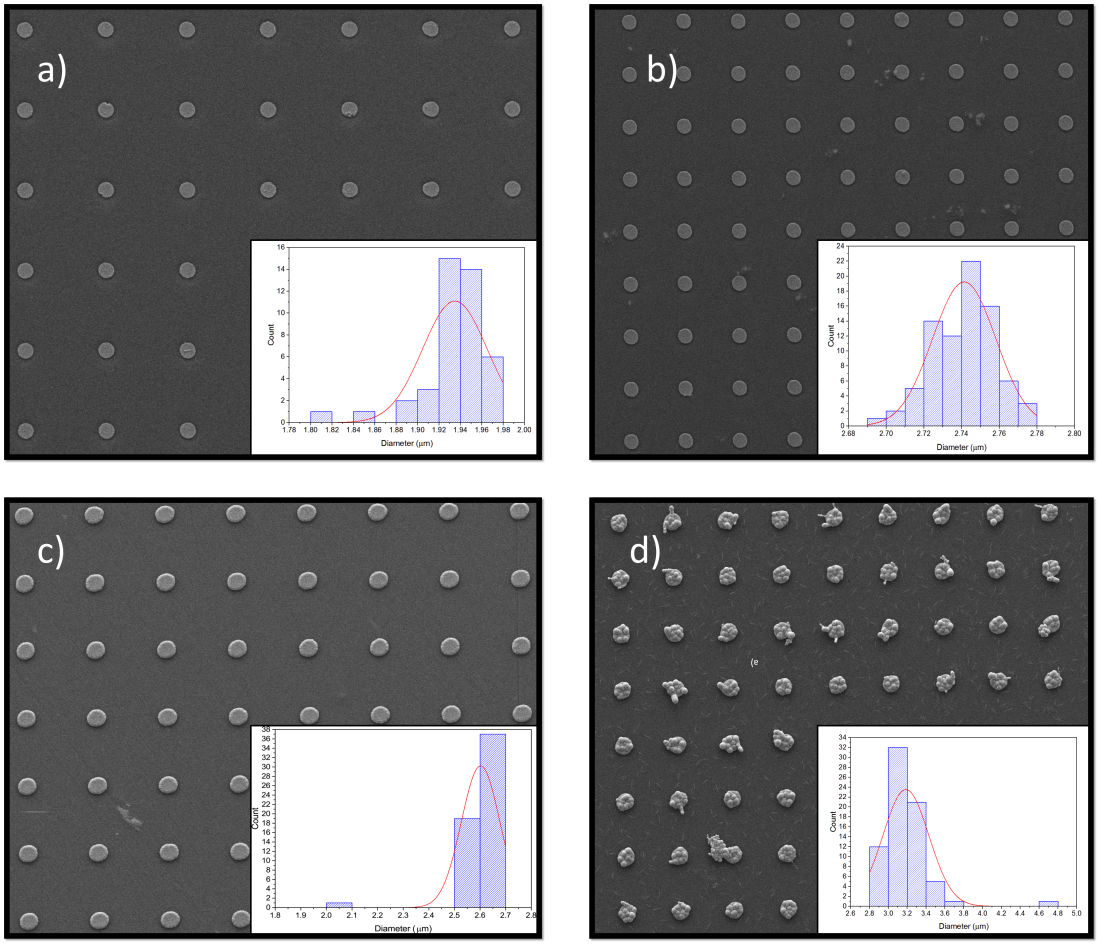

FIGURE 4.14: Arrays obtained for different deposition times with the electrodeposition temperature (23.5ºC) and potential (-1.0 V) constant.

4.3.2.3 *Structures grown with different temperatures and deposition times*

The deposition rate is the ratio between the deposited thickness and the deposition time. To obtain this value for each temperature used (25, 30 and 35 °C), we electroplated gold in the microstructures for three different times (15, 20 and 30 min). SEM images of the structures deposited with different times. Analysing Fig. 4.16, we verify three different shapes in the microelectrodes deposited. When comparing the gMμEs produced at lower temperatures (25 and 30°C) with those produced at 35 °C, we concluded that the structures do not have the mushroom cap. This happen because of the low deposition time and lower deposition rate. Figure 4.16(c) corresponds to the structure deposited at 35 °C, where the onset of the mushroom shape is verified. Again using ImageJ we were able to measure the height of the deposited material. For the depositions at 25 °C, 30 °C and 35 °C we obtained 0.69 µm, 0.93 µm and 1.22 µm, respectively, giving deposition rates of about 46 nm/min and 62 nm/min, for 25 °C and 30 °C, respectively .

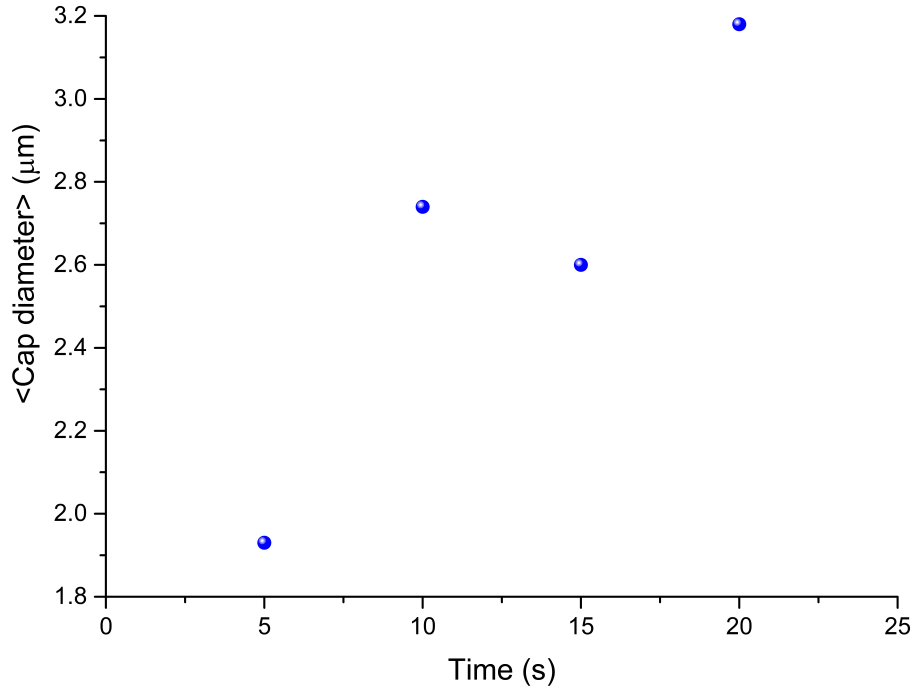

FIGURE 4.15: The cap diameter obtained for different times at -1.0 V.

For 20 min of deposition, through the SEM images it is possible verify that only the sample electroplated at 25 °C, did not produced the mushroom shape, because the deposition time was not sufficient. Analysing the stalk produced, we obtain a height of 0.90 µm. Relatively to 30°C and 35°C , the mushroom shape was obtained. The microelectrodes deposited at 30 °C had a stalk height with 1.12 µm while for 35 °C it was 1.10 µm.

A similar study was performed for an electrodeposition time of 30 min (Fig. 4.16). Total heights of the gold-mushrooms (stalk height plus the cap height) are 1.15 µm, 1.39 µm and 2.53 µm, for depositions at 25 °C, 30 °C and 35 °C, respectively. All depositions produced the mushroom shape. For 35 °C, the deposition rate was calculated including the total height of the gold-mushroom microelectrodes arrays produced. Thus, for 15 min of deposition we obtain 1.37 µm of mushroom height; for 20 min we obtain 1.71 µm and for 30 min we obtain 2.53 µm. For this case, the deposition rate is of approximately 85.2 nm/min.

A more detailed analysis of the obtained structures reveals that the deposition rate varies with the type of deposited structure. In other words, the deposition rate of the stalk is different from that of the cap. For the cap deposition rate we obtain, at 25 °C, 54 nm/min, while for 30 °C, we obtain 73.5 nm/min. These deposition rates were calculated for the cap height.

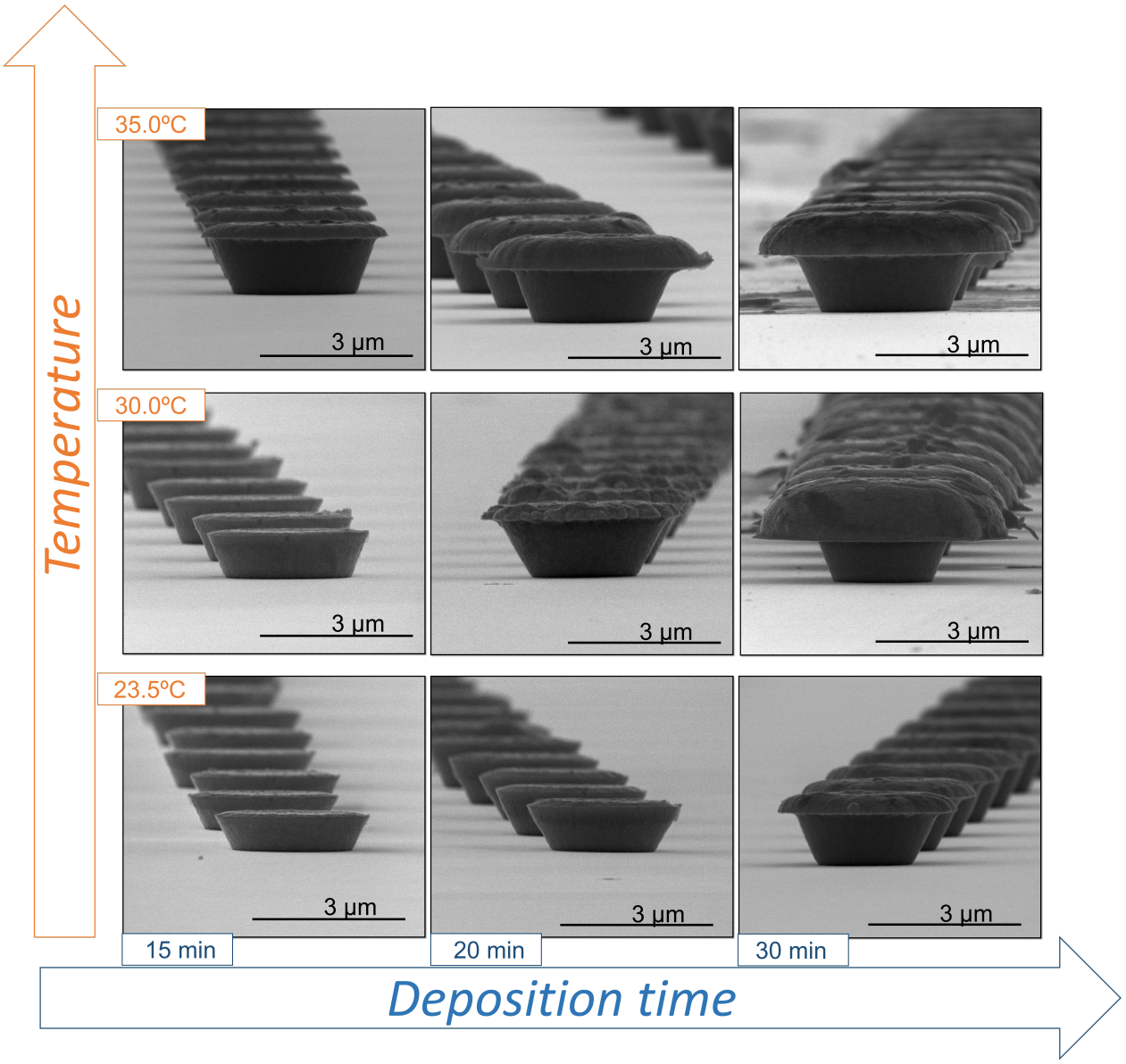

FIGURE 4.16: SEM images of electrodeposited structures at -1.0 V during 15 min, at different temperatures: (a) 23.5, (b) 30 and (c) 35 °C.

4.4 e-beam lithographed arrays

To produced smaller structures, electron beam lithography was performed at INESC-MN (Lisbon; see Runsheet in Appendix). The produced samples are constituted by a square with 1 mm^2 with holes of 300 and 500 nm with 10 µm of pitch, (Fig. 4.17). These samples were coated with PMMA at 2000 rpm and then baked at 160 °C during 4 min.

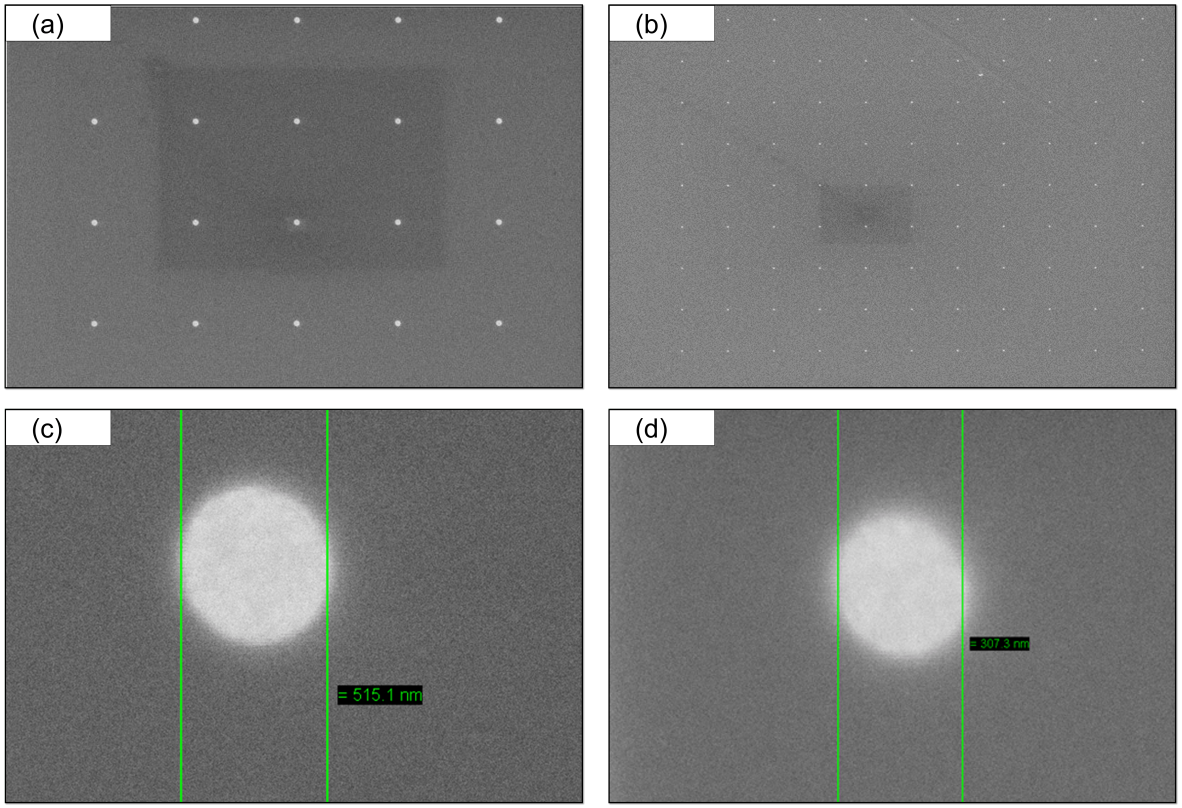

FIGURE 4.17: Nano holes transferred to PMMA.

These nano holes were then deposited during 39 min at -1.0 V and then characterized with SEM. Figure 4.18 shows the top-view of the array.

Figure 4.18(a) shows the cap diameter of the gold-mushrooms grown in holes of 300 nm. The major part of the produced microelectrodes have the cap diameter between 2.0 and the 2.5 µm, with an average value of 2.22 ± 0.02µm. For this sample the cap diameter presents a minimum value of 0.91 µm and a maximum value of 3.09 µm. Figure 4.18(b) shows the results for holes with 500 nm. For this sample, the microelectrodes produced have caps between 2.0 and 2.95 µm, but the majority of the microelectrodes have cap diameter between 2.50 and 3.00 µm. The average value of the cap diameter for this distribution is 2.40 ± 0.02 µm. Then, comparing the distribution obtained for the cap diameter, we verify that structures grown in holes of 500 nm present an uniform distribution in size because the majority of the structures present the same size. Figures 4.18(c)-(d), show the zoom-in top-view of the structures. For these SEM images, we see that the cap grown in the nano holes maintain the semi-hemisphere shape, like desired.

A cross-section analysis was performed to determine the stalk and cap characteristics. Figure 4.19 shows the SEM images taken. Through ImageJ we measured the cap and stalk diameters, and the stalk and mushroom height. For the nano holes of $300\ nm$, the cap has a diameter and

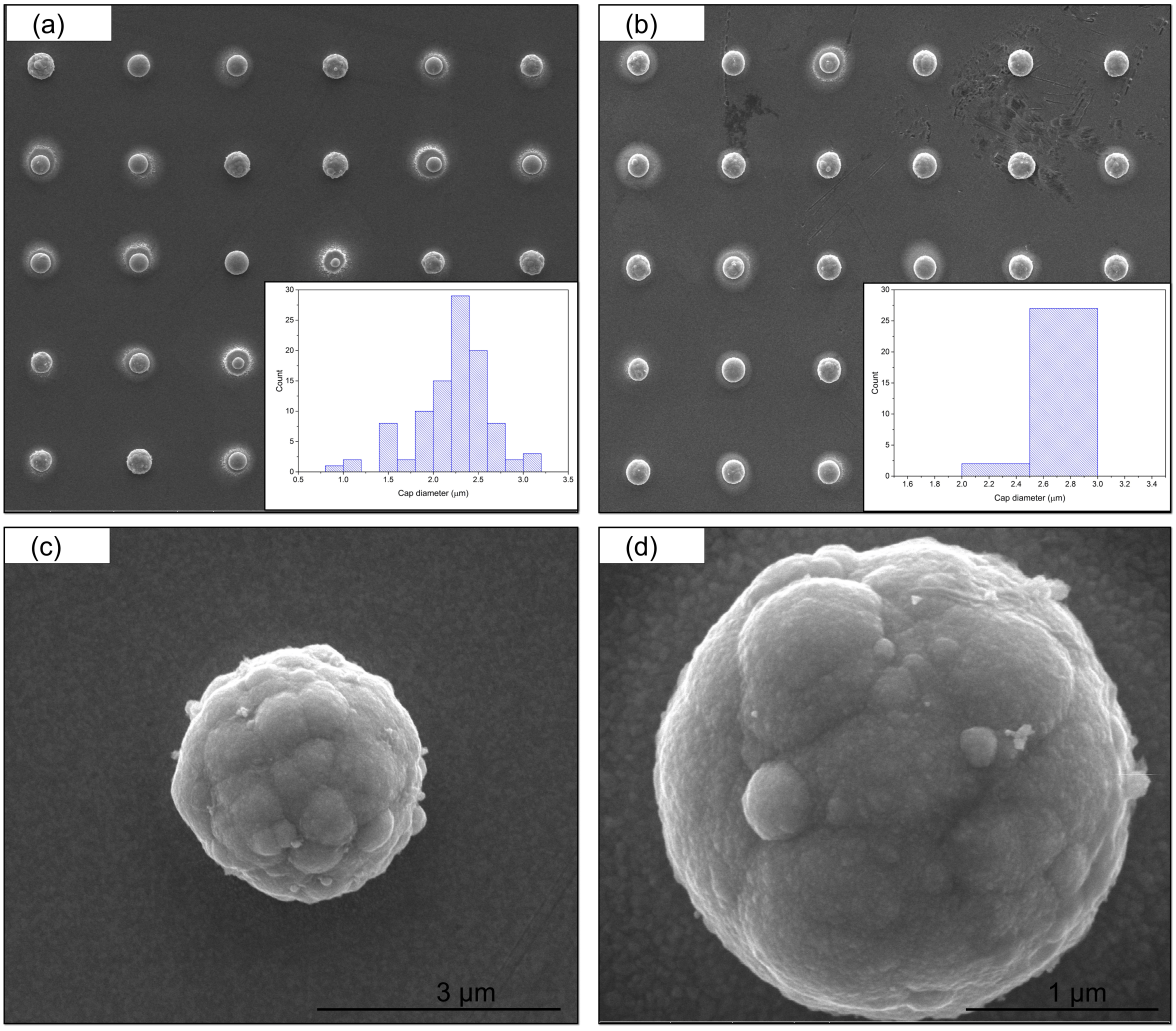

FIGURE 4.18: The gold-mushroom grown in nano holes: (a)-(b) top-view of the 300 nm and 500 nm arrays; (c) and (d) are the zoom-in images of the gold-mushrooms for structures with 300 nm and 500 nm, respectively. The inserts in (a) and (b) represent the distribution of the cap diameter.

height of 2.21 µm and 1.06 µm, respectively, while the stalk has a diameter of 303.08 nm and a height of 171 nm. Holes of 500 nm have a cap diameter of 3.65 µm with a height of 1.80 µm, while the stalk has 519.33 nm of diameter and a height of 175 nm. Comparing the two structures grown with the same time, we observe that structures created in holes of 300 nm present a lower size than grown in holes of 500 nm. The total gold-mushroom microelectrode height is 1.24 and 1.98 µm for holes of 300 and 500 nm, respectively.

The previous experimental e-beam procedure was repeated and the deposition time varied, allowing to create an array of nano-mushroom (Fig. 4.20; electroplated during 4.5 min at -1.0 V) with a base stalk diameter of 525.72 nm and a stalk height of 172 nm. The cap diameter presents a size of 907 nm and the total mushroom height is 355 nm.

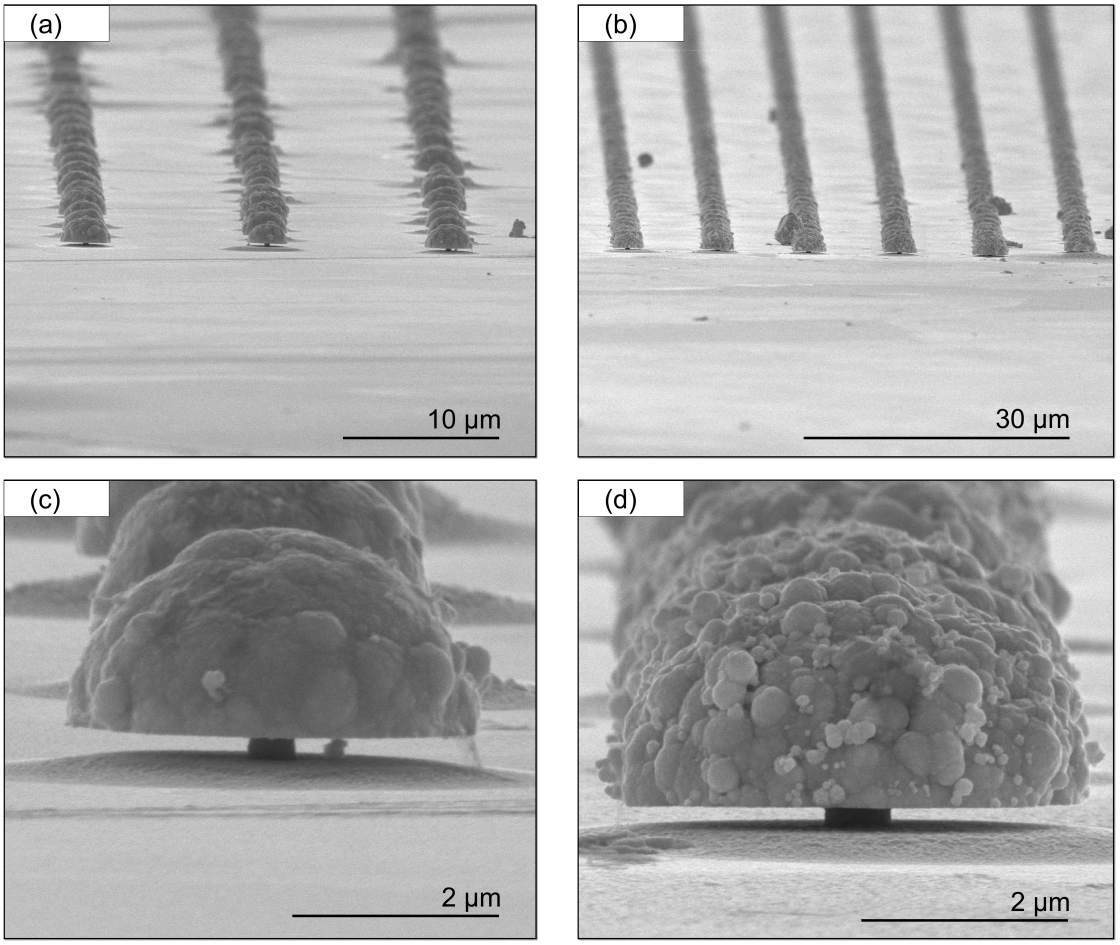

FIGURE 4.19: A cross-section view of the gMμEs grown with (a) and (c) $300\ nm$; (b) and (d) $500\ nm$.

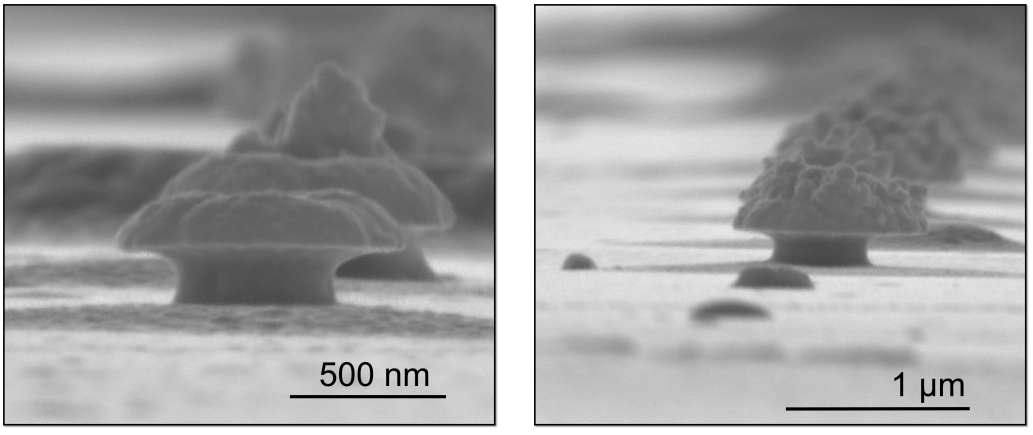

FIGURE 4.20: SEm images of nano-mushroom electroplated at -1.0 V, during 4.5 min.

Chapter 5

Interfacing electrodes and neurons

In this chapter we will present results on the characterization of the optimized gold-mushroom microelectrodes arrays. At the end of the chapter, a preliminary study with cultured neurons on top of the multi-electrode arrays is presented.

5.1 Produced sample

To create an interface between electronics and neuron cells, it is first necessary to produce the samples. To produce the gold-mushroom microelectrodes arrays, we used a Cr (3 nm)/Au (40 nm) structure on a silicon wafer. Then, we fabricated 1.5 µm dots disposed in a square array with a lattice spacing of 10 µm. Gold-mushrooms were then fabricated using electroplating in a gold solution (Orosene E +4gr/lt, for Italgalvano s.p.a.) under -1.0 V for 70 min. The produced gold-mushroom microelectrodes were then characterized using Scanning Electron Microscopy (Fig. 5.1), displaying stalks of 1.4 µm, caps with heights of 1.0 µm and diameters of 3.8 µm. The stalk of the fabricated gold-mushrooms is also seen to vary with the height, increasing from 0.6 µm at the base to 3 µm at the top. The same experimental procedure was used for the 94 min of deposition, where the deposited structures present stalks of 1.3 µm, caps with heights of 1.7 µm and diameters of 4.81 µm.

After the SEM imaging, we performed a structural and electrical characterization that will be described in the following section.

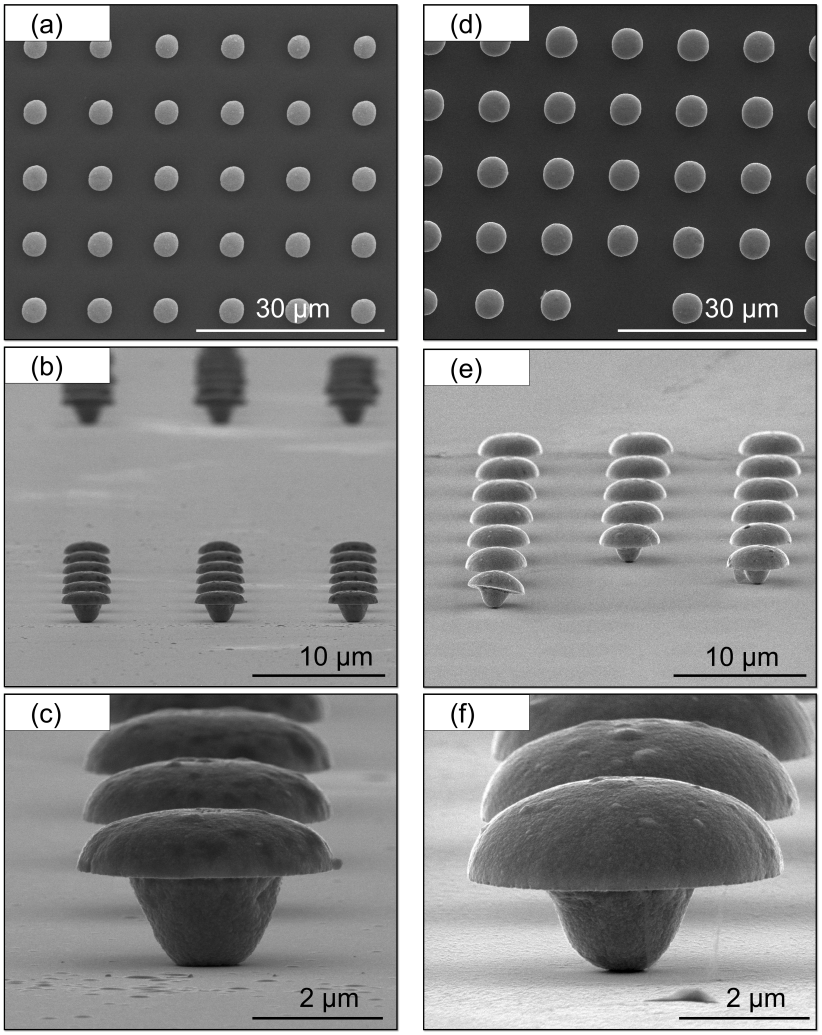

FIGURE 5.1: SEM characterization of the produced gold-mushrooms microelectrodes arrays for (a)-(c) 70 min and for (d)-(f) 94 min.

5.2 Characterization of the gold-mushroom microelectrodes arrays

5.2.1 X-ray diffraction

To identify the atomic and molecular structure of the deposited materials, we performed X-ray diffraction studies. Figure 5.2 shows the X-ray spectrum of the produced sample. In the spectrum, it is possible to identify five distinct peaks (at $33.0°$, $38.2°$, $69.31°$, $69.52°$ and $81.75°$). When comparing the reflection angles with those describe in a known data base (Pearson's Crystal Data), we can identify the peaks as belonging to the gold reflection for 38.25, 44.42 and 81.75 °, while the other peaks corresponds to silicon.

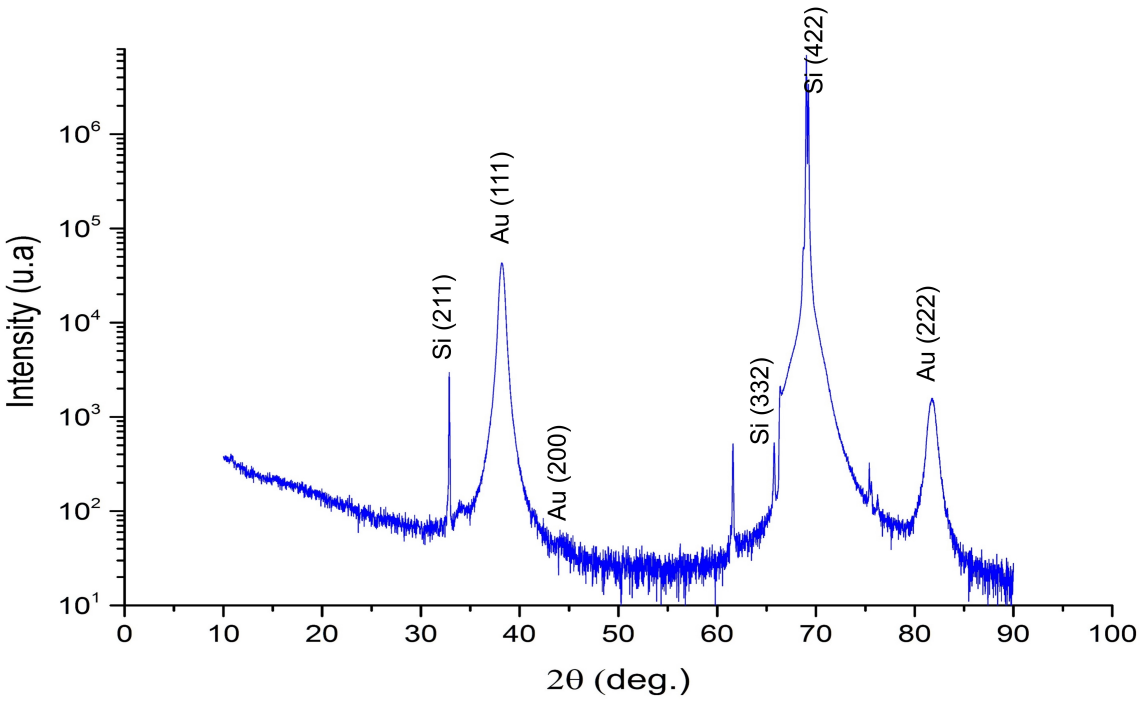

FIGURE 5.2: X-ray spectrum of the sample used to culture neurons cells.

In relation to gold, the obtained reflection corresponds to inter-plane distances of 0.24 and 0.12 nm, for 38.2 ° (111) and $81.7°$ (222), respectively. The majority of the planes is oriented in the (111) direction. Gold is a crystal with a face centered cubic cell, that has the three lattice parameters equal to 4.1 nm, and the total volume of the cell is 6.7 nm^3. Through Eq. (3.7), we obtain a grain size of 3.26 nm for gold oriented in the (111) direction and a grain size of 2.91 nm for the (222) direction.

5.2.2 Electrical Resistivity and Impedance

The resistivity was measured using the four contact method. The value of the resistivity was obtained using Eq. 3.9 and the measured linear I-V curves. For the deposited gold the obtained resistance value was $4.5\ \Omega$. The sample measured 2.5 cm of length by 0.4 cm of width, leading to a resistivity value of $0.018\ \Omega$ m.

To analyse the resistance and capacitance vs frequency of the gold-mushroom microelectrodes arrays, we performed impedance measurements (Figure 5.3). To performed the measurements the microelectrodes were emerged into a PBS (phosphate buffered saline) solution and the solution was heated in a hotplate. In the measurements we used a LabvieW routine, where the frequency and the number of points, is chosen.

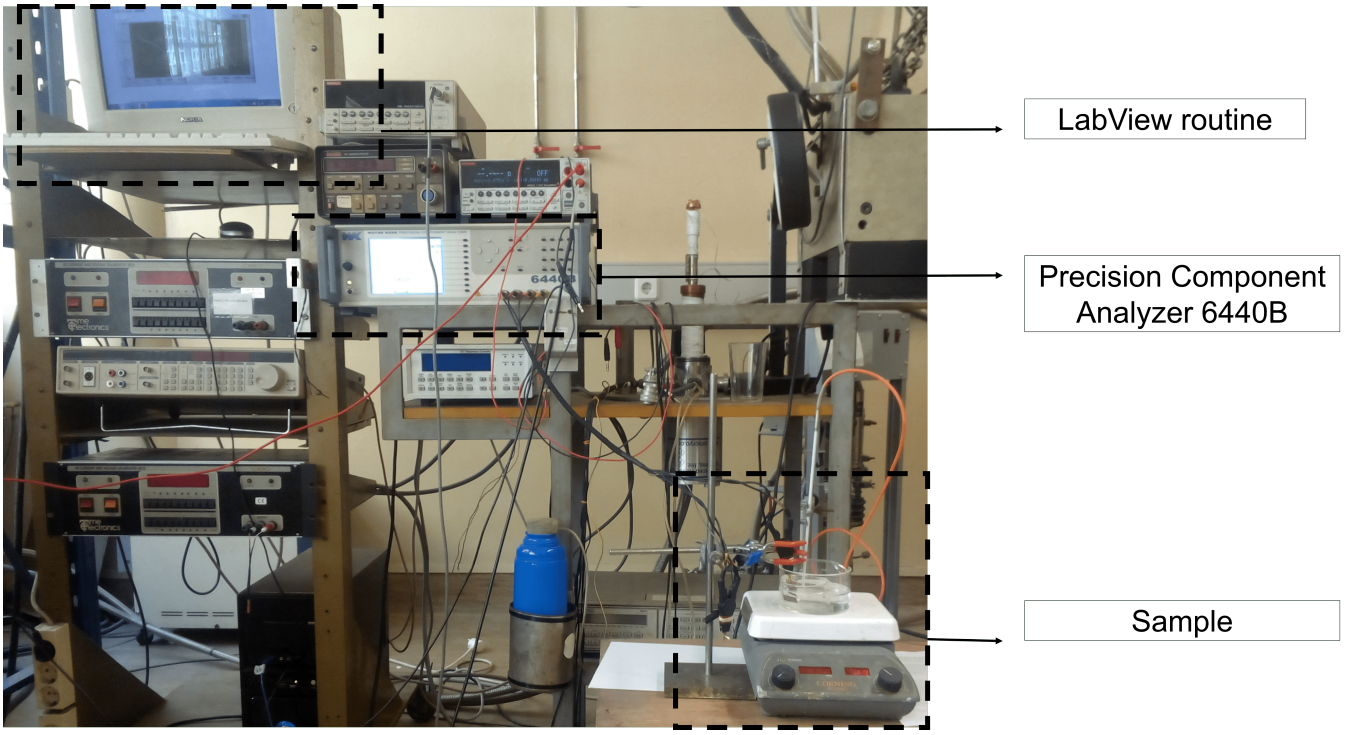

FIGURE 5.3: The set-up for measure the impedance.

Figure 5.4, shows the imaginary versus real values of the impedance. We observe that changes in temperature do not affect the behaviour of the graph. Through the ratio between the imaginary and real parts we can obtained the quality factor. In our case, the imaginary part corresponds to a capacitor, while the real part is the resistance of the set PBS/microelectrodes. Afterwards, we calculated the resistance and capacitance values as a function of frequency.

Figure 5.5(a) indicates that the resistance has the same overall behaviour for all temperatures. For high values of frequencies (in the MHz), the resistance values tend to $70\ \Omega$ while for low frequencies, the resistance varies with temperature. The most important result is at $37\ ^{\circ}\mathrm{C}$ and low frequencies, because these are the condition to acquire neuronal signals. At this temperature and low frequencies, the resistance value is very high(on the order of $\mathrm{k}\Omega$). Figure 5.5(b) indicates the capacitance values of the set PBS/microelectrodes. In this graph we observe that increasing the frequency implies a decrease in the capacitance value. Another fact observed is that, for frequencies above kHz, the capacitance value is too low and all the measurements converge approximately to the same value. For frequencies below kHz, the capacitance values vary from 5×10^{-7} to 3.0×10^{-5} F.

Figure 5.6 shows the thermal evolution of the PBS solution, taken with a thermal camera. The pictures show the existence of a thermal gradient in the PBS solution. The first picture was taken when the solution was removed from the fridge, with a temperature of $-21\ ^{\circ}\mathrm{C}$. As the

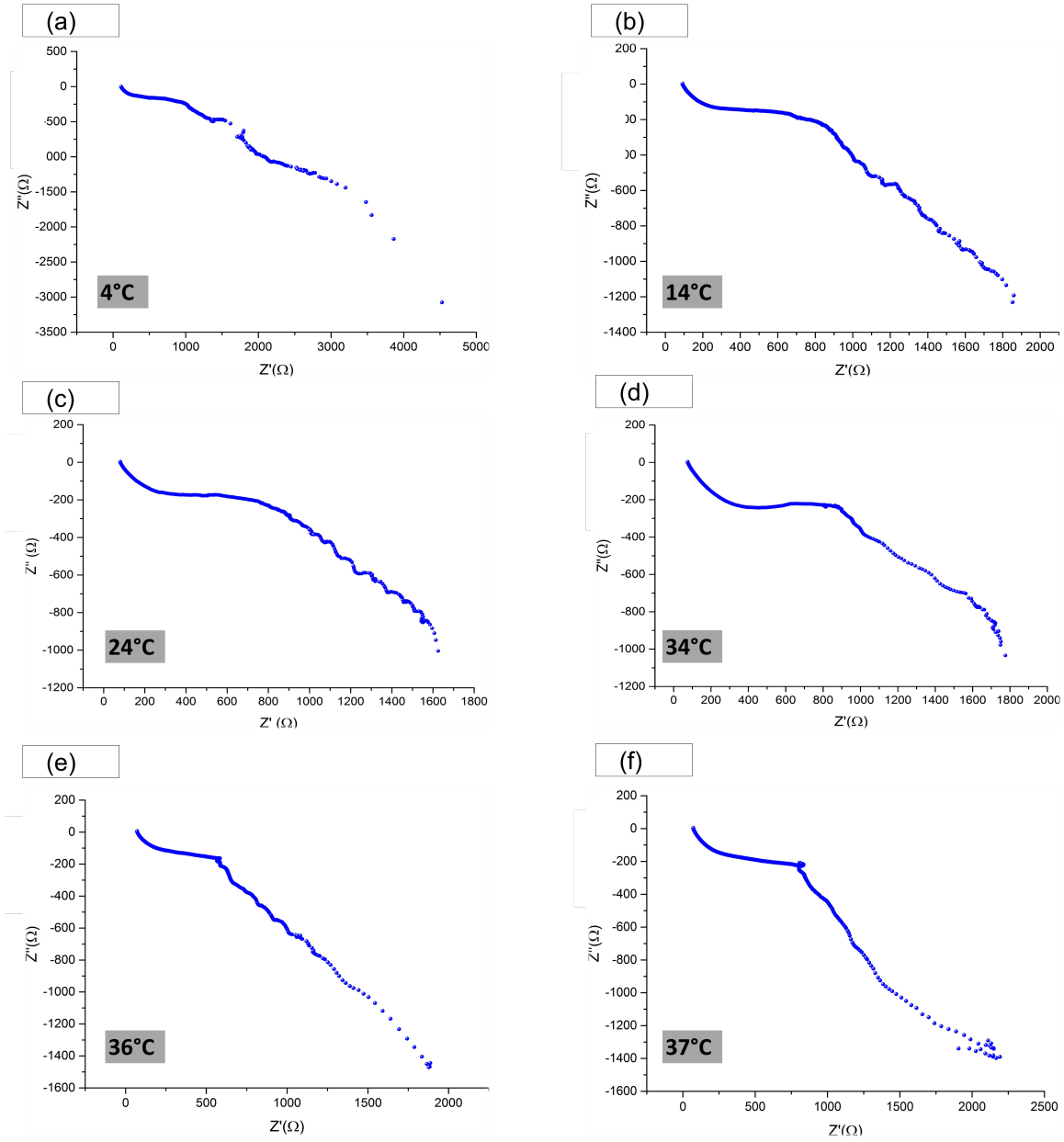

FIGURE 5.4: Impedance of PBS and electrodes, for different temperatures as a function of frequency.

solution is taken out of the fridge, its temperature increase. In all the pictures, the center of the recipient is colder than the walls, revealing a temperature gradient. The values of impedance were measured with the sample in the center of the recipient to avoid this thermal gradient.

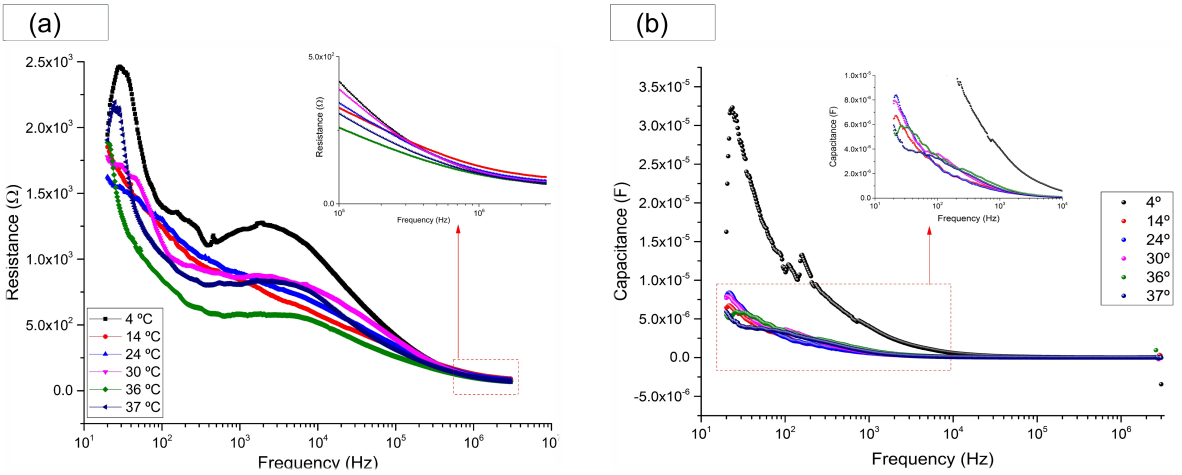

FIGURE 5.5: The values of resistance and capacitance for the PBS and electrodes system.

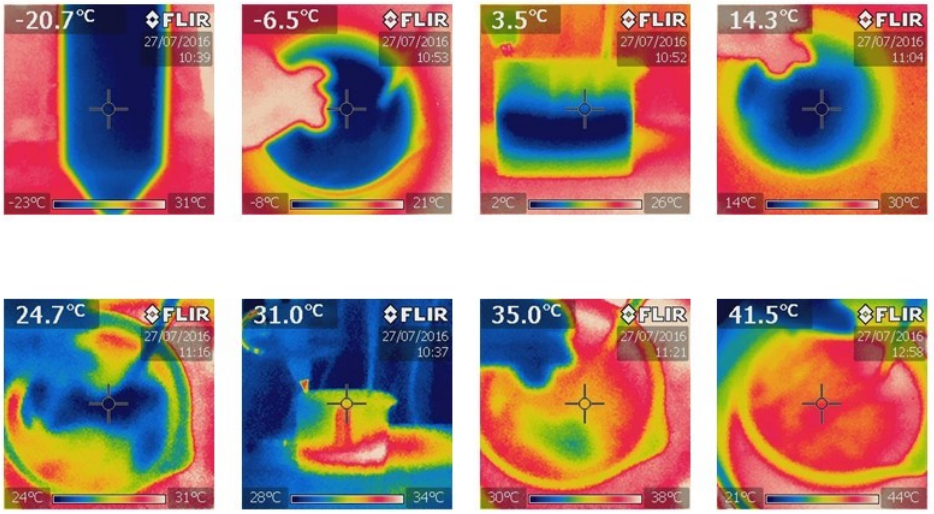

FIGURE 5.6: Thermal evolution of the PBS solution.

5.3 Cell culture

For the cell culture, the microelectrodes were carefully sterilized for 24 h and coated with 0.1 mg.ml^{-1} PDL for 24 h. ND$7/23$ cells (DMEM GlutaMAXTM, 1% P/S; 10% FBS) were plated at a density of 6.0×10^4 cells/cm^2, and left undisturbed at 37 °C, in a humidified atmosphere with 5% CO_2. After three days of culture, cells were fixed and actin filaments were labelled with Alexa Fluor-Phalloidin 488 (Invitrogen). Imaging was performed on an inverted confocal microscope Leica TCS SP5 II. These experiments were performed at i3S by local researchers.

Figure 5.7 shows the neurons culture in the gold-mushroom microelectrodes arrays. The green dots identify the neuron cell. In this figure, we can see that neuron moved in the solution,

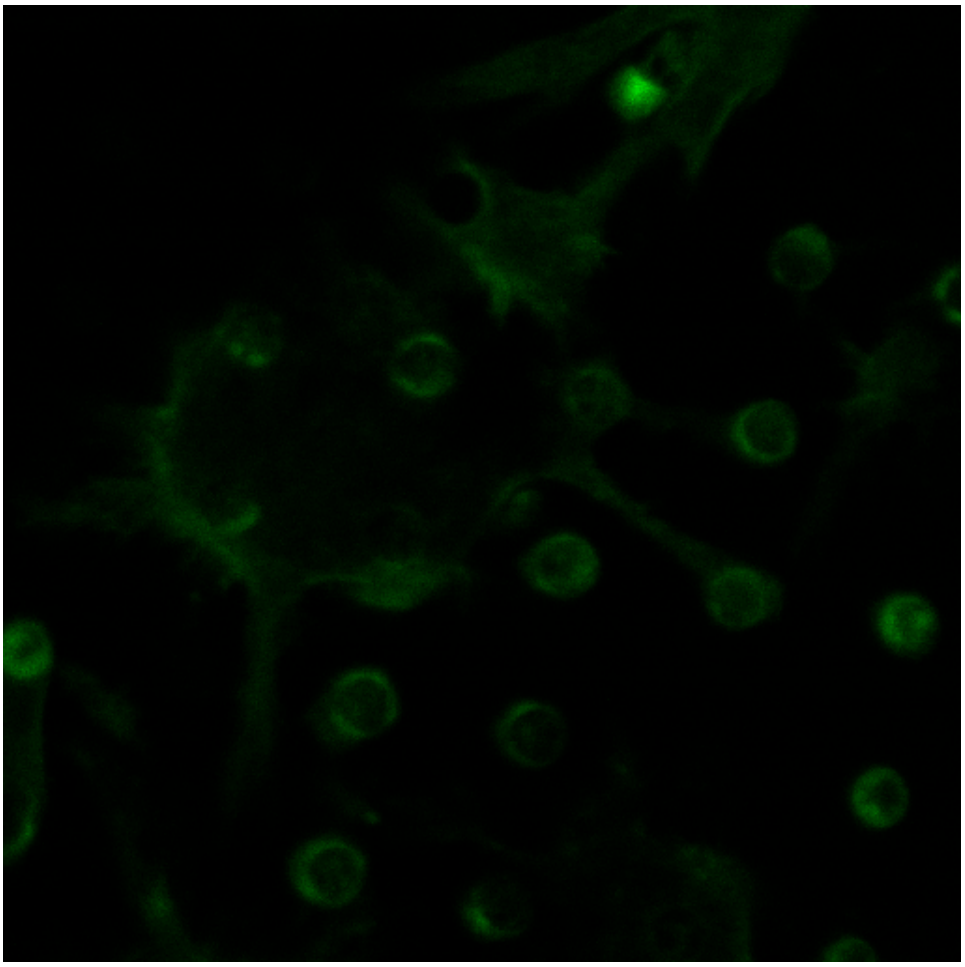

FIGURE 5.7: Microscope image of the neurons placed in the gold-mushroom microelectrodes arrays.

because some caps of the microelectrodes are green in the image, but there is no neuron engulfing the microelectrode. This situation indicates that the gold-mushrooms had a neuron cell above it, but the engulfment did not occur, leaving behind residues of the cellular membrane. In the left part of the figure we verify that there are neurons that did engulf mushrooms with succeed.

Before the sample is characterized by SEM, it must be prepared. This sample was submitted to a critical point drying method. This method is used for dehydrating biological tissue, where the water in biological tissue is replaced by CO_2. Afterwards, the sample was introduced in a sputtering system to deposit a thin layer of Au/Pd, to create a conductive medium.

Figures 5.8 and 5.9 show the engulfment of the gold-mushroom microelectrodes by a neuron cell. Figure 5.8 corresponds to a set of images where it is possible see the microelectrodes

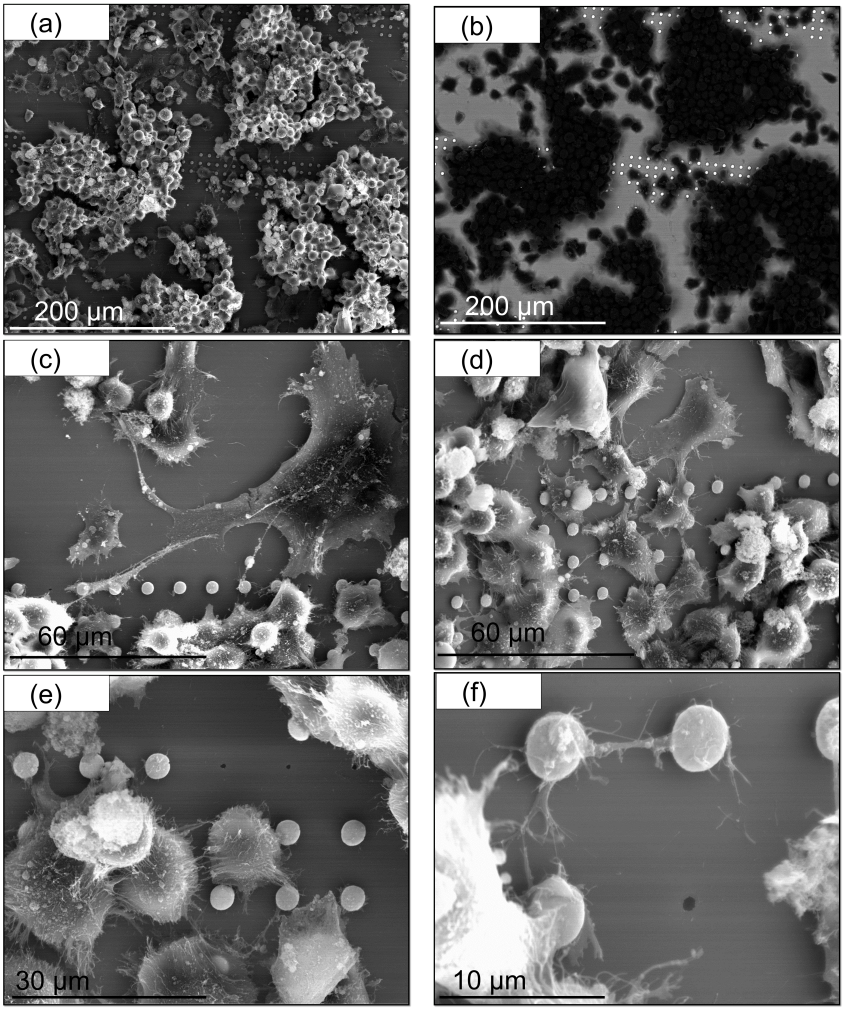

FIGURE 5.8: SEM micrographs of the neuron culture in the microelectrode electroplated for 70 min.

grown during 70 min engulfed by the neurons. Figure 5.8(a), allows us to identify a large number of neuron cells cultured on the microelectrodes. Figure 5.8(b) corresponds to a BE image where the bright points are the gold-mushroom microelectrodes and the dark region corresponds to biological matter, in this case, neurons. Figures 5.8(c)-(f) show with more accuracy the engulfment of the microelectrodes. In the last figure [Fig. 5.8 (f)], it is possible to observe a bridge created by the cellular membrane between the microelectrodes.

For the sample electroplated during 94 min, the SEM characterization is represented in Fig. 5.9. Figure 5.9(a), shows neuron cells cultured on the microelectrodes. Comparing Fig. 5.8(a) with Fig. 5.9(a), the neurons are more disperse in the latter. In Fig. 5.9(b), the bright points correspond to gold-mushroom microelectrode and the dark regions to the neuron cells. Figures

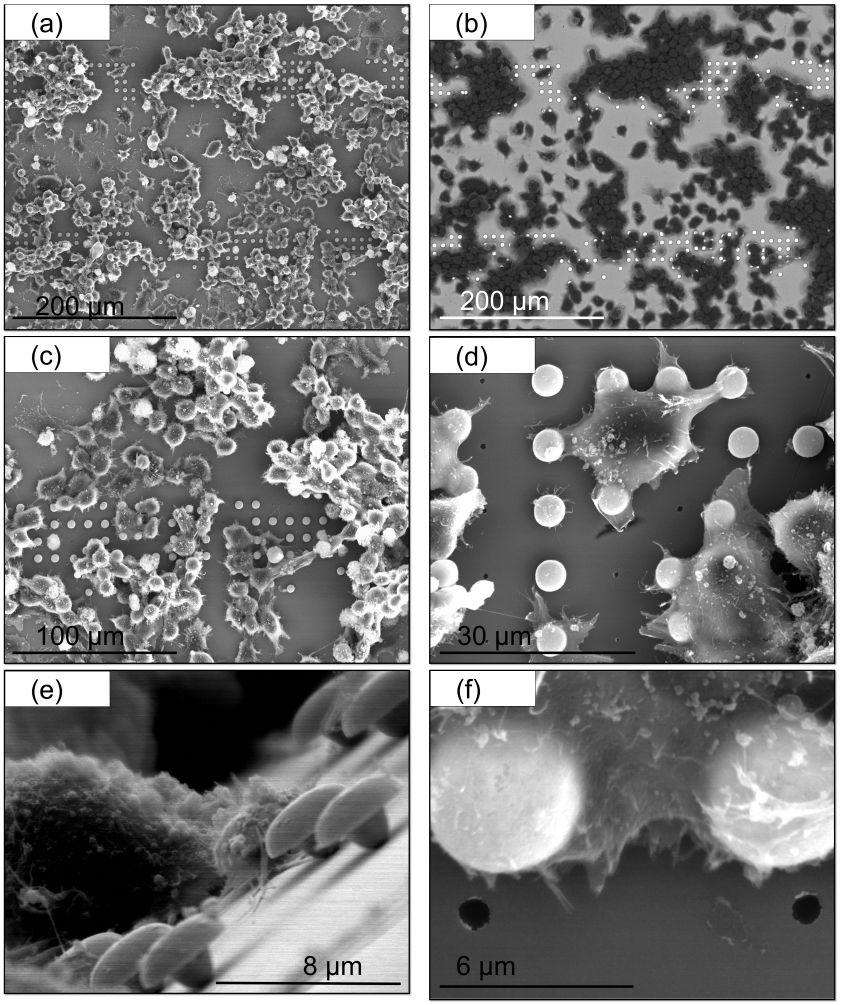

FIGURE 5.9: SEM micrographs of the neuron culture in the microelectrode electroplated for 94 min.

5.9(c)-(f) show the engulfment of the microelectrodes and Fig. 5.9(e) is a cross-section of the interface between microelectrodes and neuron cells.

Figures 5.8(a)-(b) and 5.9(a)-(b) allows us to verify that the array is not complectly full, because some regions lack the presence of the microelectrodes. In fact, the gold-mushroom microelectrodes arrays produced appear in 50 µm columns, that repeat each 150 µm. This situation occurs because the laser used to write the pattern in the photoresist writes in leaks of 200 µm, and inside each leak the laser writes the first 50 µm correctly, but loses energy as exposure proceeds, so that the pattern is not complectly transferred.

An EDS analysis was also performed (Fig. 5.10). The spectrum analysis of Fig. 5.10(a) corresponds to a gold-mushroom microelectrode. In the spectrum two materials were identified, gold (Au) and carbon (C). Then, this analysis allows us to comfirm that, when electrodeposition

occurs, only gold is deposited. The presence of carbon is a biological contamination. Figure 5.10(b) corresponds to an EDS analysis to the surface of an engulfed microelectrode, showing the presence of Gold, Silicon, Aluminum, Oxygen and Carbon. The presence of Gold and Silicon is normal, because Silicon appears from the substrate and Gold from the thin film deposited in the substrate surface. Oxygen and Carbon are biological contaminations, that have origin in the handling of the sample. The last spectrums [Fig. 5.10(c)] was taken to the surface of the substrate, and the peak observed is related to the material of the substrate (silicon). Figure 5.10(d), corresponds to an analysis of a defect detected in the substrate surface which shows the presence of silicon.

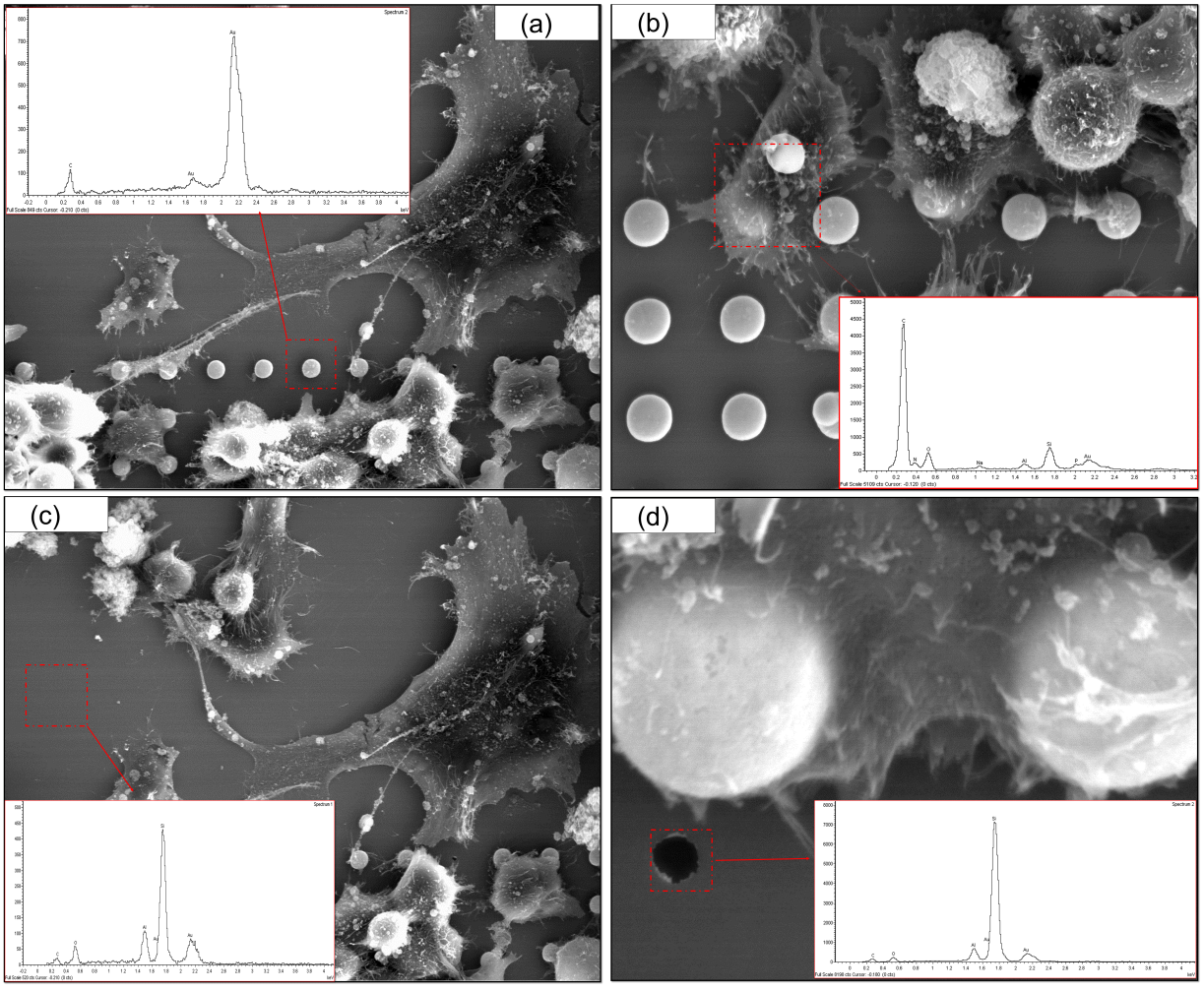

FIGURE 5.10: EDS analysis, for the sample electrodeposited during (a), (c)70 min and (b), (d) for 94 min.

The biophysical parameters (gMμE area and gMμE capacitance) were calculated for this two interfaces. Through the Eqs. (2.4)- (2.7) we calculated the gold-mushroom, stalk, cap and rim

areas, that allows us to estimate the capacitance value of the gold-mushroom microelectrodes. The areas are summarized in Table 5.1.

TABLE 5.1: Estimated areas of the stalk, cap, rim and gold-mushroom microelectrode for 70 and 94 min of electrodeposition.

Deposition Time	**AStalk**	**ACap**	**ARim**	**AgMμE**
70 min	7.91	22.68	8.80	39.39
94 min	3.43	18.17	17.6	39.20

The gold-mushroom microelectrode capacitance given according to Eq. (2.10) has approximately a value of 19.6 pF for the two microelectrodes and the resistance is 2.8 GΩ.

Chapter 6

Electrical Simulations

In this chapter we will present a brief description of simulations performed on coupling coefficient of gold-mushrooms microelectrode arrays.

The coupling coefficient is the ratio between the electrical signal measured by the electrodes and the signal that passes inside a neuron. These signals are not equal because there are several intrinsic parameters that influence the measured value. In order to evaluate the ability and the accuracy of the measurements, we simulated the values of the coupling coefficient for different values of resistance membrane junctional (R_j), of resistance membrane non-junctional(R_{nj}) and resistance of the electrode (R_e). The engulfment can be represented by an equivalent electrical circuit, as shown in Fig. 6.1.

The NI Multisim 14.0 software allows us to simulate the behavior of an electrical circuit. Figure 6.2 represents the electrical circuit used in the simulations. The electrical circuit is composed by a pulsed current source, resistances and capacitors. The circuit has three main blocks that are divided in Non-junctional region, Junctional region and Electrode recording and each of them is composed by a resistance and a capacitor. The Non-junctional region is the first block and represents the part of the membrane that is not in contact with the electrode; the Junctional region is the second block and the part of the cellular membrane that is in contact with the cap of the gold-mushroom microelectrode; finally, the third block corresponds to a microelectrode structure. In the circuit there is also one resistance named Seal Resistance that corresponds to the resistance between the electrode and the culture medium.

The input signal is generated by a pulsed current source, that applies to the circuit a current that oscillates between 0 and a given value at a certain frequency. In our case, we applied pulsed current of 1 nA with different values of amplitude at 1000 Hz. Figure 6.3, show the values

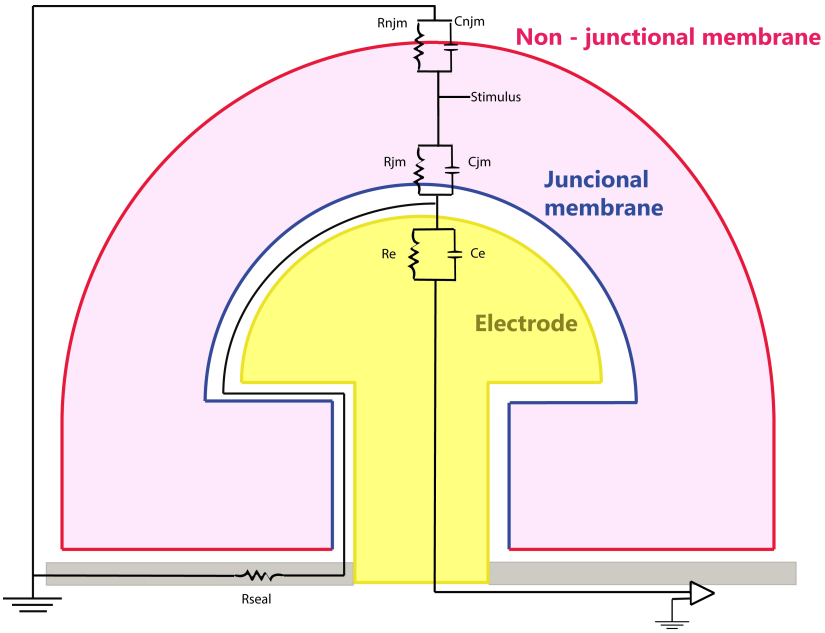

FIGURE 6.1: Schematic of the engulfment of a gold-mushroom microelectrode by a neuron cell. The electrical circuit represented is an equivalent for the situation.

found for 60 s of simulation. We see that, with decreasing junctional resistance, the coupling coefficient increases. In the real case, decreasing the value of the junctional resistance means acquiring more signal, because the opposition to the charge flow decreases. However, this fact needs to be complemented with the value of the seal resistance. Increasing the seal resistance implies an approximating the surface of the electrode to the cell membrane. The seal resistance appears during the engulfment, as a result of the creation a cleft between the cell and electrode. When the value of the seal resistance increases, the cleft is reduced, allowing a better engulfment and a better signal recording.

To analyse the maximum depolarization value, we applied to the circuit different pulsed currents and measured the maximum value of depolarization, after 60 s. The results are plotted in Fig. 6.4 and shows a linear dependence between these two quantities.

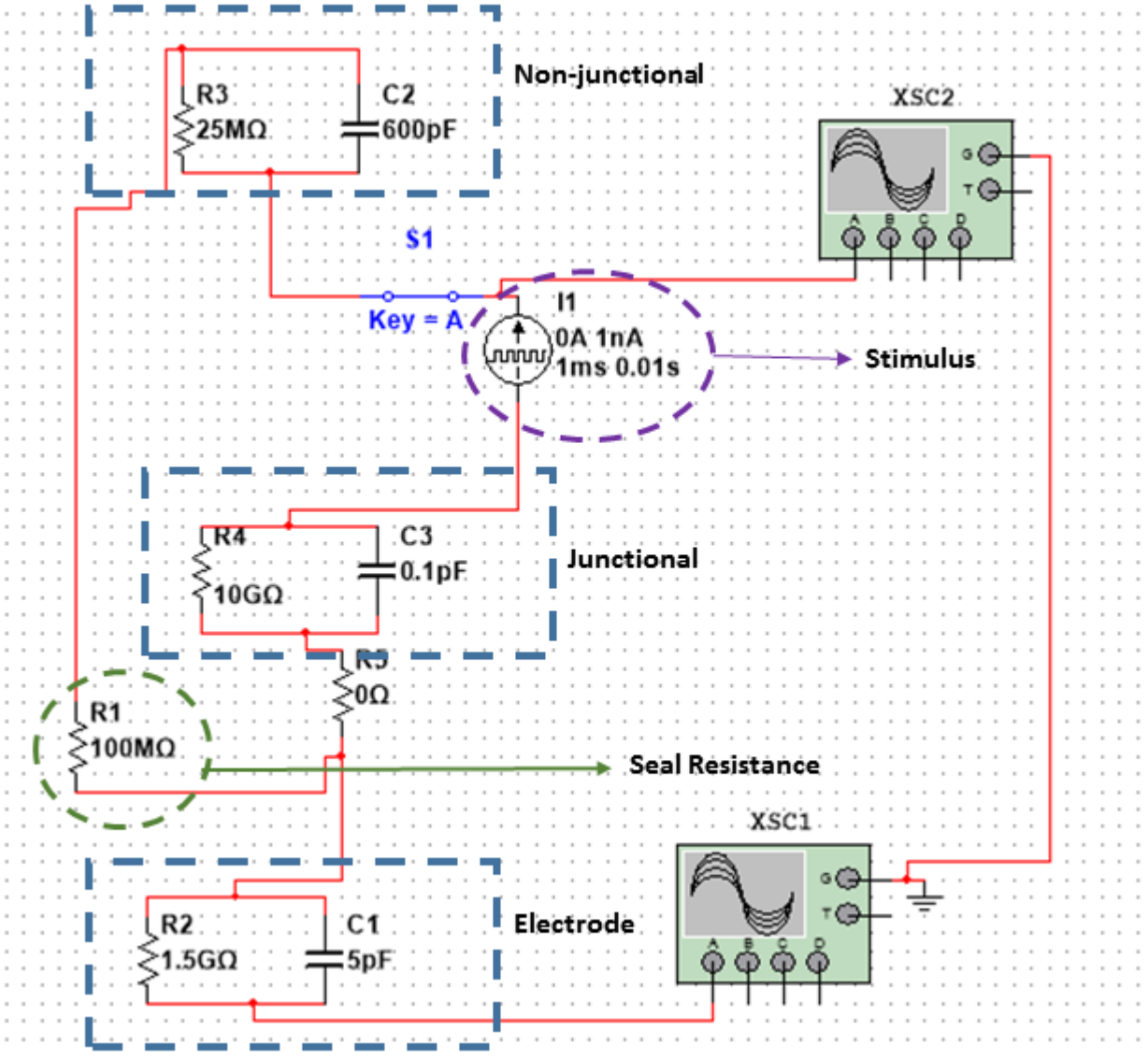

FIGURE 6.2: Electrical circuit implemented in NI Multisim 14.0.

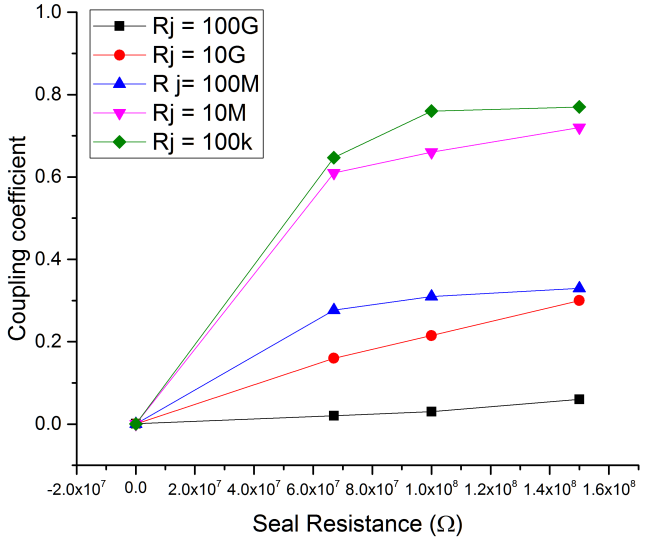

FIGURE 6.3: Coupling coefficient for pulses of current of 1 nA at 100 Hz.

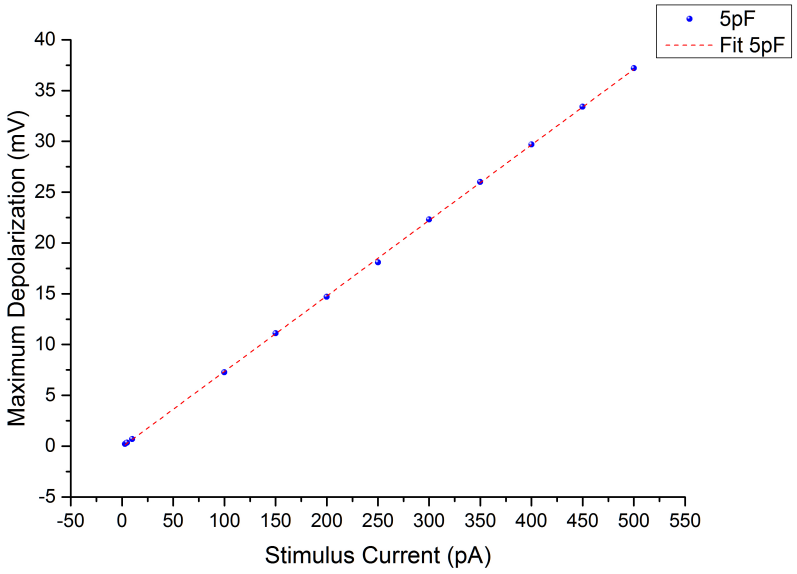

FIGURE 6.4: Maximum depolarization acquired by the gold-mushroom microelectrode arrays through changing the stimulus intensity.

Chapter 7

Conclusion and Future work

Conclusion

Neuroelectronics allows to capture electrical signals transmitted between cells. These signals are important, because through their interpretation, we can developed new devices, be able to treat deceases or develop new ways to improve the life quality of the human being. In this project, our main objective was to develop a neuronal hybrid interface. In that respect, we demonstrated an experimental procedure and optimization steps to created this interface.

The first experimental study was the optimization of 1.5 and 2 µm dot sizes in the Direct Write system. Lithographed patterns with 1.5 µm were obtained for 20 mW with a pulse duration of 50% while 2 µm dots were achieved for 10 mW at 18%, for a S1818 photoresist. Finally, we observed that the minimum energy necessary to totally expose 1.2 µm thick photoresist is 10 mW 12%. Afterwards, we studied the best potential to electroplate the structures. Through temperature, deposition and efficiency testes, we determine that electrodepositions at -1.0 V have 71% efficiency and provide the desired structures with a deposition rate of about 46 nm/min.

Finally, the interface between neurons and the gold-mushroom microelectrodes was created. For the first interface, the structures were deposited during 70 min at -1.0 V, revealing a cap diameter of 3.8 µm and a total height of 2.7 µm. The gMμE area is 39.39 µm^2, that implies a capacity of 19.6 pF. For the second interface, the structures were electroplated during 90 min at -1.0 V having a cap diameter of 3.8 µm and a total height of 2.7 µm. The gMμE area is 39.39 µm^2 and the corresponding capacity is 19.6 pF.

In this work, the two interfaces were successfully created and, through SEM images, it was possible to observe the engulfment of the gold-mushrooms by the neuronal membrane. The development and optimization of this microelectrodes can open the possibility of creating new devices.

As future work, we propose the implementation of different shapes and sizes of the gold-mushroom microelectrodes arrays, in order to evaluated the values of the coupling coefficient. It is also necessary to record the neuronal signal, stimulate the nervous cells through the microelectrodes and understand the movement and growth of the neurons on top of them.

Bibliography

[1] Sebastian Bitzer and Patrick Van Der Smagt. Learning emg control of a robotic hand: towards active prostheses. In *Proceedings 2006 IEEE International Conference on Robotics and Automation, 2006. ICRA 2006.*, pages 2819–2823. IEEE, 2006.

[2] Study.com. The Peripheral Nervous System Lesson for Kids. URL http://study.com/academy/lesson/the-peripheral-nervous-system-lesson-for-kids.html.

[3] Tainers. What is alice in wonderland syndrome and how can you treat the symptoms. URL http://www.yurtopic.com/health/diseases-conditions/alice-syndrome.html.

[4] David Sterratt, Bruce Graham, Andrew Gillies, and David Willshaw. *Principles of computational modelling in neuroscience*. Cambridge University Press, 2011.

[5] A SILVA, F Gramaxo, M SANTOS, A MESQUITA, L Baldaia, and J FÉLIX. *Terra, Universo de Vida–2ª Parte*. Geologia. Porto Editora: Porto., 2004.

[6] Micha E Spira and Aviad Hai. Multi-electrode array technologies for neuroscience and cardiology. *Nature nanotechnology*, 8 (2):83–94, 2013.

[7] Long Yang, Yuanchang Li, and Ying Fang. Nanodevices for cellular interfaces and electrophysiological recording. *Advanced Materials*, 25(28):3881–3887, 2013.

[8] Yinxi Huang and Peng Chen. Nanoelectronic biosensing of dynamic cellular activities based on nanostructured materials. *Advanced Materials*, 22(25):2818–2823, 2010.

[9] Michele Sessolo, Dion Khodagholy, Jonathan Rivnay, Fabien Maddalena, Melanie Gleyzes, Esther Steidl, Bruno Buisson, and George G Malliaras. Easy-to-fabricate conducting polymer microelectrode arrays. *Advanced Materials*, 25(15):2135–2139, 2013.

[10] Jacob T Robinson, Marsela Jorgolli, and Hongkun Park. Nanowire electrodes for high-density stimulation and measurement of neural circuits. *Frontiers in neural circuits*, 7:26–30, 2013.

[11] Alessandra Fabbro, Susanna Bosi, Laura Ballerini, and Maurizio Prato. Carbon nanotubes: artificial nanomaterials to engineer single neurons and neuronal networks. *ACS chemical neuroscience*, 3(8):611–618, 2012.

[12] Sara Bonde, Nina Buch-Månson, Katrine R Rostgaard, Tor Kristian Andersen, Trine Berthing, and Karen L Martinez. Exploring arrays of vertical one-dimensional nanostructures for cellular investigations. *Nanotechnology*, 25(36):362001–362020, 2014.

[13] Aviad Hai, Ada Dormann, Joseph Shappir, Shlomo Yitzchaik, Carmen Bartic, Gustaaf Borghs, JPM Langedijk, and Micha E Spira. Spine-shaped gold protrusions improve the adherence and electrical coupling of neurons with the surface of microelectronic devices. *Journal of The Royal Society Interface*, 6.

[14] Silviya M Ojovan, Noha Rabieh, Nava Shmoel, Hadas Erez, Eilon Maydan, Ariel Cohen, and Micha E Spira. A feasibility study of multi-site, intracellular recordings from mammalian neurons by extracellular gold mushroom-shaped microelectrodes. *Scientific reports*, 5:14–100, 2015.

[15] Francesca Santoro, Jan Schnitker, Gregory Panaitov, and Andreas Offenh usser. On chip guidance and recording of cardiomyocytes with 3d mushroom-shaped electrodes. *Nano letters*, 13(11):5379–5384, 2013.

[16] Aviad Hai, Joseph Shappir, and Micha E Spira. In-cell recordings by extracellular microelectrodes. *Nature methods*, 7(3): 200–202, 2010.

[17] Leonardo Sileo, Ferruccio Pisanello, Luca Quarta, Alessandro Maccione, Alessandro Simi, Luca Berdondini, Massimo De Vittorio, and Luigi Martiradonna. Electrical coupling of mammalian neurons to microelectrodes with 3d nanoprotrusions. *Microelectronic engineering*, 111:384–390, 2013.

[18] Aviad Hai, Joseph Shappir, and Micha E Spira. Long-term, multisite, parallel, in-cell recording and stimulation by an array of extracellular microelectrodes. *Journal of neurophysiology*, 104(1):559–568, 2010.

[19] DK Maurya, Ali Sardarinejad, and Kamal Alameh. Recent developments in rf magnetron sputtered thin films for ph sensing applications—an overview. *Coatings*, 4(4):756–771, 2014.

[20] L Santos, JP Neto, A Crespo, P Baião, P Barquinha, L Pereira, R Martins, and E Fortunato. Electrodeposition of wo3 nanoparticles for sensing applications. *InTech*, pages 27–47, 2015.

[21] Pedro Miguel de Campos Resende. Micro/nanogenerators for thermal energy harvesting. Master's thesis, Universidade do Porto, 2015.

[22] Purdue University. Scanning electron microscope. URL https://www.purdue.edu/ehps/rem/rs/sem.htm.

[23] Itamar Willner and Bilha Willner. Biomaterials integrated with electronic elements: en route to bioelectronics. *Trends in biotechnology*, 19(6):222–230, 2001.

[24] Itamar Willner and Eugenii Katz. *Bioelectronics: from theory to applications*. John Wiley & Sons, 2006.

[25] Zoltan Fekete. Recent advances in silicon-based neural microelectrodes and microsystems: a review. *Sensors and Actuators B: Chemical*, 215:300–315, 2015.

[26] Bert Sakmann. *Single-channel recording*. Springer Science & Business Media, 2013.

[27] Kenpitts. Neuron. URL http://kenpitts.net/bio/human_anat/neuron_brain.htm.

[28] Paul Rea. *Essential Clinical Anatomy of the Nervous System*. Academic Press, 2015.

[29] Michael M Cox et al. *Lehninger principles of biochemistry*. Freeman, 2013.

[30] Bertil Hille et al. *Ion channels of excitable membranes*, volume 507. Sinauer Sunderland, MA, 2001.

[31] Gregory Panaitov, Simon Thiery, Boris Hofmann, and Andreas Offenhäusser. Fabrication of gold micro-spine structures for improvement of cell/device adhesion. *Microelectronic engineering*, 88(8):1840–1844, 2011.

[32] Chong Xie, Ziliang Lin, Lindsey Hanson, Yi Cui, and Bianxiao Cui. Intracellular recording of action potentials by nanopillar electroporation. *Nature nanotechnology*, 7(3):185–190, 2012.

[33] D Brüggemann, B Wolfrum, V Maybeck, Y Mourzina, M Jansen, and A Offenhäusser. Nanostructured gold microelectrodes for extracellular recording from electrogenic cells. *IOP*, 22(26):265104,7pp, 2011.

[34] Masoud Fereidoni, Yaghoub Fathollahi, Mahyar Janahmadi, and Iran Godarzi. A rapid and non leaky way for preparation of the sharp intracellular recording microelectrodes. *Journal of biochemical and biophysical methods*, 70(6):1124–1129, 2008.

[35] Jan Konopacki, Brian H Bland, and Richard Dyck. Intracellular recording and labeling of neurons in midline structures of the rat brain in vivo using sharp electrodes. *Journal of neuroscience methods*, 127(1):85–93, 2003.

[36] Rigo Pantoja, John M Nagarah, Dorine M Starace, Nicholas A Melosh, Rikard Blunck, Francisco Bezanilla, and James R Heath. Silicon chip-based patch-clamp electrodes integrated with pdms microfluidics. *Biosensors and Bioelectronics*, 20(3): 509–517, 2004.

[37] Maria Spassova, James C Saunders, and Thomas D Parsons. Chick cochlear hair cell exocytosis mediated by dihydropyridine-sensitive calcium channels. *The Journal of Physiology*, 535(3):689–696, 2001.

[38] Niels Fertig, Robert H Blick, and Jan C Behrends. Whole cell patch clamp recording performed on a planar glass chip. *Biophysical journal*, 82(6):3056–3062, 2002.

[39] Axel Blau. Cell adhesion promotion strategies for signal transduction enhancement in microelectrode array in vitro electrophysiology: an introductory overview and critical discussion. *Current Opinion in Colloid & Interface Science*, 18(5):481–492, 2013.

[40] Nava Shmoel, Noha Rabieh, Silviya M Ojovan, Hadas Erez, Eilon Maydan, and Micha E Spira. Multisite electrophysiological recordings by self-assembled loose-patch-like junctions between cultured hippocampal neurons and mushroom-shaped microelectrodes. *Scientific reports*, 6(27110):1–11, 2016.

[41] Micha E Spira, Dotan Kamber, Ada Dormann, Ariel Cohen, Carmen Bartic, Gustaf Borghs, JPM Langedijk, Shlomo Yitzchaik, Keren Shabthai, and Josef Shappir. Improved neuronal adhesion to the surface of electronic device by engulfment of protruding micro-nails fabricated on the chip surface. In *TRANSDUCERS 2007-2007 International Solid-State Sensors, Actuators and Microsystems Conference*, pages 1247–1250. IEEE, 2007.

[42] Ulrich Egert and Thomas Meyer. Heart on a chip—extracellular multielectrode recordings from cardiac myocytes in vitro. In *Practical Methods in Cardiovascular Research*, pages 432–453. Springer, 2005.

[43] Yoonkey Nam and Bruce C Wheeler. In vitro microelectrode array technology and neural recordings. *Critical Reviews^{TM} in Biomedical Engineering*, 39(1):45–61, 2011.

[44] Francesca Santoro, Gregory Panaitov, and Andreas Offenh usser. Defined patterns of neuronal networks on 3d thiol-functionalized microstructures2. *Nano letters*, 14(12):6906–6909, 2014.

[45] Anna Fendyur, Noa Mazurski, Joseph Shappir, and Micha E Spira. Formation of essential ultrastructural interface between cultured hippocampal cells and gold mushroom-shaped mea-toward “in-cell” recordings from vertebrate neurons. *Frontiers in neuroengineering*, 4(14).

[46] Donald M Mattox. *Handbook of physical vapor deposition (PVD) processing*. William Andrew, 2010.

[47] PJ Kelly and RD Arnell. Magnetron sputtering: a review of recent developments and applications. *Vacuum*, 56(3):159–172, 2000.

[48] MILAN Paunovic, Mordechay Schlesinger, and Dexter D Snyder. *Fundamental considerations*. 2010.

[49] Allen J Bard, Larry R Faulkner, Johna Leddy, and Cynthia G Zoski. *Electrochemical methods: fundamentals and applications*, volume 2. Wiley New York, 1980.

[50] Richard P Baldwin, K Ravichandran, and Ronda K Johnson. A cyclic voltammetry experiment for the instrumental analysis laboratory. *J. Chem. Educ*, 61(9):820–823, 1984.

[51] Plating Chemistry. gold. http://www.technic.com/eu/applications/industrial/industrial-chemistry/plating-chemistry. 2016-06-30.

[52] Paul A Kohl. Electrodeposition of gold. *Modern Electroplating*, 5(4).

[53] Peter Wilkinson. Understanding gold plating. *Gold Bulletin*, 19(3):75–81, 1986.

[54] Carleton. xrd. http://serc.carleton.edu/research_education/geochemsheets/techniques/XRD.html. 2016-06-27.

[55] Michael B Heaney. Electrical conductivity and resistivity. *The measurement, instrumentation and sensors handbook*, pages 1332–1345, 2000.

[56] Yadunath Singh. Electrical resistivity measurements: a review. In *International journal of modern physics: Conference series*, volume 22, pages 745–756. World Scientific, 2013.

[57] Martin Feldman. Nanolithography: The art of fabricating nanoelectronic and nanophotonic devices and systems. 1(42).

[58] Wood Growth Rate. Reference module in materials science and materials engineering. pages 37–76, 2012.

[59] Data Sheet. Microposit s1800 series photoresists. *Shipley Company, Marlborough, MA*, pages 1–6, 1993.

[60] Microchemicals.Spin Coating of PhotoResists. http://www.microchemicals.com/downloads/application_notes.html. 2016-06-16.

[61] Microchemicals. Softbake of Photoresist Films, . URL http://www.microchemicals.com/downloads/application_notes.html.

[62] Microchemicals.Exposure of Photoresists. http://www.microchemicals.com/downloads/application_notes.html. 2016-06-16.

[63] Microchemicals. Baking Steps in Photoresists Processing, . URL http://www.microchemicals.com/downloads/application_notes.html.

[64] Microchemicals.Development of Photoresist. http://www.microchemicals.com/downloads/application_notes.html. 2016-06-16.

[65] Peter T Kissinger and William R Heineman. Cyclic voltammetry. *J. Chem. Educ*, 60(9):702, 1983.

[66] Gary A Mabbott. An introduction to cyclic voltammetry. *J. Chem. Educ*, 60(9):697–702, 1983.

[67] Gerko Oskam and Peter C Searson. Electrochemical nucleation and growth of gold on silicon. *Surface science*, 446(1): 103–111, 2000.

[68] Victor Reyes-Cruz, Carlos Ponce-de León, Ignacio González, and MT Oropeza. Electrochemical deposition of silver and gold from cyanide leaching solutions. *Hydrometallurgy*, 65(2):187–203, 2002.

[69] Yutaka Okinaka and Masao Hoshino. Some recent topics in gold plating for electronics applications. *Gold Bulletin*, 31(1): 3–13, 1998.

[70] V Reyes-Cruz, I Gonzalez, and MT Oropeza. Electro-recovery of gold and silver from a cyanide leaching solution using a three-dimensional reactor. *Electrochimica Acta*, 49(25):4417–4423, 2004.

Appendix A

Appendixes

Process Name: Gold – mushroom microelectrodes arrays
Responsible:
Samples: 8 glass 1 inch (4 dies per sample)

RUNSHEET

Process Start: 21/03/2016 Process Finish: 25/03/2016

Step1	Stack deposition	Date	
		Responsible	

Thin film Deposition

Alcatel – magnetron sputtering

Step2	**1st Lithography @ INESC-MN**	Date	
		Responsible	

ID	**Stack**	**Die arrangement**	**#Samples**
Batch#1	Si/ Cr 3 nm/Au 30-40 nm	1inch substrate/ 30 dies Holes Diameter =2 um nominal (@mask) Pitch =10 um	30 samples (4 dies per substrate)

1.Sample Preparation

1) Vapor Prime

Step description	Conditions
Wafer dehydration	Vacuum, 10 Torr, 2 min. N2 inlet, 760 Torr, 3min. Heating to 130ºC
Priming	Vacuum, 1 Torr, 3 min. HDMS, 6 Torr, 5 min.
Purge prime exhaust	Vacuum, 4 Torr, 1 min. N2 inlet, 500 Torr, 2min. Vacuum, 4 Torr, 2 min.
Vent	N2 inlet, 3min.

Coating Parameters	
#1	Dispense photoresist on the sample and spinning at 800 rpm for 5 sec.
#2	Spin at 2500 rpm for 30 sec.
#3	Soft bake at 85º for 60 seconds; Used to remove solvents and stress, while promoting adhesion.

2) Optical Lithography

Origin of the die:

X,Y = 6000, 6000

Map: FOURSQ

Mask: Dots 2um sepio (\ h3)

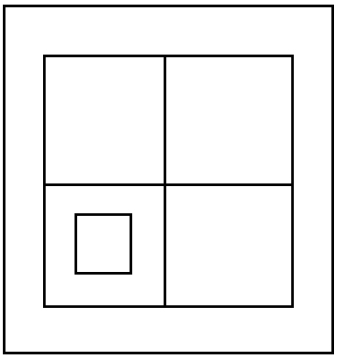

Energy=	60%
Power=	100mw
Focus=	-20
Aligment mask:	X=2000; Y=2000

Details of Map:

Each die =

List f all samples:

Sample#	Exposure Date	Details	Sample#	Exposure Date	Details
#1	21/03/2016	2 µM sep 10/60	**#5**	21/03/2016	Ok
#2	21/03/2016	2 µM sep 10/60	**#6**	21/03/2016	Ok
#3	21/03/2016	2 µM sep 10/60	**#7**	21/03/2016	Ok
#4	21/03/2016	2 µM sep 10/60	**#8**	21/03/2016	ok

Nota: No alinhamento inicial para a origem ter em atenção que há uma parte do substrato quando é vidro.

3) Development

Development parameters	
Bake	110º C for 60s
Cool	30s

SVG system
TMA238WA chemical developer

ID	Exposure Energy	Development time
Batch#1	**60**	**120 sec** (60s +60s processo feito duas vezes)

4) Optical Inspection

#1 – Os poros estão abertos é possível identificar;

#4- Está identificado no array de poros com a lente de 50X; com a lente de 100X também parece aberto e parece ter profundidade. Estão todos os arrays identificados todos têm profundidade.

5) Profile inspection



NanoPattern Definition E-Beam

Machine: RAITH 150

Coating	Substrate preparation	Specifications	Recipe	(Pre) Bake
	x	x	30'' @ 3 krpm Manual dispensing	4 min @160ºC
	x	PMMA 950k	Track 2: Coater / Stations: 1 Hot Plate	
	Comments: Coating performed twice to achieve a nominal thickness of 1 um			

				@ user diana /Nano Si etch:
Exposure	Mask: Structure: Matrix:	NanoMushrooms main 2x2	WF:	500 um
	Layers:	0	WA:	boundaries
	Coordinates:	Origin @ 7,7 mm		

	Column Parameters					**Exposure Parameters**			
	VB (kV)	A (um)	WD (mm)	A .Alignment Stigmation	IB (pA)	Step Size (nm)	Dwell Time (ns)	Base Dose (uC/cm^2)	Beam speed (mm/s)
Pillars	10	10	~ 7	-	21	6.4	-	200	-
Comments:	Sizes very close to nominal. Dispersion <5%.								

Develop	(Pos) Bake	Specifications	Recipe
	x	MIBK + Stopper IPA	Developing time: 80'' Manual
Comments:	x		Immerse in IPA

Observations: